Thesis

Exotic superconductivity associated with parity symmetry breaking

by

Shota Kanasugi

Department of Physics, Kyoto University
February, 2022

KYOTO UNIVERSITY

Abstract

Investigation of unconventional superconductivity has been one of the central topics in modern condensed matter physics. In unconventional superconductors, interesting phenomena have been clarified owing to various kinds of symmetry breaking from the internal degrees of freedom of Cooper pairs. In particular, the interplay between superconductivity and *parity symmetry breaking* is attracting much attention since the discovery of noncentrosymmetric superconductors. Parity symmetry is one of the fundamental properties in quantum materials, and hence the lack of parity symmetry significantly affects the superconducting properties and leads to exotic superconducting phenomena. Although most of such phenomena have been elucidated for noncentrosymmetric superconductors, we can consider other types of superconductors associated with parity symmetry breaking; (i) superconductors coexistent with other parity-breaking orders, (ii) locally noncentrosymmetric superconductors, and (iii) superconductors hosting multiple even- and odd-parity pairing instabilities. However, theoretical understanding for these kinds of superconductors is still insufficient compared with that for noncentrosymmetric superconductors. In this thesis, we investigate such exotic superconductors and uncover the novel interplay between superconductivity and parity symmetry breaking.

First, regarding the type (i), we study a coexistent phenomenon of superconductivity and ferroelectric-like polar parity-breaking order, which we call the *ferroelectric superconductivity*. In particular, we focus on $SrTiO_3$ as a possible candidate of the ferroelectric superconductor and demonstrate the impacts of the multiorbital/multiband effect on the ferroelectric superconductivity. By analyzing a multiorbital model for $SrTiO_3$, we demonstrate that the ferroelectric superconductivity is stabilized in a very low carrier density regime or high magnetic field regime. The essential ingredient for stabilizing the ferroelectric superconductivity is Rashba-type spin-orbit coupling dynamically induced by the ferroelectric ordering, which is significantly affected by multiorbital/multiband effects. Furthermore, we predict that the ferroelectric superconductivity in $SrTiO_3$ leads to a topological Weyl superconducting state and generation of odd-frequency pair correlations.

Second, regarding the type (ii), we clarify the novel interplay of ferromagnetic-fluctuation-driven odd-parity superconductivity and locally noncentrosymmetric crystal structure. To this end, we consider a bilayer triangular lattice Hubbard model, which is relevant to, e.g., bilayer transition metal dichalcogenides. In this model, odd-parity spin-triplet superconductivity is

realized in a wide range of parameter regimes owing to the ferromagnetic fluctuation. Specifically, we demonstrate that competing multiple odd-parity pairing instabilities are induced by the layer-dependent staggered antisymmetric spin-orbit coupling that originates from the locally noncentrosymmetric crystal structure. Some of the odd-parity pairing states are identified as topological superconductivity. The obtained results shed light on the possibility of odd-parity superconductivity in various ferromagnetic van der Waals materials.

Lastly, regarding the type (iii), we explore *time-reversal-symmetry-breaking mixed-parity superconductivity* in multiband systems. Recently, superconductivity with spontaneous time-reversal or parity symmetry breaking is attracting much attention owing to its exotic properties, such as nontrivial topology and nonreciprocal transport. Particularly fascinating phenomena are expected when the time-reversal and parity symmetry are simultaneously broken by the spontaneous ordering of time-reversal symmetry-breaking mixed-parity superconductivity, which can be realized when the even- and odd-parity pairing instabilities are competing in one system. This work shows that such time-reversal symmetry-breaking mixed-parity superconducting states generally exhibit an unusual asymmetric Bogoliubov spectrum due to nonunitary interband pairing. For generic two-band models, we derive the necessary conditions for the asymmetric Bogoliubov spectrum. We also demonstrate that the asymmetric Bogoliubov quasiparticles lead to the effective anapole moment of the superconducting state, which stabilizes a nonuniform Fulde-Ferrell-Larkin-Ovchinnikov state at zero magnetic fields. The concept of anapole order employed in nuclear physics, magnetic materials science, strongly correlated electron systems, and optoelectronics is extended to superconductors by this work. Our conclusions are relevant to any multiband superconductors with competing even- and odd-parity pairing interactions. Especially, we apply our theory to UTe_2, in which spontaneous ordering of mixed-parity superconductivity is recently proposed.

Contents

List of publications

Papers related to the thesis

1. Shota Kanasugi and Youichi Yanase,
   Multiorbital ferroelectric superconductivity in doped SrTiO₃,
   Physical Review B **100**, 094504 (2019).
   ©2019 American Physical Society

2. Shota Kanasugi and Youichi Yanase,
   Multiple odd-parity superconducting phases in bilayer transition metal dichalcogenides,
   Physical Review B **102**, 094507 (2020).
   ©2020 American Physical Society

3. Shota Kanasugi, Dushko Kuzmanovski, Alexander V Balatsky, and Youichi Yanase,
   Ferroelectricity-induced multiorbital odd-frequency superconductivity in SrTiO₃,
   Physical Review B **102**, 184506 (2020).
   ©2020 American Physical Society

4. Shota Kanasugi and Youichi Yanase,
   Anapole superconductivity from $\mathcal{PT}$-symmetric mixed-parity interband pairing,
   arXiv:2107.07096 (2021). [accepted in Communications Physics]

Published papers not included in the thesis

1. Shota Kanasugi and Youichi Yanase,
   Spin-orbit-coupled ferroelectric superconductivity,
   Physical Review B **98**, 024521 (2018).
   ©2018 American Physical Society

v

Abbreviations

Abbreviation	Definition
BCS	Bardeen-Cooper-Schrieffer
BdG	Bogoliubov-de Gennes
DOF	Degrees of freedom
DOS	Density of states
FESC	Ferroelectric superconductivity
FFLO	Fulde-Ferrell-Larkin-Ovchinnikov
FM	Ferromagnetic
GL	Ginzburg-Landau
IR	Irreducible representation
NCS	Noncentrosymmetric
RPA	Random phase approximation
SOC	Spin-orbit coupling
STO	$SrTiO_3$
TMD	Transition metal dichalcogenide
vHS	Van Hove singularity
$\mathcal{P}$-symmetry	Parity/space-inversion symmetry
$\mathcal{T}$-symmetry	Time-reversal symmetry
$\mathcal{P}, \mathcal{T}$-odd	Parity- and time-reversal-odd

Chapter 1

Introduction: superconductivity and parity symmetry breaking

Conventional superconductivity, which is described by the Bardeen-Cooper-Schrieffer (BCS) theory [1], is caused by the quantum condensation of spin-singlet s-wave Cooper pairs. Since the Cooper pairs in conventional superconducting states have no internal degrees of freedom, only the U(1) gauge symmetry is spontaneously broken by the superconducting phase transition. On the other hand, unconventional superconductivity has been intensively studied in recent condensed matter physics. The ground state of unconventional superconductivity is a condensate of Cooper pairs with internal degrees of freedom such as spin, orbital angular momentum, and center-of-mass momentum. Therefore, unconventional superconductivity is accompanied by an additional symmetry breaking other than U(1) gauge symmetry breaking. Such additional symmetry breaking leads to various intriguing superconducting phenomena. For example, chiral p-wave superconductivity with spontaneous time-reversal symmetry breaking realizes topological superconductivity possessing Majorana fermions at the surface [2, 3], which is currently attracting much attention as a possible platform of decoherence-free topological quantum computation [4].

Especially, exotic superconducting phenomena have been clarified in the presence of parity/space-inversion symmetry ($\mathcal{P}$-symmetry) breaking. In noncentrosymmetric (NCS) superconductors, the lack of the global parity symmetry in the crystal structure leads to a variety of exotic superconducting phenomena. Similarly, local parity violation in the crystal structure also induces exotic superconducting phenomena although the parity symmetry is globally maintained. The interplay of superconductivity and other parity-breaking orders, e.g., ferroelectric order, is also an interesting topic that is not yet clarified so much. Furthermore, we can consider spontaneous parity symmetry breaking induced by superconductivity itself. In the following, we will uncover novel properties of superconductors associated with such various kinds of parity symmetry breaking.

This chapter is dedicated to the introduction to the recent progress in the research field of

exotic superconductivity associated with parity symmetry breaking. In Sec. 1.1, we introduce basic properties of superconductivity in globally/locally NCS crystals. Especially, as a guiding principle, we focus on the selection rule for globally/locally NCS superconductors in the presence of spin-orbit coupling (SOC). In Sec. 1.2, we overview recent progress in the research field of superconductors correlated with other parity-breaking orders. In Sec. 1.3, we discuss the parity symmetry breaking induced by the spontaneous ordering of mixed-parity superconductivity. Finally, the organization of this thesis is explained in Sec. 1.4.

1.1 Superconductivity in globally/locally noncentrosymmetric crystals

The effects of the parity symmetry breaking in NCS crystals (Fig. 1.1) on the electronic properties can be represented as the *antisymmetric spin-orbit coupling*

$$\mathcal{H}_{\text{ASOC}} = \sum_{\boldsymbol{k},s,s'} (\boldsymbol{g_k} \cdot \boldsymbol{\sigma})_{ss'} c_{\boldsymbol{k}s}^{\dagger} c_{\boldsymbol{k}s'}, \tag{1.1}$$

where $\boldsymbol{\sigma} = (\sigma_x, \sigma_y, \sigma_z)$ is the vector of Pauli matrices, and $c_{\boldsymbol{k}s}$ is the annihilation operator for an electron with momentum $\boldsymbol{k}$ and spin $s = \uparrow, \downarrow$. $\boldsymbol{g_k}$ is the so-called g-vector satisfying $\boldsymbol{g_{-k}} = -\boldsymbol{g_k}$. The antisymmetric SOC affects the Cooper pairing in NCS superconductors and causes various intriguing superconducting phenomena, e.g., parity-mixing of Cooper pairs [5], topological superconductivity [6–8], upper critical fields exceeding the Pauli limit [9–11], helical superconductivity [12–15], Edelstein effect [16–22], and superconducting diode effect [23–28].
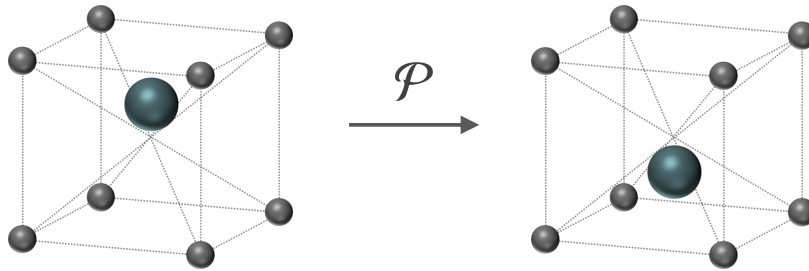
Fig. 1.1. Example of NCS crystal structure. The crystal structure after the space-inversion $\mathcal{P}$ does not coincide with the original crystal structure.

We here introduce the *selection rule* for superconductivity in NCS crystals. The selection rule is a guiding principle when we consider Cooper pairing in NCS superconductors with antisymmetric SOC. To see this, we consider the effective mean-field Hamiltonian in the matrix

form:

$$\mathcal{H} = \frac{1}{2} \sum_{k} (\hat{c}_{k}^{\dagger}, \hat{c}_{-k}^{\mathrm{T}}) \begin{pmatrix} H_0(\boldsymbol{k}) & \Delta(\boldsymbol{k}) \\ \Delta^{\dagger}(\boldsymbol{k}) & -H_0^*(-\boldsymbol{k}) \end{pmatrix} \begin{pmatrix} \hat{c}_{k} \\ \hat{c}_{-k}^* \end{pmatrix}, \tag{1.2}$$

where $\hat{c}_{k}^{\dagger} \equiv (c_{k\uparrow}^{\dagger}, c_{k\downarrow}^{\dagger})$. In NCS crystals with antisymmetric SOC, the normal state part $H_0(\boldsymbol{k})$ is described as

$$H_0(\boldsymbol{k}) = \epsilon_{\boldsymbol{k}} \sigma_0 + \boldsymbol{g}_{\boldsymbol{k}} \cdot \boldsymbol{\sigma}, \tag{1.3}$$

where σ_0 is the 2×2 unit matrix. On the other hand, the pairing potential $\Delta(\boldsymbol{k})$ is generally expressed as

$$\Delta(\boldsymbol{k}) = (\psi_{\boldsymbol{k}} \sigma_0 + \boldsymbol{d}_{\boldsymbol{k}} \cdot \boldsymbol{\sigma}) i \sigma_y. \tag{1.4}$$

To derive the selection rule, we now introduce the concept of *superconducting fitness* [29, 30], which quantifies the stability of superconducting states under symmetry-breaking fields. The superconducting fitness $F(\boldsymbol{k})$ is defined as

$$F(\boldsymbol{k}) U_T = H_0(\boldsymbol{k}) \Delta(\boldsymbol{k}) - \Delta(\boldsymbol{k}) H_0^*(-\boldsymbol{k}), \tag{1.5}$$

where U_T is the unitary part of the time-reversal operator (i.e., $U_T = i\sigma_y$ for spin-1/2 single-orbital model). If $H_0(\boldsymbol{k})$ and $\Delta(\boldsymbol{k})$ satisfy $F(\boldsymbol{k}) \neq 0$, the system possesses finite *interband pairing* which gives suppression of the superconducting transition temperature [29, 30]. Hence, the presence of a finite value of $F(\boldsymbol{k})$ is detrimental to the superconductivity. In this sense, the superconducting fitness $F(\boldsymbol{k})$ is a measure to quantify the incompatibility of arbitrary pairing states with a given normal state Hamiltonian. Applying Eq. (1.5) to Eqs. (1.3) and (1.4), we obtain

$$F(\boldsymbol{k}) = 2i(\boldsymbol{g}_{\boldsymbol{k}} \times \boldsymbol{d}_{\boldsymbol{k}}) \cdot \boldsymbol{\sigma}. \tag{1.6}$$

Equation (1.6) indicates that spin-triplet superconducting states are destabilized by the antisymmetric SOC except when $\boldsymbol{d}_{\boldsymbol{k}}$ is parallel to $\boldsymbol{g}_{\boldsymbol{k}}$, while the spin-singlet superconducting states are not affected by the antisymmetric SOC. These facts lead to the selection rule for NCS superconductors summarized in Table 1.1 (a). Since parity is not a good quantum number in NCS crystals, mixed-parity superconducting states with spin-singlet and spin-triplet pairing components are generally realized. In such mixed-parity superconducting states, symmetry of spin-triplet component is restricted so as to satisfy the above selection rule (i.e., $\boldsymbol{d}_{\boldsymbol{k}} \parallel \boldsymbol{g}_{\boldsymbol{k}}$).

Next, we consider the impacts of locally NCS crystal structure on superconductivity. Figure 1.2 shows examples of locally NCS crystal structure. As shown in Fig. 1.2, locally NCS

Table 1.1. Selection rule for superconductivity in globally/locally NCS crystals.

(a) Globally NCS crystal	
SOC	Selection rule
$g_k \cdot \sigma$	intrasublattice singlet, triplet ($d_k \parallel g_k$)

(b) Locally NCS crystal		
SOC	Selection rule	
$(g'_k \cdot \sigma) \otimes \tau_z$	intrasublattice singlet, triplet ($d_k^\mu \parallel g'_k$)	intersublattice triplet ($d_k^\mu \perp g'_k$)

lattices possess non-equivalent sublattices and the inversion center is not located at the sub-lattices. This indicates that the global parity symmetry is preserved by interchanging two sublattices, while the local parity symmetry is broken at each sublattice. In such locally NCS crystals, a sublattice-dependent antisymmetric SOC appears as

$$\mathcal{H}_{\text{sASOC}} = \sum_{k,s,s'} (g'_k \cdot \sigma)_{ss'} (c^\dagger_{kas} c_{kas'} - c^\dagger_{kbs} c_{kbs'}), \tag{1.7}$$

where c_{kms} is the annihilation operator for an electron with withmomentum k and spin $s = \uparrow, \downarrow$ on sublattice $m = a, b$. The g-vector g'_k satisfies $g'_{-k} = -g'_k$. The sublattice-dependent antisymmetric SOC plays a key role to realize various exotic phenomena in locally NCS superconductors, e.g., singlet-triplet mixed pairing states [31], pair density wave states [32, 33], complex stripe states [34], and topological superconductivity [35–37]. To see the selection rule for locally NCS superconductors, we now consider the mean-field Hamiltonian given by Eq. (1.2) with $\hat{c}^\dagger_k \equiv (c^\dagger_{ka\uparrow}, c^\dagger_{ka\downarrow}, c^\dagger_{kb\uparrow}, c^\dagger_{kb\downarrow})$. The normal state part $H_0(k)$ with the sublattice-dependent staggered antisymmetric SOC is described as

$$H_0(k) = \epsilon_k \sigma_0 \otimes \tau_0 + g'_k \cdot \sigma \otimes \tau_z, \tag{1.8}$$

where τ_μ ($\mu = 0, x, y, z$) denotes the Pauli matrix for the sublattice degrees of freedom. The general form of the pairing potential $\Delta(k)$ is written as

$$\Delta(k) = \sum_{\mu=0,x,y,z} (\psi_k^\mu \sigma_0 + d_k^\mu \cdot \sigma) i\sigma_y \otimes \tau_\mu. \tag{1.9}$$

Applying Eq. (1.5) to Eqs. (1.8) and (1.9), we can obtain the superconducting fitness $F(k)$ in locally NCS superconductors. Owing to the sublattice degrees of freedom, the superconducting fitness is decomposed into intrasublattice and intersublattice components as $F(k) = F_{\text{intra}}(k) + F_{\text{inter}}(k)$. The intrasublattice and intersublattice superconducting fitness $F_{\text{intra}}(k)$ and $F_{\text{inter}}(k)$
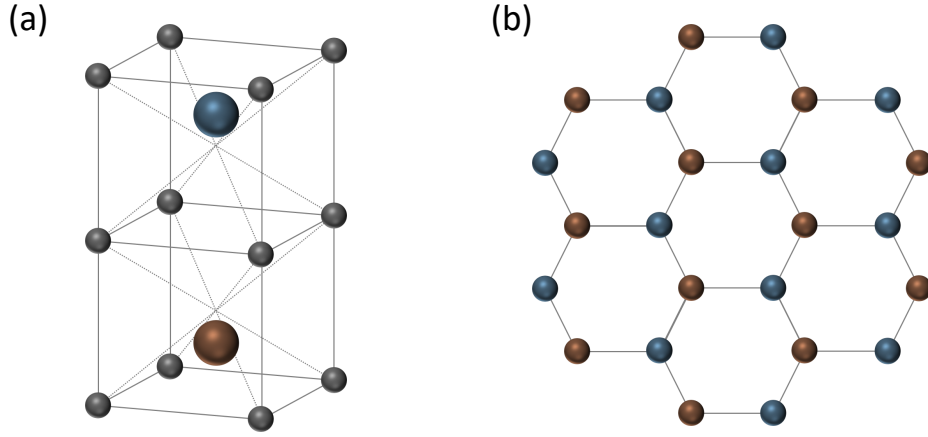
Fig. 1.2. Examples of locally NCS crystal structure. Two non-equivalent sublattices are described as blue and red spheres. (a) The crystal structure is formed by stacking inversion-symmetry lacking blocks in a staggered way. (b) Top view of the honeycomb lattice structure.

are obtained as follows:

$$F_{\text{intra}}(\boldsymbol{k}) = 2i \left[(\boldsymbol{g}'_{\boldsymbol{k}} \times \boldsymbol{d}^0_{\boldsymbol{k}}) \cdot \boldsymbol{\sigma} \otimes \tau_z + (\boldsymbol{g}'_{\boldsymbol{k}} \times \boldsymbol{d}^z_{\boldsymbol{k}}) \cdot \boldsymbol{\sigma} \otimes \tau_0 \right], \tag{1.10}$$

$$F_{\text{inter}}(\boldsymbol{k}) = 2i \left[(\boldsymbol{g}'_{\boldsymbol{k}} \cdot \boldsymbol{d}^x_{\boldsymbol{k}}) \sigma_0 \otimes \tau_y - (\boldsymbol{g}'_{\boldsymbol{k}} \cdot \boldsymbol{d}^y_{\boldsymbol{k}}) \sigma_0 \otimes \tau_x \right]$$
$$+ 2i \left[\psi^x_{\boldsymbol{k}} (\boldsymbol{g}'_{\boldsymbol{k}} \cdot \boldsymbol{\sigma}) \otimes \tau_y - \psi^y_{\boldsymbol{k}} (\boldsymbol{g}'_{\boldsymbol{k}} \cdot \boldsymbol{\sigma}) \otimes \tau_x \right]. \tag{1.11}$$

From Eqs. (1.10) and (1.11), we can derive the selection rule for locally NCS supercodncutors summarized in Table 1.1 (b). For intrasublattice pairing, spin-triplet superconducting states are destabilized by the antisymmetric SOC except when $\boldsymbol{d}^{0,z}_{\boldsymbol{k}}$ is parallel to $\boldsymbol{g}'_{\boldsymbol{k}}$, while the intra-sublattice spin-singlet superconducting states are not affected by the antisymmetric SOC. This result is same with that for globally NCS superconductors. On the other hand, for intersublattice pairing, only the spin-triplet superconducting states are stabilized when $\boldsymbol{d}^{x,y}_{\boldsymbol{k}}$ is perpendicular to $\boldsymbol{g}'_{\boldsymbol{k}}$. Superconductivity in locally NCS crystals obeys the above selection rule in general [31, 38]. However, since superconducting fitness is a concept based on the mean-field theory, the selection rule can be violated if the superconductivity is described by a theoretical framework beyond the mean-field theory. We will indeed encounter such a situation in Chap. 3.

1.2   Superconductivity and parity-breaking order

The interplay between superconductivity and other electric/magnetic orders has attracted much attention in the research field of unconventional superconductivity. In high-T_{c} cuprates and heavy-fermion superconductors [39–41], *d*-wave superconductivity induced by antiferromagnetic spin fluctuations has been elucidated. Spin-triplet superconductivity mediated by ferro-
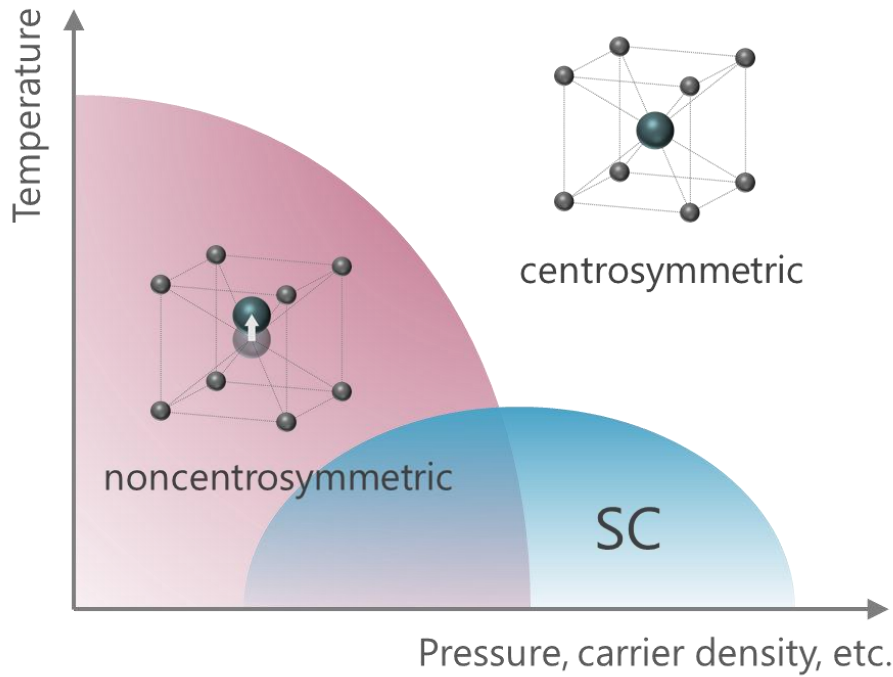
Fig. 1.3. Schematic phase diagram for superconductivity in the vicinity of a parity-breaking quantum critical point. The quantum criticality of the parity-breaking order is controlled by tuning a physical parameter such as pressure and carrier density. Superconductivity is driven by Cooper pairing mediated by the quantum fluctuation of the parity-breaking order.

magnetic (FM) spin fluctuations has been studied in uranium-based FM superconductors such as UGe_2, URhGe, and UCoGe [42]. In iron-based superconductors, charge/orbital-fluctuation-driven s_{++}-wave superconductivity has been clarified [43, 44]. In recently discovered kagome metals, the interplay between superconductivity and charge density waves is drawing attention [45–47].

In particular, recent theoretical studies have clarified exotic correlations between superconductivity and other parity-breaking orders. These theoretical works treat a system in which superconductivity and parity-breaking order are adjacent as shown in Fig. 1.3. In the disordered state of the parity-breaking order, superconductivity mediated by the quantum fluctuation of the parity-breaking order, which we call *parity-breaking fluctuation*, has been elucidated. For spin-orbit coupled isotropic systems, it has been clarified that the nonmagnetic parity-breaking fluctuations (i.e., odd-parity electric multipole fluctuations) generate an odd-parity pairing interaction competing with the conventional s-wave pairing interaction [48]. Hence, the odd-parity superconductivity can be stabilized by the nonmagnetic parity-breaking fluctuations when the s-wave pairing is suppressed by external Zeeman field or Coulomb repulsion. The essence of this pioneering work is a direct coupling between the parity-breaking order parameter and the electron's spin texture on the Fermi surface, which appears in the presence of SOC [49]. This theoretical framework was further extended to both crystalline systems and systems with mag-

6

netic parity-breaking fluctuations [50]. The idea proposed in Ref. [48] was applied to explain the pairing mechanism of superconductivity induced by ferroelectric soft modes [51–54]. In addition, it has been clarified that odd-parity topological superconductivity is realized by an antiferromagnetic spin fluctuation in locally NCS crystals, which effectively acts as a magnetic parity-breaking fluctuation (i.e., odd-parity magnetic multipole fluctuation) [38]. On the other hand, intriguing phenomena have also been clarified in the coexistent states of superconductivity and parity-breaking order. In a coexistent phase of superconductivity and odd-parity magnetic quadrupole order, the stabilization of Fulde-Ferrell-Larkin-Ovchinnikov (FFLO) superconducting state without external magnetic field has been proposed [55, 56]. For spin-orbit-coupled superconductors in the vicinity of the ferroelectric critical point, it has been clarified that coexistent state of superconductivity and ferroelectric-like parity-breaking order, which we call ferroelectric superconducting state, is stabilized in a very low carrier density regime or high magnetic field regime [57]. In Chap. 2, we show that the ferroelectric superconducting state induces exotic phenomena such as topological superconductivity and odd-frequency pairing in the presence of multiorbital/multiband effects.

At present, the above theoretical proposals are not yet established experimentally. One of the reasons is that there are few candidate materials realizing superconductivity in the vicinity of parity-breaking critical point (e.g., $SrTiO_3$ [58, 59] and $Cd_2Re_2O_7$ [60, 61]) like shown in Fig. 1.3. Although such experimental difficulty is present, exploration of the correlation between superconductivity and parity-breaking order should give valuable insights to the research field of unconventional superconductivity.

1.3 Mixed-parity superconductivity

Now that we have reviewed the interplay of superconductivity and parity symmetry breaking due to the crystal structure or other parity-breaking orders, we here consider spontaneous parity symmetry breaking realized by superconductivity itself. Superconductivity gives stiffness under the U(1) gauge transformation. Hence, we need to take into account combined operations operations of usual symmetry operations and U(1) gauge transformation in order to consider symmetry in superconducting states. This means that odd-parity superconductivity does not break the parity symmetry because the combined $\mathcal{P} \times$ U(1) symmetry is preserved. On the other hand, if the superconductivity possesses a mixed-parity order parameter (e.g., $s + p$-wave order parameter), the parity symmetry is spontaneously broken by the superconducting transition. Spontaneous ordering of such *mixed-parity superconductivity* can be realized when even- and odd-parity pairing instabilities are competing in one system. Especially, it has been clarified that time-reversal symmetry ($\mathcal{T}$-symmetry) breaking mixed-parity superconductivity (e.g., $s + ip$-wave superconductivity) is energetically favored in such situations [8, 62, 63]. Hereafter, we refer to this kind of $\mathcal{P}$- and $\mathcal{T}$-breaking superconducting states as $\mathcal{PT}$-*symmetric mixed-parity*

superconductivity since it preserves the combined $\mathcal{PT}$-symmetry.

To see this, we consider a simplified Hamiltonian for mixed-parity superconductivity as follows:

$$H_0(\boldsymbol{k}) = (\epsilon_{\boldsymbol{k}} - \mu)\sigma_0, \tag{1.12}$$

$$\Delta(\boldsymbol{k}) = (e^{i\phi}\Delta_1\hat{\psi}_{\boldsymbol{k}}\sigma_0 + \Delta_2\hat{\boldsymbol{d}}_{\boldsymbol{k}} \cdot \boldsymbol{\sigma})i\sigma_y, \tag{1.13}$$

where μ is the chemical potential and $\Delta_{1,2}$ represents the superconducting order parameter for the even/odd-parity pairing channels. ϕ is the phase difference between the even- and odd-parity pairing order parameters. Without loss of generality, we assume Δ_1 and Δ_2 are real. The real-valued coefficients $\hat{\psi}_{\boldsymbol{k}}$ and $\hat{\boldsymbol{d}}_{\boldsymbol{k}}$ express the momentum-dependence of even- and odd-parity pairing channels. The above Hamiltonian can be diagonalized as

$$\begin{pmatrix} H_0(\boldsymbol{k}) & \Delta(\boldsymbol{k}) \\ \Delta^\dagger(\boldsymbol{k}) & -H_0^*(-\boldsymbol{k}) \end{pmatrix} \rightarrow \mathrm{diag}\left(E_{\boldsymbol{k}}^+, E_{\boldsymbol{k}}^-, -E_{-\boldsymbol{k}}^+, -E_{-\boldsymbol{k}}^-\right), \tag{1.14}$$

where the energy spectrum $E_{\boldsymbol{k}}^\pm$ is given by

$$E_{\boldsymbol{k}}^\pm = \sqrt{(\epsilon_{\boldsymbol{k}} - \mu)^2 + (\Delta_1^2\hat{\psi}_{\boldsymbol{k}}^2 \pm 2\Delta_1\Delta_2\hat{\psi}_{\boldsymbol{k}}|\hat{\boldsymbol{d}}_{\boldsymbol{k}}|\cos\phi + \Delta_2^2|\hat{\boldsymbol{d}}_{\boldsymbol{k}}|^2)}. \tag{1.15}$$

From Eq. (1.15), we can derive the Landau free energy as follows:

$$\mathcal{F} = \alpha_1\Delta_1^2 + \alpha_2\Delta_2^2 + \beta_1\Delta_1^4 + \beta_2\Delta_2^4 + 2\tilde{\beta}(2 + \cos 2\phi)\Delta_1^2\Delta_2^2. \tag{1.16}$$

The coefficients are obtained as

$$\alpha_1 = \rho_0\langle\hat{\psi}_{\boldsymbol{k}}^2\rangle_{\mathrm{FS}}(T - T_{\mathrm{c}1})/T_{\mathrm{c}1}, \tag{1.17}$$

$$\alpha_2 = \rho_0\langle|\hat{\boldsymbol{d}}_{\boldsymbol{k}}|^2\rangle_{\mathrm{FS}}(T - T_{\mathrm{c}2})/T_{\mathrm{c}2}, \tag{1.18}$$

$$\beta_1 = \rho_0\langle\hat{\psi}_{\boldsymbol{k}}^4\rangle_{\mathrm{FS}}7\zeta(3)/(16\pi^2T^2), \tag{1.19}$$

$$\beta_2 = \rho_0\langle|\hat{\boldsymbol{d}}_{\boldsymbol{k}}|^4\rangle_{\mathrm{FS}}7\zeta(3)/(16\pi^2T^2), \tag{1.20}$$

$$\tilde{\beta} = \rho_0\langle\hat{\psi}_{\boldsymbol{k}}^2|\hat{\boldsymbol{d}}_{\boldsymbol{k}}|^2\rangle_{\mathrm{FS}}7\zeta(3)/(16\pi^2T^2), \tag{1.21}$$

where ρ_0 is the density of states (DOS) at the Fermi energy, $\langle\cdots\rangle_{\mathrm{FS}}$ denotes the average over the Fermi surface, $\zeta(x)$ is the Riemann zeta function, and T is the temperature. $T_{\mathrm{c}1}$ and $T_{\mathrm{c}2}$ denote the superconducting transition temperature for even- and odd-parity pairing channels, respectively. By assuming $\alpha_1 \simeq \alpha_2$, we consider the case when even- and odd-parity pairing instabilities are comparable in strength, and hence tuning some physical parameters (e.g., pressure, chemical substitution) can drive multiple superconducting phase transitions. Now, we consider the possibility of the coexistence of even- and odd-parity pairing orders. Since the last

term in Eq. (1.16) is minimized when $\phi = \pm\pi/2$, spontaneous time-reversal symmetry breaking is energetically favored if the coexistent mixed-parity phase is stable. For $\phi = \pm\pi/2$, the free energy (1.16) becomes

$$\mathcal{F} = \alpha_1 \Delta_1^2 + \alpha_2 \Delta_2^2 + \beta_1 \Delta_1^4 + \beta_2 \Delta_2^4 + 2\tilde{\beta}\Delta_1^2\Delta_2^2. \tag{1.22}$$

For this free energy, the thermodynamically stable states must satisfy the following relations:

$$\partial_{\Delta_1}\mathcal{F} = 2\Delta_1 \left[\alpha_1 + 2\beta_1 \Delta_1^2 + 2\tilde{\beta}\Delta_2^2 \right] = 0, \tag{1.23}$$

$$\partial_{\Delta_2}\mathcal{F} = 2\Delta_2 \left[\alpha_2 + 2\beta_2 \Delta_2^2 + 2\tilde{\beta}\Delta_1^2 \right] = 0. \tag{1.24}$$

Nonzero solutions of the above simultaneous equations are obtained as

$$(\Delta_1, \Delta_2) = \begin{cases} \left(\sqrt{\dfrac{-\alpha_1}{2\beta_1}}, 0 \right) \equiv (\Delta_1^{\text{even}}, 0), \\[3mm] \left(0, \sqrt{\dfrac{-\alpha_2}{2\beta_2}} \right) \equiv (0, \Delta_2^{\text{odd}}), \\[3mm] \left(\sqrt{\dfrac{\alpha_1\beta_2 - \alpha_2\tilde{\beta}}{2(\tilde{\beta}^2 - \beta_1\beta_2)}}, \sqrt{\dfrac{\alpha_2\beta_1 - \alpha_1\tilde{\beta}}{2(\tilde{\beta}^2 - \beta_1\beta_2)}} \right) \equiv (\Delta_1^{\text{mix}}, \Delta_2^{\text{mix}}). \end{cases} \tag{1.25}$$

From Eq. (1.25), we see that there are three possible superconducting states for the free energy (1.22); (i) even-parity superconducting state with $(\Delta_1, \Delta_2) = (\Delta_1^{\text{even}}, 0)$, (ii) odd-parity superconducting state with $(\Delta_1, \Delta_2) = (0, \Delta_2^{\text{odd}})$, and (iii) mixed-parity superconducting state with $(\Delta_1, \Delta_2) = (\Delta_1^{\text{mix}}, \Delta_2^{\text{mix}})$. To determine the most stable state, we substitute the solutions (1.25) into the free energy (1.22) and compare the results:

$$\mathcal{F}[\Delta_1^{\text{mix}}, \Delta_2^{\text{mix}}] - \mathcal{F}[\Delta_1^{\text{even}}, 0] = \frac{(\alpha_1\tilde{\beta} - \alpha_2\beta_1)^2}{4\beta_1(\tilde{\beta}^2 - \beta_1\beta_2)}, \tag{1.26}$$

$$\mathcal{F}[\Delta_1^{\text{mix}}, \Delta_2^{\text{mix}}] - \mathcal{F}[0, \Delta_2^{\text{odd}}] = \frac{(\alpha_2\tilde{\beta} - \alpha_1\beta_2)^2}{4\beta_2(\tilde{\beta}^2 - \beta_1\beta_2)}. \tag{1.27}$$

Equations (1.26) and (1.27) indicates that the coexistent mixed-parity phase with $(\Delta_1, \Delta_2) = (\Delta_1^{\text{mix}}, \Delta_2^{\text{mix}})$ is most stable because we find $\tilde{\beta}^2 < \beta_1\beta_2$ holds from Eqs. (1.19)-(1.21). Note that $\tilde{\beta}^2 < \beta_1\beta_2$ also ensures that Δ_1^{mix} and Δ_2^{mix} are real. Therefore, the free energy (1.22) leads to the stabilization of the $\mathcal{PT}$-symmetric mixed-parity coexistent phase with $\phi = \pm\pi/2$. In Chap. 4, we will clarify exotic phenomena induced by the spontaneous ordering of such $\mathcal{PT}$-symmetric mixed-parity superconductivity.

1.4   Organization of this thesis

In this thesis, we clarify a variety of exotic superconducting phenomena associated with parity symmetry breaking. In Chap. 2, we study a coexistent phenomenon of superconductivity and ferroelectric-like parity-breaking order, which we call the ferroelectric superconductivity (FESC). Based on numerical calculations and symmetry analysis of a multiorbital model, we clarify the unusual cooperating effect between superconductivity and ferroelectricity, which leads to exotic properties such as topological Weyl superconductivity and odd-frequency pairing. In Chap. 3, we investigate an interplay of unconventional superconductivity and locally NCS crystal structure by using a bilayer triangular lattice Hubbard model. By performing numerical calculations within the framework of the strong coupling theory of superconductivity, it is shown that the combination of FM spin fluctuation and sublattice-dependent antisymmetric SOC generates multiple odd-parity pairing instabilities. In Chap. 4, we demonstrate novel properties of $\mathcal{PT}$-symmetric mixed-parity superconductivity, which simultaneously breaks the space-inversion and time-reversal symmetries. Focusing on the multiband effects, we clarify that such superconducting states generally possess unusual asymmetric Bogoliubov spectrum, which induces stabilization of FFLO-like nonuniform superconducting state at a zero magnetic field. Finally, the obtained results are summarized in Chap. 5.

Chapter 2

Ferroelectric superconductivity and multiorbital/multiband effects: application to SrTiO$_3$

2.1   Introduction

For a long time, it has been widely believed that conductivity and ferroelectricity can not coexist in one system because the static electric fields are screened by conduction electrons. However, recent experiments revealed the existence of ferroelectric metals (e.g., LiOsO$_3$ [64] and WTe$_2$ [65, 66]), in which a ferroelectric-like (polar-nonpolar) structural phase transition occurs in the metallic state.

The discovery of the ferroelectric metals also generated a flurry of interests in the possibility of the coexistence of ferroelectricity[1] and superconductivity, namely FESC. At present, only SrTiO$_3$ (STO) is considered as a promising candidate realizing FESC. Superconductivity in STO emerges in a very low carrier density regime on the order of 10^{17} cm^{-3} [67–69], where the pairing mechanism cannot be captured by conventional Migdal-Eliashberg theory due to extreme retardation effects. Although various pairing interactions (e.g., plasmons [70, 71], localized longitudinal optical phonons [72, 73]) have been proposed to explain the persistence of superconductivity in the dilute density limit, the issue of the pairing mechanism has not yet been settled. On the other hand, STO is a quantum paraelectric [74] existing in the vicinity of the ferroelectric quantum critical point [75]. The avoided ferroelectric ordering can be activated by some chemical or physical operations, e.g., isovalent substitution of Sr with Ca [76], isotopic substitution of ^{16}O with ^{18}O [77], and application of tensile strain [78] or electric field [79].

---

[1]In the following part of this thesis, we will use the terms "ferroelectricity" and "ferroelectric" to describe the spontaneous inversion symmetry breaking accompanied by the appearance of a polar axis. Note that this usage is different from conventional definition of ferroelectricity for insulating materials since the switchability of polarization is not required. Indeed, at present, the electric-field-switchable ferroelectric metal is not discovered other than WTe$_2$ [65, 66].

This ferroelectric instability of STO also motivated proposals of pairing scenarios related to optical phonons mediating FE fluctuations [50, 51, 53, 54, 80–85]. Indeed, enhancement of the superconducting transition temperature by a ferroelectric quantum fluctuation was proposed theoretically [80], and later confirmed experimentally [58, 86–89]. Furthermore, a phase transition structurally indistinguishable from the ferroelectric phase transition was observed in dilute superconducting Sr$_{1-x}$Ca$_x$TiO$_{3-\delta}$ [58] and strained STO thin films [59]. These experimental observations suggested the existence of the ferroelectric superconducting states and stimulated theoretical study for FESC [57, 90].

Another important aspect regarding the superconductivity in STO is its multiorbital/multiband nature. The conduction bands in STO originate from three Ti t_{2g} orbitals. Three-fold degeneracy of the t_{2g} orbitals is lifted by the SOC and the tetragonal crystal field due to antiferrodistortive rotation of TiO$_6$ octahedra below 105 K [91]. Thus, STO has three distinct bands all centered at the Γ-point and constructed from multiple orbitals [see Fig. 2.3 for reference]. Therefore, the multiorbital features may affect superconductivity even in the dilute carrier density regime with single Fermi surface. Consequently, the superconductivity in doped STO has multiorbital character regardless of the carrier density. The issue of multiple superconducting bands and gaps in STO is also a subject of debate. Early tunneling measurements on doped STO observed two peaks in the local DOS [92] which implies the multiple superconducting gaps. This result is supported by recent quantum oscillation measurements [68] and thermal conductivity data [93]. Thus, it has been suggested that STO is a multiband superconductor with multiple nodeless gaps, and the multiband effect has been theoretically discussed [94–96]. In contrast, recent tunneling experiments [97] and optical conductivity data [98] indicate only single superconducting gap.

Considering all the unique aspects of the superconducting STO, in this chapter, we show that STO can be a platform of the FESC through two different mechanisms that rely on the SOC. The first mechanism originates from the ferroelectricity-induced Lifshitz transition in dilute carrier density regimes. Another one is the magnetic-field-induced FESC caused by spin-momentum locking in the ferroelectric phase. It is shown that, in both mechanisms, the FESC is strongly influenced by the multiorbital/multiband nature of STO. In particular, we predict that the combination of the FESC and multiorbital/multiband effects leads to topological Weyl superconductivity and odd-frequency pairing.

The rest of this chapter is organized as follows. In Sec. 2.2, we summarize a basic idea to describe FESC in theory. In Sec. 2.3, model and formulation for analyzing the FESC in STO are provided. In Sec. 2.4, we demonstrate the multiorbital/multiband effect on the electronic structure and superconductivity in STO. In Sec. 2.5, we show the magnetic field-temperature phase diagrams for the FESC in three different carrier density regimes in STO. In Sec. 2.6, we study the multiorbital odd-frequency pairing in the ferroelectric superconducting phase. Finally, we summarize this chapter in Sec. 2.7.

2.2 Theoretical approach to ferroelectric superconductivity

In insulators, ferroelectric instability is explained by the competition between long-range Coulomb forces (which favor the polar ferroelectric phase) and short-range repulsions (which favor the nonpolar paraelectric phase) [99]. However, in superconductors, the long-range Coulomb forces are screened by the conduction electrons. Therefore, we need to find out an alternative way to stabilize the ferroelectric order in the presence of superconductivity.

A possible coupling that favors the ferroelectric/polar superconducting phase originates from the SOC. As explained in Sec. 1.1, the combination of inversion symmetry breaking and SOC leads to the emergence of the antisymmetric SOC. Especially, a polar inversion symmetry breaking induces the so-called Rashba-type antisymmetric SOC which is expressed as

$$\mathcal{H}_{\text{RSOC}} = \alpha \sum_{\boldsymbol{k},s,s'} c^{\dagger}_{\boldsymbol{k},s} [\boldsymbol{e}_{\text{pol}} \cdot (\boldsymbol{k} \times \boldsymbol{\sigma})]_{ss'} c_{\boldsymbol{k},s'}, \tag{2.1}$$

where $\boldsymbol{e}_{\text{pol}}$ denotes a unit vector along the polar axis. Therefore, the ferroelectric phase transition (i.e., spontaneous polar inversion symmetry breaking) should be accompanied by the appearance of Rashba-type SOC. This means that the Rashba-type SOC is dynamically induced in the momentum space by a spontaneous polar lattice displacement in the real space as depicted in Fig 2.1. Based on this idea, we rewrite Eq. (2.1) as

$$\mathcal{H}_{\text{pol}} = \tilde{\alpha} P \sum_{\boldsymbol{k},s,s'} c^{\dagger}_{\boldsymbol{k},s} [\boldsymbol{e}_{\text{pol}} \cdot (\boldsymbol{k} \times \boldsymbol{\sigma})]_{ss'} c_{\boldsymbol{k},s'}, \tag{2.2}$$

where we replaced $\alpha \rightarrow \tilde{\alpha} P$ with P being the magnitude of the polar lattice displacement in the ferroelectric phase. Thus, Eq. (2.2) expresses an effective coupling between conduction electrons, which form Cooper pairs in the superconducting state, and polar lattice displacement (i.e., ferroelectricity)[2]. In our previous work using a simplified single-orbital model [57], it has been clarified that the FESC is indeed realized by the feedback effect of superconductivity on the ferroelectricity induced by the Rashba-type coupling (2.2).

---

[2]In the same spirit, one can consider a direct coupling between conduction electrons and transverse optical phonons in the presence of SOC as follows:

$$\mathcal{H}^{\text{TO}}_{\text{el-ph}} = \lambda_{\text{TO}} \sum_{\boldsymbol{k},\boldsymbol{q},s,s'} c^{\dagger}_{\boldsymbol{k}+\boldsymbol{q},s} [\boldsymbol{u}_{\boldsymbol{q}} \cdot (\boldsymbol{k} \times \boldsymbol{\sigma})]_{ss'} c_{\boldsymbol{k},s'}, \tag{2.3}$$

where $\boldsymbol{u}$ is a transverse displacement vector. Recently, the effective pairing interaction that arises from the coupling (2.3) is expected to give significant impacts on the superconductivity in the vicinity of the ferroelectric quantum critical point, which is characterized by a softening of the transverse optical modes. Indeed, some theoretical works clarified that such pairing interaction induces exotic superconducting phenomena such as anisotropic superconductivity [51] and topological superconductivity [52]. The microscopic origin of the coupling (2.3) is recently discussed based on multiorbital models [53, 54].
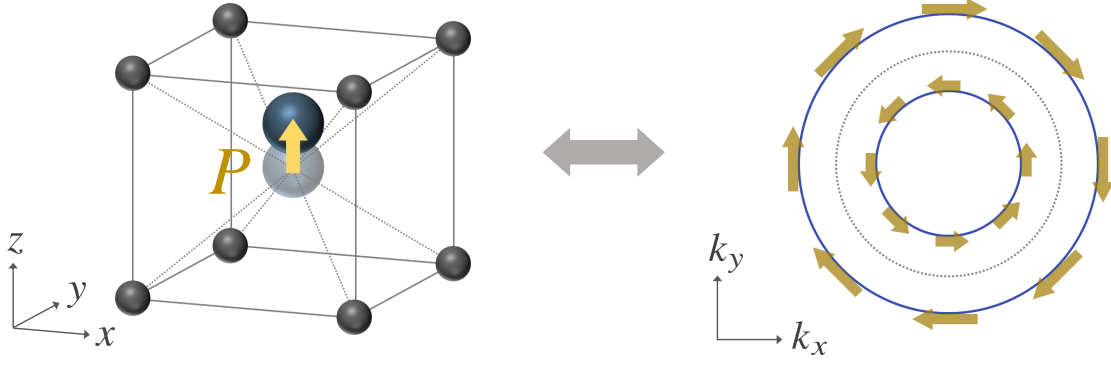
Fig. 2.1. Schematic illustration for the relationship between the polar lattice displacement P (left figure) and the accompanied Rashba-type SOC (right figure). The polar lattice displacement associated with the ferroelectric-like phase transition induces Rashba-type spin-orbit splitting of the band structure (Fermi surface) in the momentum space.

2.3 Model and formulation

2.3.1 Three-orbital model for SrTiO₃

In order to describe the three distinct band structure in tetragonal STO, we introduce a three-orbital tight-binding model for t_{2g} electrons as follows:

$$\mathcal{H}_{\text{STO}} = \sum_{\boldsymbol{k},l,s} \left(\varepsilon_l(\boldsymbol{k}) - \mu\right) c^{\dagger}_{\boldsymbol{k},ls} c_{\boldsymbol{k},ls} + \frac{\lambda}{2} \sum_{\boldsymbol{k},l,l',s,s'} \left(\boldsymbol{\ell}_{ll'} \cdot \boldsymbol{\sigma}_{ss'}\right) c^{\dagger}_{\boldsymbol{k},ls} c_{\boldsymbol{k},l's'}, \tag{2.4}$$

where $c_{\boldsymbol{k},ls}$ is the annihilation operator for an electron with momentum $\boldsymbol{k}$, orbital $l = 1, 2, 3$, and spin $s = \uparrow, \downarrow$. d_{yz}, d_{xz}, d_{xy} orbitals are denoted by the orbital index $l = 1, 2, 3$, respectively. The first term is the kinetic-energy term of t_{2g} orbitals including the chemical potential μ. The single electron kinetic energy $\varepsilon_l(\boldsymbol{k})$ are described as

$$\varepsilon_1(\boldsymbol{k}) = -2t_1 \left(\cos k_y + \cos k_z\right) - 2t_2 \cos k_x - 4t_3 \cos k_y \cos k_z, \tag{2.5}$$

$$\varepsilon_2(\boldsymbol{k}) = -2t_1 \left(\cos k_x + \cos k_z\right) - 2t_2 \cos k_y - 4t_3 \cos k_x \cos k_z, \tag{2.6}$$

$$\varepsilon_3(\boldsymbol{k}) = -2t_1 \left(\cos k_x + \cos k_y\right) - 2t_2 \cos k_z - 4t_3 \cos k_x \cos k_y + \Delta_{\text{T}}. \tag{2.7}$$

Here, Δ_{T} expresses the tetragonal crystal field for the antiferrodistortive transition, which lifts the energy of the d_{xy} orbital. The second term of Eq. (2.4) represents the LS coupling of Ti ions. Here, $\ell^a_{bc} \equiv i\epsilon_{abc}$ is the completely antisymmetric tensor representing the projection of

Table 2.1. Model parameters for bulk STO. We choose the unit of energy as $t_1 = 1$. The values of Δ_T and λ are set to be larger than the literature values [101–103] for simplicity of the numerical calculations. The value of γ at the SrTiO$_3$/LaAlO$_3$ interface [103] is also shown for reference.

	Literature values [101–103]	This paper
t_1	277 meV	1
t_2	31 meV	0.11
t_3	76 meV	0.27
Δ_T	3.2 meV	0.03
λ	12 meV	0.12
γ	20 meV (SrTiO$_3$/LaAlO$_3$)	$\lesssim 0.20$

the $L = 2$ angular momentum operator onto the t_{2g} orbital subspace[3]. The band structure of tetragonal STO is reproduced by $\mathcal{H}_{STO}$[4] with the parameter set listed in Table 2.1, which is determined based on the first principles calculations [101–103].

Then, we discuss effects of the ferroelectricity on the electronic structure. The ferroelectric transition in STO is realized by opposite displacement of Sr/Ti cation and O anion, and thus the crystal symmetry descends to one of polar space groups. Although STO has two ferroelectric modes parallel and perpendicular to the antiferrodistortive rotation axis [104], we only consider the former for simplicity. Thus, the crystallographic space group of tetragonal STO descends to $I4cm$ (C_{4v}^{10}) from $I4/mcm$ (D_{4h}^{18}) as a consequence of the ferroelectric ordering along the [001] axis [105]. In this mirror symmetry broken ferroelectric phase, a spin-independent odd-parity orbital hybridization term

$$\mathcal{H}_{pol} = 2\gamma \sum_{\boldsymbol{k},l,l',s} \boldsymbol{e}_{pol} \cdot (\boldsymbol{\ell}_{ll'} \times \boldsymbol{w}(\boldsymbol{k})) c_{\boldsymbol{k},ls}^{\dagger} c_{\boldsymbol{k},l's}, \tag{2.11}$$

is induced in addition to $\mathcal{H}_0$ [102]. Here, $\boldsymbol{e}_{pol} \equiv (0,0,1)$ and $\boldsymbol{w}(\boldsymbol{k}) \equiv (\sin k_x, \sin k_y, \sin k_z)$. As illustrated in Fig. 2.2, Equation (2.11) describes the intersite hybridization between d_{xy} and $d_{yz,xz}$ orbitals, which have different mirror parity along the [001] axis. Combination of $\mathcal{H}_{pol}$ and

---

[3]In matrix form, the operator $\boldsymbol{\ell} = (\ell^x, \ell^y, \ell^z)$ is described as

$$\ell^x = \begin{pmatrix} 0 & 0 & 0 \\ 0 & 0 & i \\ 0 & -i & 0 \end{pmatrix}, \quad \ell^y = \begin{pmatrix} 0 & 0 & -i \\ 0 & 0 & 0 \\ i & 0 & 0 \end{pmatrix}, \quad \ell^z = \begin{pmatrix} 0 & i & 0 \\ -i & 0 & 0 \\ 0 & 0 & 0 \end{pmatrix}, \tag{2.8}$$

where the basis elements are $|d_{yz}\rangle$, $|d_{xz}\rangle$, and $|d_{xy}\rangle$.

[4]In general, we should consider an intersite hybridization term

$$\mathcal{H}_{hyb} = \sum_{\boldsymbol{k},l,l',s} v_{ll'}(\boldsymbol{k}) c_{\boldsymbol{k},ls}^{\dagger} c_{\boldsymbol{k},l's}, \tag{2.9}$$

$$v_{ll'}(\boldsymbol{k}) = v_{l'l}(\boldsymbol{k}) = 4t' \sin k_l \sin k_l', \tag{2.10}$$

for perovskite oxides [100] in addition to the above two terms. However, first-principles band calculations have shown that it is negligible in the bulk STO [101–103], and hence we neglect $\mathcal{H}_{hyb}$ in this study.
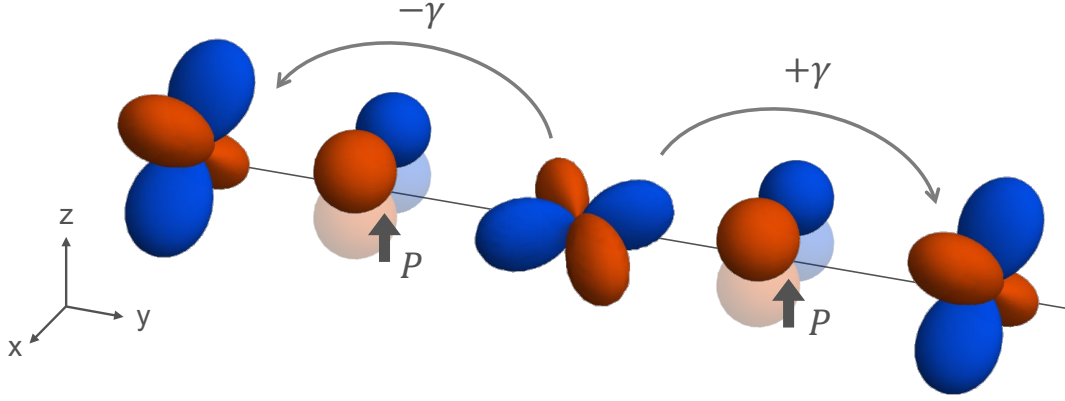
Fig. 2.2. Illustration of the odd-parity orbital hybridization processes in the ferroelectric phase of STO. A polar lattice displacement P induces interorbital hopping γ between the t_{2g} orbitals of nearest neighbor Ti atoms. This orbital hybridization is mediated by the p orbitals of the bridging O atom and changes sign along the Ti-O-Ti bond. For example, a polar displacement P along the crystalline z-axis couples the d_{xy} and d_{xz} orbitals along the y-axis via the p_x orbitals.

the LS coupling leads to the Rashba SOC [103, 106], and thus spin-orbit splitting in the band structure is induced in the ferroelectric phase [Fig. 2.3]. In addition, the magnitude of the Rashba SOC is roughly proportional to the odd-parity hopping integral γ (see Appendix A). Therefore, based on the discussion in Sec. 2.2, we consider that the odd-parity orbital hybridization (2.11) is dynamically induced by the polar lattice displacement P in the ferroelectric phase. Hence, we assume $\gamma \propto P$ and treat γ as an order parameter that characterizes the ferroelectricity in STO. In Appendix C, we discuss possible experimental signatures of the ferroelectricity-induced odd-parity orbital hybridization.

As explained in Sec. 2.1, the origin of superconductivity in STO is still under debate. However, thermodynamic properties such as the specific heat jump are in good agreement with the BCS theory [93] and the ratio of the superconducting gap Δ_0 to the transition temperature T_c is close to the BCS value $2\Delta_0/k_B T_c \simeq 3.54$ [97, 98, 107]. Therefore, we investigate an interplay of superconductivity and ferroelectricity by adopting a simple BCS-type model, and focus on the multiorbital effect on the FESC in STO. More precise studies including a realistic dynamical electron-phonon coupling and Coulomb interactions are left for a future study. The BCS-type static attractive interaction is introduced as follows:

$$\mathcal{H}_{\text{pair}} = -\frac{V_s}{N} \sum_{\boldsymbol{k},\boldsymbol{k}',\boldsymbol{q},l} c^\dagger_{\boldsymbol{k},l\uparrow} c^\dagger_{-\boldsymbol{k}+\boldsymbol{q},l\downarrow} c_{-\boldsymbol{k}'+\boldsymbol{q},l\downarrow} c_{\boldsymbol{k}',l\uparrow}, \tag{2.12}$$

where N is the number of Ti sites, and $\boldsymbol{q}$ is the center-of-mass momentum of Cooper pairs. Since the s-wave superconductivity in STO has been confirmed [93], we assume momentum-independent intraorbital pairing interaction. The pairing interaction strength V_s is determined to satisfy $T_c \ll E_{\text{SO}}$, where E_{SO} is a typical energy of the spin-orbit splitting. This condition
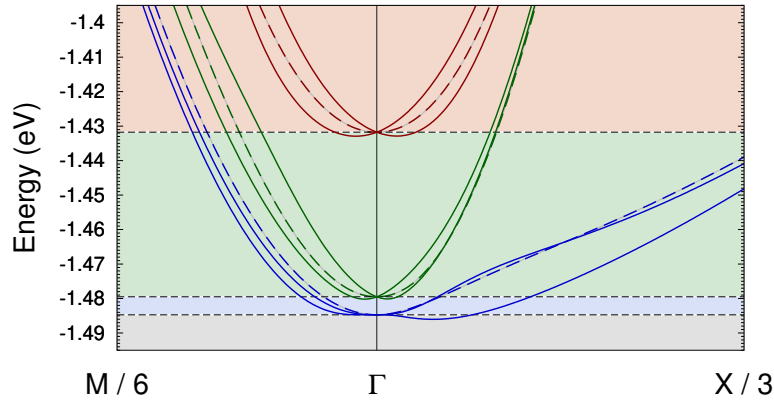
Fig. 2.3. Band structure of bulk STO around the Γ-point in the paraelectric phase (dashed line; $\gamma = 0$) and the ferroelectric phase (solid line; $\gamma = 27.7$ meV). The Lifshitz transitions occur when the Fermi level crosses black dashed lines. Different colored areas show different carrier density regimes which are distinguished by the topology of Fermi surfaces.

is reasonable in STO since the superconducting transition temperature is extremely small, i.e., about 0.3 K. Then, the Rashba splitting in the ferroelectric phase significantly affects the superconductivity. Here, we neglect the interorbital pairing because the interorbital interaction is generally weak and does not alter qualitative results. Furthermore, we ignore the parity mixing of Cooper pairs in the ferroelectric phase, since the stability of FESC is hardly affected by an induced *p*-wave component.

The impact of the applied magnetic field is included as the Zeeman coupling term,

$$\mathcal{H}_Z = -\mu_B \sum_{\boldsymbol{k},l,s,s'} \boldsymbol{H} \cdot \boldsymbol{\sigma}_{ss'} c^\dagger_{\boldsymbol{k},ls} c_{\boldsymbol{k},ls'}, \tag{2.13}$$

where μ_B is the Bohr magneton. In the superconducting STO, the superfluid density n_s is small [108], and hence the penetration depth $\lambda_L \propto n_s^{-1/2}$ is large. Thus, STO is a superconductor close to type-II limit with an extremely large Ginzburg-Landau parameter $\kappa_{GL} \gg 1$. Therefore, it is justified to assume a uniform magnetic field in the bulk superconducting STO. It would be desirable to include the gauge interaction with the vector potential in addition to the Zeeman coupling term $\mathcal{H}_Z$. The importance of the orbital depairing effect is represented by the Maki parameter $\alpha_M \propto \Delta/\epsilon_F$, where Δ is the superconducting gap and ϵ_F is the Fermi energy. When $\alpha_M > 1$, the orbital depairing effect is suppressed and the superconducting state is destroyed mainly due to the Pauli depairing effect. In the superconducting STO, ϵ_F is extremely small and hence α_M can be large. Thus, we assume that the orbital depairing effect is not qualitatively important in the dilute superconducting STO. Indeed, the upper critical field exceeding the Pauli limit in some doped STO [89, 109] indicates a strong impact of the Pauli depairing effect on the superconductivity. In the following, we fix the magnetic field in a direction parallel to the polar [001] axis, i.e., $\boldsymbol{H} = (0, 0, H_z)$. Thus, an asymmetric deformation of the Rashba split Fermi

surface, which is destructive for the FESC [57], is not induced under the magnetic field.

2.3.2 Mean-field theory for superconductivity

We investigate the superconductivity in STO by means of the mean-field theory. In the following discussion, we fix $\boldsymbol{q} = \boldsymbol{0}$ since FFLO superconductivity with finite $\boldsymbol{q}$ is not stabilized in our model when the magnetic field is applied along the polar axis. The pairing interaction $\mathcal{H}_{\text{pair}}$ is approximated as

$$
\begin{aligned}
\mathcal{H}_{\text{pair}} &= -\frac{V_s}{N} \sum_{\boldsymbol{k},\boldsymbol{k}',l} c^\dagger_{\boldsymbol{k},l\uparrow} c^\dagger_{-\boldsymbol{k},l\downarrow} c_{-\boldsymbol{k}',l\downarrow} c_{\boldsymbol{k}',l\uparrow} \\
&\approx \sum_{\boldsymbol{k},l} \left(\Delta_l c^\dagger_{\boldsymbol{k},l\uparrow} c^\dagger_{-\boldsymbol{k},l\downarrow} + \text{H.c.} \right) + \frac{N}{V_s} \sum_l |\Delta_l|^2,
\end{aligned}
\tag{2.14}
$$

by introducing the orbital-dependent superconducting order parameters,

$$
\Delta_l = -\frac{V_s}{N} \sum_{\boldsymbol{k}} \langle c_{-\boldsymbol{k},l\downarrow} c_{\boldsymbol{k},l\uparrow} \rangle.
\tag{2.15}
$$

To describe the total Hamiltonian $\mathcal{H} = \mathcal{H}_{\text{STO}} + \mathcal{H}_{\text{pol}} + \mathcal{H}_{\text{Z}} + \mathcal{H}_{\text{pair}}$ in a matrix form, we define the vector operator as follows:

$$
\hat{c}^\dagger_{\boldsymbol{k}} = (c^\dagger_{\boldsymbol{k},1\uparrow}, c^\dagger_{\boldsymbol{k},1\downarrow}, c^\dagger_{\boldsymbol{k},2\uparrow}, c^\dagger_{\boldsymbol{k},2\downarrow}, c^\dagger_{\boldsymbol{k},3\uparrow}, c^\dagger_{\boldsymbol{k},3\downarrow}).
\tag{2.16}
$$

Then, we obtain the mean-field Hamiltonian in the matrix form

$$
\mathcal{H} = \frac{1}{2} \sum_{\boldsymbol{k}} (\hat{c}^\dagger_{\boldsymbol{k}}, \hat{c}^{\text{T}}_{-\boldsymbol{k}}) H(\boldsymbol{k}) \begin{pmatrix} \hat{c}_{\boldsymbol{k}} \\ \hat{c}^*_{-\boldsymbol{k}} \end{pmatrix} + E_0
\tag{2.17}
$$

$$
E_0 = \frac{N}{V_s} \sum_l |\Delta_l|^2 + \sum_{\boldsymbol{k},l} \left(\varepsilon_l(\boldsymbol{k}) - \mu \right).
\tag{2.18}
$$

The Bogoliubov-de Gennes (BdG) Hamiltonian $H(\boldsymbol{k})$ is described as

$$
H(\boldsymbol{k}) = \begin{pmatrix} H_0(\boldsymbol{k}) & \Delta(\boldsymbol{k}) \\ \Delta^\dagger(\boldsymbol{k}) & -H_0^{\text{T}}(-\boldsymbol{k}) \end{pmatrix},
\tag{2.19}
$$

by using the normal state part

$$
H_0(\boldsymbol{k}) = \begin{pmatrix} \xi_1(\boldsymbol{k})\sigma_0 - h_z\sigma_z & \frac{\lambda}{2}i\sigma_z & -\frac{\lambda}{2}i\sigma_y + \gamma w_x(\boldsymbol{k})\sigma_0 \\ -\frac{\lambda}{2}i\sigma_z & \xi_2(\boldsymbol{k})\sigma_0 - h_z\sigma_z & \frac{\lambda}{2}i\sigma_x + \gamma w_y(\boldsymbol{k})\sigma_0 \\ \frac{\lambda}{2}i\sigma_y + \gamma w_x^*(\boldsymbol{k})\sigma_0 & -\frac{\lambda}{2}i\sigma_x + \gamma w_y^*(\boldsymbol{k})\sigma_0 & \xi_3(\boldsymbol{k})\sigma_0 - h_z\sigma_z \end{pmatrix},
\tag{2.20}
$$

and the pairing part

$$\Delta(\boldsymbol{k}) = \begin{pmatrix} \Delta_1 i\sigma_y & 0 & 0 \\ 0 & \Delta_2 i\sigma_y & 0 \\ 0 & 0 & \Delta_3 i\sigma_y \end{pmatrix}. \tag{2.21}$$

Here, we abbreviate as $\xi_l(\boldsymbol{k}) \equiv \varepsilon_l(\boldsymbol{k}) - \mu$ and $h_z \equiv \mu_{\mathrm{B}} H_z$.

Then, we carry out the Bogoliubov transformation

$$c_{\boldsymbol{k},ls} = \sum_{\nu,\tau} \left(u^{(\nu\tau)}_{\boldsymbol{k},ls} \alpha_{\boldsymbol{k},\nu\tau} - v^{(\nu\tau)*}_{-\boldsymbol{k},ls} \alpha^{\dagger}_{-\boldsymbol{k},\nu\tau} \right), \tag{2.22}$$

$$c^{\dagger}_{-\boldsymbol{k},ls} = \sum_{\nu,\tau} \left(v^{(\nu\tau)}_{\boldsymbol{k},ls} \alpha_{\boldsymbol{k},\nu\tau} + u^{(\nu\tau)*}_{-\boldsymbol{k},ls} \alpha^{\dagger}_{-\boldsymbol{k},\nu\tau} \right), \tag{2.23}$$

where $\alpha_{\boldsymbol{k},\nu\tau}$ is the annihilation operator for a Bogoliubov quasiparticle with momentum $\boldsymbol{k}$, pseudoorbital $\nu = 1, 2, 3$, and pseudospin $\tau = \uparrow, \downarrow$. Thus, Eq. (2.15) is rewritten as

$$\Delta_l = -\frac{V_s}{N} \sum_{\boldsymbol{k},\nu,\tau} \left(u^{(\nu\tau)}_{\boldsymbol{k},l\uparrow} v^{(\nu\tau)*}_{\boldsymbol{k},l\downarrow} f[E_{\nu\tau}(\boldsymbol{k})] - u^{(\nu\tau)}_{\boldsymbol{k},l\downarrow} v^{(\nu\tau)*}_{\boldsymbol{k},l\uparrow} f[-E_{\nu\tau}(\boldsymbol{k})] \right), \tag{2.24}$$

where $f[E]$ is the Fermi-Dirac distribution function and $E_{\nu\tau}(\boldsymbol{k})$ is the energy of a Bogoliubov quasiparticle. Equations (2.24) are the simultaneous gap equations to be solved numerically. In the Bogoliubov quasiparticle picture, the total Hamiltonian is described as

$$\mathcal{H} = \sum_{\boldsymbol{k},\nu,\tau} E_{\nu\tau}(\boldsymbol{k}) \left(\alpha^{\dagger}_{\boldsymbol{k},\nu\tau} \alpha_{\boldsymbol{k},\nu\tau} - \frac{1}{2} \right) + E_0. \tag{2.25}$$

Therefore, the electronic free energy per Ti site is obtained as

$$\Omega_{\mathrm{ele}}[\boldsymbol{\Delta}, P] = -\frac{1}{N\beta} \sum_{\boldsymbol{k},\nu,\tau} \left[\ln \left(1 + e^{-\beta E_{\nu\tau}(\boldsymbol{k})} \right) + \frac{\beta E_{\nu\tau}(\boldsymbol{k})}{2} \right] + \mu n + \frac{E_0}{N}, \tag{2.26}$$

where $\boldsymbol{\Delta} = (\Delta_1, \Delta_2, \Delta_3)$ and $\beta = 1/T$ is the inverse temperature. The last term of Eq. (2.26) is necessary since the carrier density per Ti site is fixed as n instead of the chemical potential μ. Using $\boldsymbol{\Delta}$ obtained by solving Eqs. (2.24), we calculate the electronic part of the free energy $\mathcal{F}_{\mathrm{ele}}[\boldsymbol{\Delta}, P]$ from Eq. (2.26).

2.3.3 Polar instability

In order to discuss the ferroelectric-like structural phase transition, we take into account the Landau free energy arising form polar lattice distortion as follows:

$$\Omega_{\mathrm{lat}}[P] = \frac{1}{2}\kappa_2 P^2 + \frac{1}{4}\kappa_4 P^4 + \frac{1}{6}\kappa_6 P^6, \tag{2.27}$$

where κ_2, κ_4, and κ_6 are the lattice parameters which describe the elasticity of the lattice. The temperature dependence of the lattice parameters is ignored, consistent with the fact that the dielectric constant is almost temperature-independent in the quantum paraelectric STO [74].

The total free energy including the contributions of both electrons and lattice is given by

$$\Omega[\Delta, P] = \Omega_{\text{ele}}[\Delta, P] + \Omega_{\text{lat}}[P]. \tag{2.28}$$

The thermodynamically stable state is determined by minimizing the free energy $\Omega[\Delta, P]$ with respect to Δ and P. The ferroelectric superconducting state is stabilized when both Δ and P have finite values. The values of the phenomenological lattice parameters κ_2, κ_4, and κ_6 are determined as follows. The lattice parameters κ_4 and κ_6 are introduced to cut off the ferroelectric order parameter $\gamma \propto P$ in a realistic regime. In this study, we set κ_4 and κ_6 so as to satisfy $\gamma/t_1 \lesssim 0.20$ in agreement with the first-principles estimation of γ for the SrTiO₃/LaAlO₃ interface [103]. The choice of κ_4 and κ_6 hardly alters the results of this study. The value of κ_2 is determined so as to realize a paraelectric normal state near a ferroelectric phase transition point. This condition expresses a situation of the paraelectric STO which is moved toward the vicinity of the ferroelectric quantum critical point, for example, by Ca substitution [76] or isotopic substitution of O[77]. Then, we investigate the feasibility of a ferroelectric transition caused by the superconductivity.

The phenomenological parameters κ_2, κ_4, and κ_6 might be derived from the microscopic Hamiltonian for the optical phonon excitations coupled to the conduction electrons, in which the ferroelectric transition should be driven by the dipolar interaction [83, 110]. They are phenomenologically introduced in this study, and more microscopic study for the ferroelectricity in the superconducting STO is left for a future work.

2.4 Multiorbital/multiband effect

Before showing results for the FESC, we here clarify effects of the multiorbital/multiband electronic structure in STO.

2.4.1 Unconventional Rashba spin-orbit coupling

First, we investigate the multiorbital effect on the Rashba spin-orbit splitting in the ferroelectric STO. We elucidate the nature of the Rashba SOC by calculating the energy spectrum in the normal state $\mathcal{E}_\alpha^\pm(\boldsymbol{k})$ ($\alpha = 1, 2, 3$) [$\mathcal{E}_\alpha^-(\boldsymbol{k}) \leq \mathcal{E}_\alpha^+(\boldsymbol{k})$ and $\mathcal{E}_\alpha^\pm(\boldsymbol{k}) \leq \mathcal{E}_{\alpha'}^\pm(\boldsymbol{k})$ for $\alpha < \alpha'$] and wave functions. In the presence of the inversion symmetry ($\gamma = 0$), the two-fold Kramers degeneracy holds as $\mathcal{E}_\alpha^-(\boldsymbol{k}) = \mathcal{E}_\alpha^+(\boldsymbol{k})$ at zero magnetic fields. On the other hand, Rashba-type spin-orbit splitting is induced by the polar inversion symmetry breaking ($\gamma \neq 0$) as $\mathcal{E}_\alpha^-(\boldsymbol{k}) < \mathcal{E}_\alpha^+(\boldsymbol{k})$
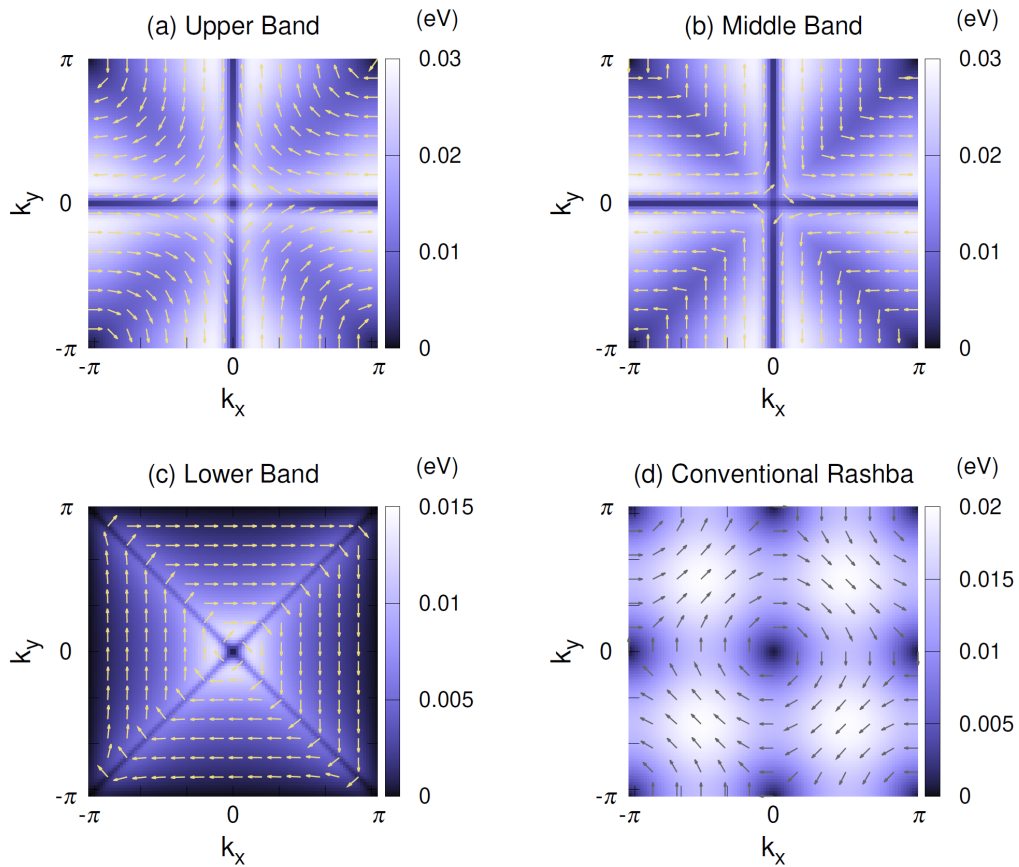
Fig. 2.4. The magnitude of the spin-orbit splitting in the (a) upper band, (b) middle band, and (c) lower band at $k_z = 0$ with $\gamma/t_1 = 0.105$. The arrows show the direction of the g-vector. (d) $\boldsymbol{k}$ dependence of the conventional Rashba SOC given by Eq. (2.30) with $\gamma/t_1 = 0.105$.

except for at the time-reversal invariant momentum. Spin direction of each Rashba split bands is calculated by taking the average $\boldsymbol{S}_\alpha(\boldsymbol{k}) = \langle \sum_l \sum_{\sigma,\sigma'} \boldsymbol{\sigma}_{\sigma\sigma'} c^\dagger_{\boldsymbol{k},l\sigma} c_{\boldsymbol{k},l\sigma'} \rangle_\alpha$ for the wave function of the α-th band. Figures 2.4(a)-(c) show the magnitude of the spin-orbit splitting $\delta\mathcal{E}_\alpha(\boldsymbol{k}) = \mathcal{E}^+_\alpha(\boldsymbol{k}) - \mathcal{E}^-_\alpha(\boldsymbol{k})$ and the direction of the g-vector defined as $\boldsymbol{g}_\alpha(\boldsymbol{k}) = \delta\mathcal{E}_\alpha(\boldsymbol{k})\boldsymbol{S}_\alpha(\boldsymbol{k})$ for each Rashba split bands. Note that the upper, middle, and lower bands are denoted by $\alpha = 3, 2$, and 1, respectively. We see that the $\boldsymbol{k}$-dependence of the Rashba spin-orbit splitting in STO is significantly different from that of the conventional Rashba SOC with $\boldsymbol{g}(\boldsymbol{k}) = (\sin k_y, -\sin k_x, 0)$ [Fig. 2.4(d)]. The spin-orbit splitting in the lower band is large at $\boldsymbol{k}$ slightly away from the Γ-M line, whereas that in the middle or upper band is large at $\boldsymbol{k}$ slightly away from the Γ-X line. In particular, the spin-orbit splitting in the lower band is maximized near the Γ-point where the spin-orbit splitting of the conventional Rashba SOC is tiny. Moreover, the g-vectors of the lower and middle bands are almost parallel to the [100] or [010] axis, and rapidly rotates by $\pi/2$ at the Γ-M line. The origin of this unconventional Rashba SOC is explained by combined analysis of the perturbation expansion for the LS coupling and the basis transformation to the total angular momentum space [see Appendix A]. The unconventional Rashba SOC characteristic of the multiorbital system gives impacts on superconductivity, as we show below.

2.4.2 Enhanced upper critical field of dilute superconductivity

Next, we discuss an impact of the multiorbital electronic structure on the dilute superconductivity in STO. As shown in Sec. 2.4.1, unconventional Rashba SOC is induced by ferroelectricity as a consequence of the multiorbital effect. Unlike the conventional Rashba effect, the Rashba splitting in the lower band is maximized near the Γ-point [Fig. 2.4(c)]. On the other hand, the Pauli depairing effect of a Rashba superconductor is suppressed under a magnetic field parallel to the polar axis [9, 10, 16, 111, 112]. This is because the BCS-type Cooper pairing is possible even under the magnetic field thanks to the Rashba-type spin-momentum locking. Thus, it is implied that the Pauli depairing effect in a dilute superconducting state with a tiny Fermi surface should be strongly suppressed compared to the case of a conventional Rashba superconductor.

To test the above expectation, we introduce a simple Hamiltonian with conventional Rashba SOC as follows:

$$\tilde{\mathcal{H}} = \tilde{\mathcal{H}}_0 + \mathcal{H}_Z + \mathcal{H}_{\text{pair}}, \tag{2.29}$$

$$\tilde{\mathcal{H}}_0 = \sum_{\boldsymbol{k},l,s} (\varepsilon_l(\boldsymbol{k}) - \mu) c^\dagger_{\boldsymbol{k},ls} c_{\boldsymbol{k},ls} + \alpha \sum_{\boldsymbol{k},l,s,s'} \boldsymbol{g}(\boldsymbol{k}) \cdot \boldsymbol{\sigma}_{ss'} c^\dagger_{\boldsymbol{k},ls} c_{\boldsymbol{k},ls'}, \tag{2.30}$$

where the g-vector is assumed to be $\boldsymbol{g}(\boldsymbol{k}) = (\sin k_y, -\sin k_x, 0)$ and diagonal in the orbital space. Based on the perturbation analysis for the LS coupling [see Eq. (A.8) in Appendix A], we assume $\alpha = 2\lambda\gamma/t_1$ in the following discussion. Here, we compare this model with our

three-orbital model for STO to illuminate the multiorbital effect which is appropriately taken into account in the latter. Figure 2.5(a) shows the temperature dependence of the upper critical
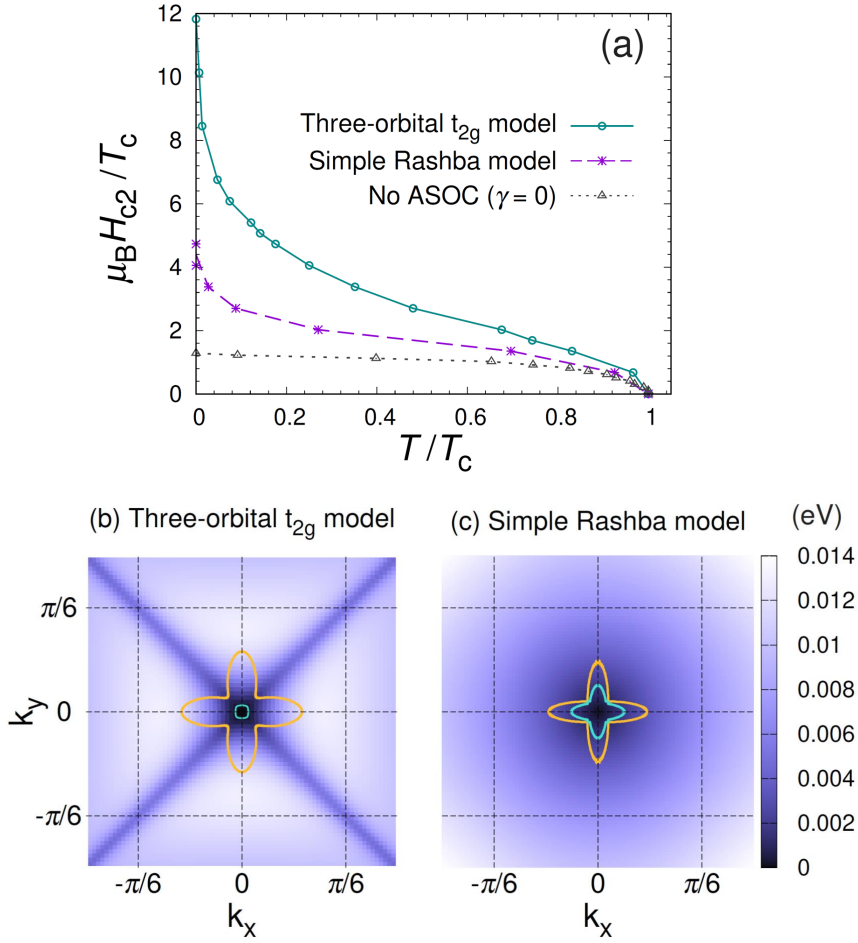
**Fig. 2.5.** (a) The temperature dependence of the upper critical field $\mu_B H_{c2}$. The magnetic filed is applied along the [001] axis. The green solid line (purple dashed line) shows the upper critical field calculated for the three-orbital model (simple Rashba model). The gray dotted line shows the upper critical field of the three-orbital model with $\gamma = 0$. (b) and (c) Illustration of the Fermi surface and the magnitude of the spin-orbit splitting of the lower band for the (b) three-orbital model and (c) simple Rashba model. The carrier density and odd-parity hopping integral are set to $n = 5.0 \times 10^{-5}$ and $\gamma/t_1 = 0.105$, respectively.

field $\mu_B H_{c2}$ in the dilute single-band regime ($n = 5.0 \times 10^{-5}$) where the Fermi surface is only composed of the lower band. Since the lattice constant of STO ~ 3.905 Å is chosen as the unit of length, $n = 5.0 \times 10^{-5}$ corresponds to 8.40×10^{17} cm^{-3}. The paring interaction is chosen to $V_s/t_1 = 0.28$, hence the superconducting transition temperature is set to $T_c = 0.00098 t_1 \sim 3.0$ K at $\gamma = 0$ and $H_z = 0$. When we adopt $\gamma = 0.105 t_1$, a typical energy of spin-orbit splitting is $E_{SO} \sim \lambda \gamma / t_1 \sim 0.01$. Then, $T_c \ll E_{SO}$ is satisfied and the effect of the Rashba splitting is reflected to the superconductivity. Note that the superconducting transition temperature is set to be larger than the realistic value $T_c \sim 0.3$ K of doped STO to reduce the cost of

23

numerical calculation. In both models, the upper critical field of the NCS superconductivity with Rashba splitting (green solid line and purple dashed line) is enhanced compared to that of the centrosymmetric superconductivity without SOC (gray dotted line). Furthermore, we see that the upper critical field of the three-orbital model for STO [Eqs. (2.4) and (2.11)] is larger than that of the simple Rashba model [Eq. (2.29)]. The origin of this enhanced upper critical field can be attributed to the Fermi surface anisotropy and large spin-orbit splitting. As shown in Figs. 2.5(b) and 2.5(c), the Fermi surfaces of the lower band show $d_{x^2-y^2}$-wave like anisotropy. The unconventional Rashba SOC in the three-orbital model induces a large spin-orbit splitting particularly in the region near $k \parallel [100]$. The DOS at the Fermi energy mainly comes from this region. Furthermore, the magnitude of the spin-orbit splitting is maximized near the Γ-point, where the Fermi surfaces in the dilute region are located [Fig. 2.5(b)]. Therefore, the upper critical field is drastically enhanced thanks to the strong spin-momentum locking on the Fermi surface. In contrast, the conventional Rashba SOC induces a small spin-orbit splitting around the Γ-point as shown in Fig. 2.5(c). Thus, the enhancement of the upper critical field by spin-orbit splitting is less pronounced than that in the three-orbital model.

2.4.3 Lifshitz transitions and superconductivity

In this section, we discuss the ferroelectricity-induced Lifshitz transition and its effect on superconductivity. Upon decreasing the carrier density in the ferroelectric phase, the Fermi energy becomes lower than the crossing point of the spin-orbit split bands at the Γ-point [see Fig. 2.3], and thus the topology of Fermi surfaces is changed in stages. These Lifshitz transitions enhance the DOS due to an effective reduction of dimensionality [113], and leads to the stabilization of a ferroelectric superconducting state [57].
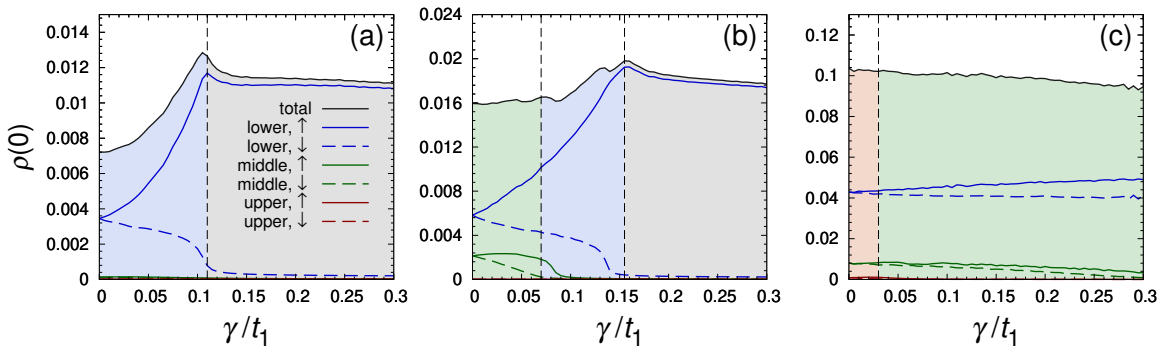
Fig. 2.6. DOS at the Fermi energy $\rho(0)$ as a function of the odd-parity hopping integral γ. The partial DOS for the Rashba split t_{2g} bands are also shown. The black dashed vertical lines represent the Lifshitz transition point. Different colored regions indicate different phases which are distinguished by the Lifshitz transitions. The colors correspond to the background colors in Fig. 2.3. The carrier density is set to (a) $n = 5.0 \times 10^{-5}$, (b) $n = 2.0 \times 10^{-4}$, and (c) $n = 1.0 \times 10^{-2}$, respectively.
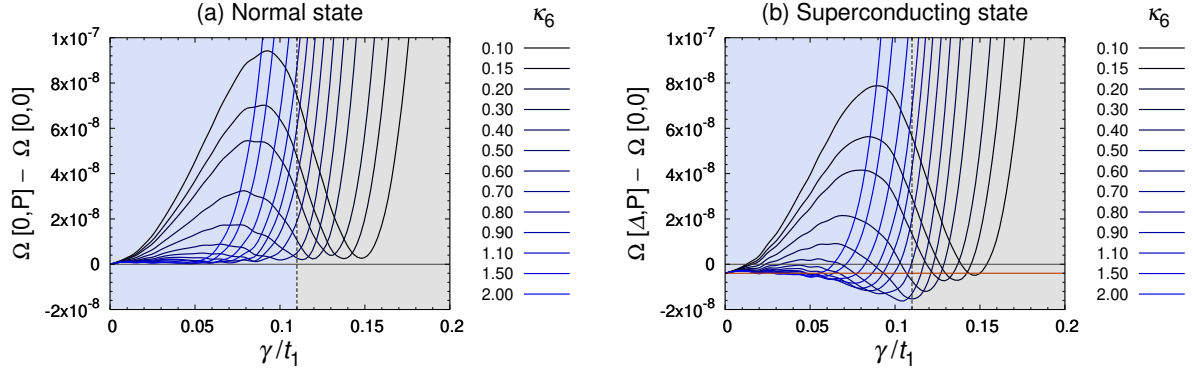
Fig. 2.7. The free energy as a function of the odd-parity hopping integral γ for several values of the cutoff lattice parameter κ_6. The carrier density is set to $n = 5.0 \times 10^{-5}$, i.e., a single-band regime. The other lattice parameters are chosen as $(\kappa_2, \kappa_4) = (6.75 \times 10^{-5}, 0)$. The temperature and magnetic field are set to $T = 1.0 \times 10^{-10}$ and $\boldsymbol{H} = 0$, respectively. The black dashed vertical line shows the Lifshitz transition point. (a) $\gamma \propto P$ dependence of $\delta\Omega[0, P] = \Omega[0, P] - \Omega[0, 0]$. Since $\delta\Omega[0, P] > 0$ is satisfied in the whole range of κ_6, the paraelectric normal state is realized. (b) $\gamma \propto P$ dependence of $\delta\Omega[\Delta, P] = \Omega[\Delta, P] - \Omega[0, 0]$. The stabilization condition of the ferroelectric superconducting state, i.e., $\delta\Omega[\Delta, P] < \delta\Omega[\Delta, 0] < 0$, is satisfied under the red horizontal line.

Figure 2.6 shows the DOS at the Fermi energy $\rho(0)$ as a function of γ. In the single-band regime ($n = 5.0 \times 10^{-5}$), $\rho(0)$ is maximized at the Lifshitz transition point of the lowest band $\gamma = \gamma_{c1}$ [Fig. 2.6(a)], thanks to the effective reduction of the dimensionality. Consequently, the superconductivity is enhanced at the Lifshitz transition point γ_{c1}. Figure 2.7(b) shows the $\gamma \propto P$ dependence of the ferroelectric superconducting condensation energy $\delta\Omega[\Delta, P] = \Omega[\Delta, P] - \Omega[0, 0]$ for various values of the cutoff lattice parameter κ_6. Here, Δ is optimized under fixed P. We see that the stabilization condition of the ferroelectric superconducting sate, i.e., $\delta\Omega[\Delta, P] < \delta\Omega[\Delta, 0] < 0$, is satisfied in a wide range of lattice parameters, although the normal state is paraelectric [see Fig. 2.7(a)]. This means that the FESC is stable at zero magnetic field in the dilute region.

Next, we discuss the effects of Lifshitz transitions of the middle and upper bands. When the Fermi energy in the paraelectric phase is slightly higher than the bottom of the bands, the Lifshitz transition is induced by the ferroelectricity. However, we see that these Lifshitz transitions are not significantly reflected in the total DOS $\rho(0)$ [Figs. 2.6(b) and 2.6(c)]. Although the partial DOS for the middle or upper band is enhanced as approaching to the Lifshitz transitions, the contribution of the partial DOS is very small compared to that of the lower band. Therefore, the total DOS $\rho(0)$ is not drastically enhanced by these Lifshitz transitions, and hence the ferroelectric superconducting state is hardly stabilized at zero magnetic field in relatively high carrier density two- or three-band regimes. The phase diagram of the FESC depends on what band causes the Lifshitz transition.

2.5   Magnetic field-temperature phase diagram
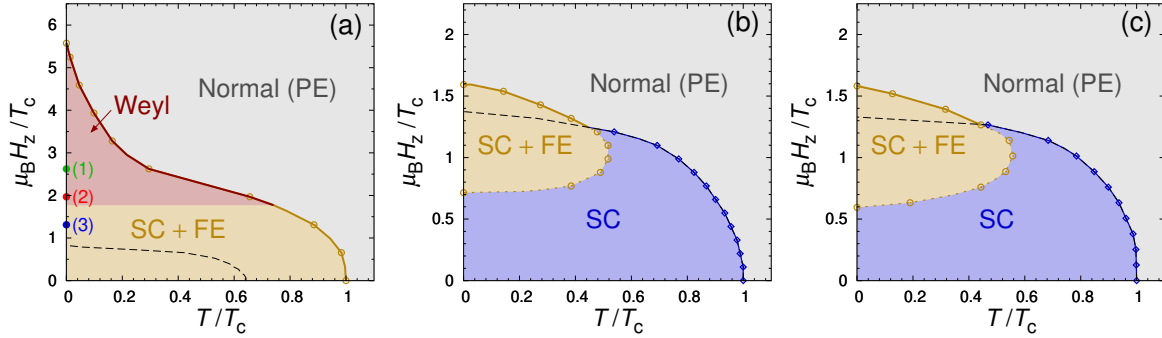
Fig. 2.8. Phase diagrams in a (a) single-band regime ($n = 5.0 \times 10^{-5}$), (b) two-band regime ($n = 3.2 \times 10^{-3}$), and (c) three-band regime ($n = 1.8 \times 10^{-2}$). Band structures corresponding to these carrier densities are shown in Fig. 2.9. The yellow or red solid (dotted) line shows the first-order (second-order) ferroelectric phase transition line. The black dashed line indicates the paraelectric superconducting transition line obtained by assuming $\gamma = 0$. The red colored region in (a) illustrates the Weyl superconducting phase. The pairing interaction and the lattice parameters are set to (a) $(V_s/t_1, \kappa_2, \kappa_4, \kappa_6) = (0.28, 6.75 \times 10^{-5}, 0, 0.50)$ (b) $(V_s/t_1, \kappa_2, \kappa_4, \kappa_6) = (0.51, 1.00 \times 10^{-2}, 0, 0)$ and (c) $(V_s/t_1, \kappa_2, \kappa_4, \kappa_6) = (0.77, 5.30 \times 10^{-2}, 0, 0)$ respectively. The temperature T and the magnetic field $\mu_B H_z$ are normalized by the superconducting transition temperature T_c at zero magnetic field.

Figure 2.8 shows the magnetic field versus temperature phase diagrams in three different carrier density regimes which are distinguished by the number of Fermi surfaces [see Fig. 2.9(a)]. In the single-band regime, the ferroelectric superconducting state is stabilized at zero magnetic field [Fig. 2.8(a)]. This is a consequence of a Lifshitz transition induced by the ferroelectricity as shown in Sec. 2.4.3. On the other hand, the zero field FESC is not realized in the two- or three-band regime due to the small contribution of the middle or upper band to the total DOS. Because of the multiband nature of STO, the zero field FESC is possible only in the dilute region where the Lifhisitz transition of the lower band can be induced by the ferroelectricity.

Irrespective of the carrier density, the ferroelectric superconducting state is stabilized under the magnetic field, despite an absence of the zero field ferroelectric superconducting phase in the two- or three-band regime [Figs. 2.8(b) and 2.8(c)]. This magnetic-field-induced FESC originates from the anomalous Pauli depairing effect in NCS superconductors [9, 10, 16, 111, 112]. To avoid the Pauli depairing effect, superconductivity induces the ferroelectric order giving rise to the Rashba SOC. Then, the upper critical field is enhanced compared to the paraelectric state.

In particular, the enhancement of the upper critical field is remarkable in the single-band regime [Fig. 2.8(a)]; $\mu_B H/T_c \sim 5.5$ far exceeds the Pauli limit ~ 1.25. This is owing to the Lifshitz transition and the multiorbital effect discussed in Sec. 2.4.2. For low carrier densities, the free energy is minimized at a large value of γ so that the Lifshitz transition of the lower
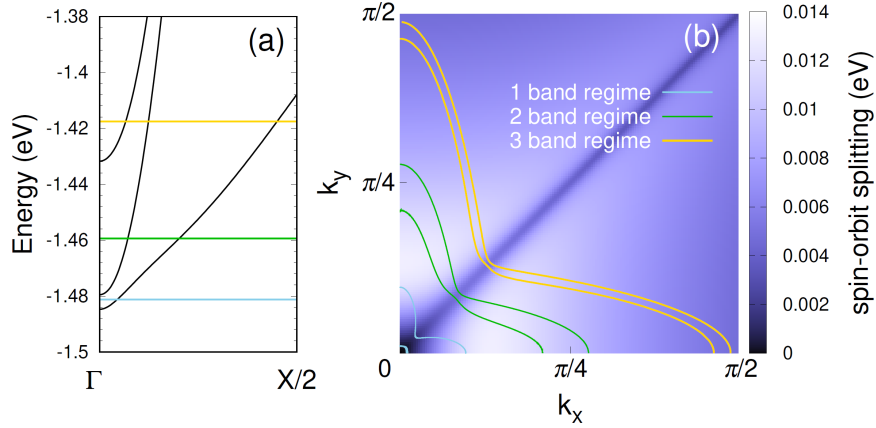
Fig. 2.9. (a) Band structure for $\gamma = 0$. The blue, green and yellow horizontal lines illustrate the Fermi energy in a single-band regime ($n = 5.0 \times 10^{-5}$), two-band regime ($n = 3.2 \times 10^{-3}$), and three-band regime ($n = 1.8 \times 10^{-2}$), respectively. (b) Illustration of the Rashba split Fermi surfaces of the lower band ($\gamma = 29.1$ meV) in the single-, two-, and three-band regime, overwritten on the magnitude of spin-orbit splitting. Color of Fermi surfaces corresponds to the colored lines in (a).

band occurs [Fig. 2.7(b)]. Consequently, the first-order ferroelectric transition occurs at the same time as the superconducting transition. Furthermore, the Rashba spin-orbit splitting of the lower band particularly becomes large around the Γ-point thanks to the multiorbital effect [see Figs. 2.4(c) and 2.9(b)]. Therefore, the Pauli depairing effect is strongly suppressed and the upper critical field is strongly enhanced as shown in Sec. 2.4.2. On the other hand, the γ and resulting spin-orbit splitting are small in a higher carrier density regime, and thus the upper critical field is not significantly enhanced [Figs. 2.8(b) and 2.8(c)].

2.5.1 Weyl superconductivity

As a consequence of the drastically enhanced upper critical field, the dilute superconducting state in STO may realize a topological Weyl superconductor. In a two-dimensional Rashba superconductor, a gapped topological superconducting state in class D can be realized under a perpendicular magnetic field [6, 7]. In our three dimensional case, a Weyl superconducting state, which is characterized by topologically-protected Weyl nodes, is realized in the ferroelectric phase for a wide range of the magnetic field along the polar axis. We identify Weyl nodes by calculating k_z-dependent Chern number,

$$\nu(k_z) = \frac{1}{2\pi} \int dk_x dk_y F_z(\boldsymbol{k}), \tag{2.31}$$
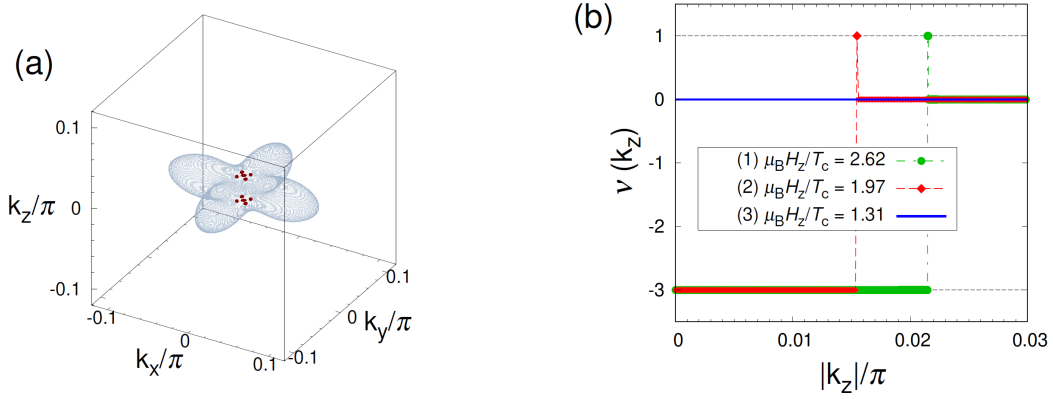
Fig. 2.10. (a) Weyl nodes (red points) on the Fermi surface. Parameters correspond to the point (1) in Fig. 2.8(a). (b) k_z-dependent Chern number calculated at three magnetic fields (1), (2), and (3) in Fig. 2.8(a). In the Weyl superconducting phase, $\nu(k_z)$ changes as $-3 \rightarrow 1 \rightarrow 0$.

on a two-dimensional k_x-k_y plane [114–116]. The Berry flux $F_a(\boldsymbol{k})$ is defined as

$$F_a(\boldsymbol{k}) = -i\epsilon_{abc} \sum_{E_m(\boldsymbol{k})<0} \partial_{k_b} \langle u_m(\boldsymbol{k})|\partial_{k_c} u_m(\boldsymbol{k}) \rangle, \qquad (2.32)$$

where the wave function of a Bogoliubov quasiparticle with energy $E_m(\boldsymbol{k})$ is denoted as $|u_m(\boldsymbol{k})\rangle$. Since a jump in $\nu(k_z)$ is equivalent to the sum of Weyl charges at k_z, we can detect Weyl charges by counting point nodes and comparing it with the jump. As shown in Fig. 2.10(b), the Chern number jumps by $+1$ and -4. Thus, we identify five pairs of Weyl nodes and we illustrate the distribution of Weyl charges in the momentum space in Fig. 2.10(a). One of them is located at poles of the Fermi surface. The rest of Weyl nodes, which are protected by C_4 symmetry, surrounds the above Weyl nodes with opposite Weyl charges. These four pairs of Weyl nodes arise as a consequence of the anisotropic Fermi surfaces due to the multiorbital effect. Therefore, a Weyl superconducting state with Chern number $\nu(k_z) = (+1) \times 1 + (-1) \times 4 = -3$ is obtained. Thus, multiorbital nature of STO leads to topological property distinct from the single-orbital topological Rashba superconductor with Chern number $\nu = \pm 1$ [6, 7]. It gives rise to three Majorana arcs in the surface state, and the zero-field thermal conductivity $\kappa'_{xy} \sim T \int dk_z \nu(k_z)$ [117] in STO should be larger than that in the single-orbital Rashba model.

2.6 Ferroelectricity-induced odd-frequency pairing

In the previous sections, we have investigated the mechanism to stabilize the ferroelectric superconducting phase by analyzing a multiorbital model for STO. In this section, we demonstrate that the combination of FESC and multiorbital/multiband nature leads to the generation of the odd-frequency pair correlations.

2.6.1 Berezinskii rule

We begin our discussion by classifying multiorbital superconducting states based on the fermionic symmetry, namely the *Berezinskii rule* [118, 119]. The pair amplitude (anomalous Green's function) can be defined in a multiorbital system as

$$\mathcal{F}_{ls,l's'}(\boldsymbol{k}, \tau) = -\langle T_\tau c_{\boldsymbol{k},ls}(\tau) c_{-\boldsymbol{k},l's'}(0)\rangle, \tag{2.33}$$

where τ is the imaginary time and $c_{\boldsymbol{k},ls}$ is the annihilation operator for an electron with momentum $\boldsymbol{k}$, orbital index l, and spin $s = \uparrow, \downarrow$. T_τ denotes the time-ordering operator for τ. The Matsubara representation of Eq. (2.33) is given by

$$\mathcal{F}_{ls,l's'}(\boldsymbol{k}, i\omega_m) = \int_0^\beta d\tau \mathcal{F}_{ls,l's'}(\boldsymbol{k}, \tau) e^{i\omega_m \tau}, \tag{2.34}$$

where $\omega_m = (2m+1)\pi\beta$ is a Matsubara frequency for the inverse temperature $\beta = 1/T$ and $m \in \mathbb{Z}$. We here consider the space, time, spin, and orbital parities of Cooper pairs in a multiorbital system. The space permutation operation $\mathcal{P}^*$ acting on the relative coordinate is defined as

$$\mathcal{P}^* \mathcal{F}_{ls,l's'}(\boldsymbol{k}, i\omega_m) \equiv \mathcal{F}_{ls,l's'}(-\boldsymbol{k}, i\omega_m). \tag{2.35}$$

Note that $\mathcal{P}^*$ is different from the full space inversion operation $\mathcal{P}$, since this operation merely permute the relative coordinate of two particles. The time permutation operation $\mathcal{T}^*$, which changes sign of the relative time τ, acts on the Matsubara anomalous Green's function as

$$\mathcal{T}^* \mathcal{F}_{ls,l's'}(\boldsymbol{k}, i\omega_m) \equiv \mathcal{F}_{ls,l's'}(\boldsymbol{k}, -i\omega_m). \tag{2.36}$$

Note that $\mathcal{T}^*$ is not the full time reversal operation $\mathcal{T}$, since this operation merely permute the relative time of the pairing correlator. The fact that permuting $\tau \to -\tau$ is different from the time reversal can be seen from the fact that the true time reversal $\mathcal{T}$ converts $\mathcal{F}$ to $\mathcal{F}^*$. The spin permutation operation $\mathcal{S}$ and the orbital permutation operation O, simple swap operators permuting respective indices, are introduced as:

$$\mathcal{S} \mathcal{F}_{ls,l's'}(\boldsymbol{k}, i\omega_m) \equiv \mathcal{F}_{ls',l's}(\boldsymbol{k}, i\omega_m), \tag{2.37}$$

$$O \mathcal{F}_{ls,l's'}(\boldsymbol{k}, i\omega_m) \equiv \mathcal{F}_{l's,ls'}(\boldsymbol{k}, i\omega_m). \tag{2.38}$$

The Fermi-Dirac statistics gives the sign change of the anomalous Green's function under the combined action of the space, time, spin, and orbital permutation operations as

$$\mathcal{S}\mathcal{P}^* O \mathcal{T}^* \mathcal{F}_{ls,l's'}(\boldsymbol{k}, i\omega_m) = -\mathcal{F}_{ls,l's'}(\boldsymbol{k}, i\omega_m), \tag{2.39}$$

Table 2.2. Symmetry properties of the anomalous Green's function under the space, time, spin, and orbital permutation operations.

Pairing	$\mathcal{S}$	$\mathcal{P}^*$	$\mathcal{O}$	$\mathcal{T}^*$	$\mathcal{SP}^*\mathcal{OT}^*$
$-+++$	-1	$+1$	$+1$	$+1$	-1
$---+$	-1	-1	-1	$+1$	-1
$++-+$	$+1$	$+1$	-1	$+1$	-1
$+-++$	$+1$	-1	$+1$	$+1$	-1
$-+--$	-1	$+1$	-1	-1	-1
$--+-$	-1	-1	$+1$	-1	-1
$+++-$	$+1$	$+1$	$+1$	-1	-1
$+---$	$+1$	-1	-1	-1	-1

which we write symbolically as $\mathcal{SP}^*\mathcal{OT}^* = -1$. The full symmetries of the Cooper pair that satisfies Eq. (2.39) are summarized in Table 2.2.

Then, we perform the classification of the pair amplitude based on the results in Table 2.2. First of all, the anomalous Green's function can be decomposed as

$$\mathcal{F}_{ls,l's'}(k) = \left[\left(\psi_{ll'}(k)\sigma^0 + \boldsymbol{d}_{ll'}(k)\cdot\boldsymbol{\sigma}\right)i\sigma^y\right]_{ss'}, \tag{2.40}$$

where σ^0 is a 2×2 identity matrix and $\boldsymbol{\sigma} = (\sigma^x, \sigma^y, \sigma^z)$ are the Pauli matrices. We here used the abbreviate notation $k = (\boldsymbol{k}, i\omega_m)$. The spin-singlet (triplet) pair amplitude $\psi_{ll'}(k)$ ($\boldsymbol{d}_{ll'}(k)$) is odd (even) under the spin permutation $\mathcal{S}$. Furthermore, we define the orbital-singlet and orbital-triplet pair amplitudes as

$$\psi_{ll'}^{\pm}(k) = \frac{\psi_{ll'}(k) \pm \psi_{l'l}(k)}{2}, \tag{2.41}$$

$$\boldsymbol{d}_{ll'}^{\pm}(k) = \frac{\boldsymbol{d}_{ll'}(k) \pm \boldsymbol{d}_{l'l}(k)}{2}. \tag{2.42}$$

The orbital-triplet pair amplitudes $\psi_{ll'}^{+}(k)$ and $\boldsymbol{d}_{ll'}^{+}(k)$ are even under the orbital permutation $\mathcal{O}$. On the other hand, the orbital-singlet pair amplitudes $\psi_{ll'}^{-}(k)$ and $\boldsymbol{d}_{ll'}^{-}(k)$ are odd under the orbital permutation $\mathcal{O}$.

Using Eqs. (2.41) and (2.42), the odd-frequency pair amplitudes, that are odd under the

time permutation $\mathcal{T}^*$, can be obtained as follows:

$$\mathcal{F}_{ll'}^{-+--} = \frac{(\psi_{ll'}^- + \mathcal{P}^*\psi_{ll'}^-) - \mathcal{T}^*(\psi_{ll'}^- + \mathcal{P}^*\psi_{ll'}^-)}{4}, \tag{2.43}$$

$$\mathcal{F}_{ll'}^{--+-} = \frac{(\psi_{ll'}^+ - \mathcal{P}^*\psi_{ll'}^+) - \mathcal{T}^*(\psi_{ll'}^+ - \mathcal{P}^*\psi_{ll'}^+)}{4}, \tag{2.44}$$

$$\mathcal{F}_{ll'}^{+++-} = \frac{(\boldsymbol{d}_{ll'}^+ + \mathcal{P}^*\boldsymbol{d}_{ll'}^+) - \mathcal{T}^*(\boldsymbol{d}_{ll'}^+ + \mathcal{P}^*\boldsymbol{d}_{ll'}^+)}{4}, \tag{2.45}$$

$$\mathcal{F}_{ll'}^{+---} = \frac{(\boldsymbol{d}_{ll'}^- - \mathcal{P}^*\boldsymbol{d}_{ll'}^-) - \mathcal{T}^*(\boldsymbol{d}_{ll'}^- - \mathcal{P}^*\boldsymbol{d}_{ll'}^-)}{4}, \tag{2.46}$$

where we suppressed the k-dependence for brevity. In the same manner, the even-frequency pair amplitudes can be obtained as

$$\mathcal{F}_{ll'}^{-+++} = \frac{(\psi_{ll'}^+ + \mathcal{P}^*\psi_{ll'}^+) + \mathcal{T}^*(\psi_{ll'}^+ + \mathcal{P}^*\psi_{ll'}^+)}{4}, \tag{2.47}$$

$$\mathcal{F}_{ll'}^{---+} = \frac{(\psi_{ll'}^- - \mathcal{P}^*\psi_{ll'}^-) + \mathcal{T}^*(\psi_{ll'}^- - \mathcal{P}^*\psi_{ll'}^-)}{4}, \tag{2.48}$$

$$\mathcal{F}_{ll'}^{++-+} = \frac{(\boldsymbol{d}_{ll'}^- + \mathcal{P}^*\boldsymbol{d}_{ll'}^-) + \mathcal{T}^*(\boldsymbol{d}_{ll'}^- + \mathcal{P}^*\boldsymbol{d}_{ll'}^-)}{4}, \tag{2.49}$$

$$\mathcal{F}_{ll'}^{+-++} = \frac{(\boldsymbol{d}_{ll'}^+ - \mathcal{P}^*\boldsymbol{d}_{ll'}^+) + \mathcal{T}^*(\boldsymbol{d}_{ll'}^+ - \mathcal{P}^*\boldsymbol{d}_{ll'}^+)}{4}. \tag{2.50}$$

The spin-triplet pair amplitudes are described by using a vector notation $\mathcal{F}_{ll'} = \mathcal{F}_{ll',x}\hat{\boldsymbol{x}} + \mathcal{F}_{ll',y}\hat{\boldsymbol{y}} + \mathcal{F}_{ll',z}\hat{\boldsymbol{z}}$, where $\sigma^\mu i\sigma^y$ is represented as $\hat{\boldsymbol{\mu}}$. The above odd/even-frequency pair amplitudes satisfy the Berezinskii rule (i.e., $\mathcal{SP}^*\mathcal{OT}^* = -1$).

2.6.2 Symmetry analysis of odd-frequency pair amplitude in SrTiO$_3$

Now, we perform the classification of the multiorbital odd-frequency pair amplitude based on both fermionic and space group symmetries (see Appendix B for the classification method of the pair amplitude based on the space group symmetry). As far as we know, we here provide a first example of group theoretical classification for the multiorbital odd-frequency superconductivity, although that for the multiorbital even-frequency superconductivity [120, 121] and single-orbital odd-frequency superconductivity [122] has been done in previous works.

With STO in mind, we here consider a time-reversal symmetric t_{2g} electron system in tetragonal D_{4h} or C_{4v} point group and assume s-wave superconducting states which belong to trivial irreducible representation (IR) (i.e., $\mathcal{D}^\Gamma(g) = 1$ in Eq. (B.7)). Then, according to Eq. (B.7), it is sufficient to classify the pair amplitudes based on the point group symmetry, not space group symmetry. Extension to anisotropic superconducting states that transform in accordance with nontrivial IRs is straightforward. The basis functions for k-dependence of the odd/even-frequency pair amplitudes, that are determined by using Eq. (B.7), are listed in

Table 2.3. Basis functions for $\boldsymbol{k}$-dependence of (a) odd-frequency pair amplitudes and (b) even-frequency pair amplitudes in a t_{2g} electron system under D_{4h} point group symmetry. Basis functions of A_{1g} and A_{2u} IRs are listed, because the superconducting gap function is assumed to belong the trivial IR of D_{4h} or C_{4v}.

(a) Odd-frequency

	Basis functions	IR
$\mathcal{F}_{ll'}^{-+--}$	$k_z(k_y\zeta_x^- + k_x\zeta_y^-),\ k_xk_y(k_x^2 - k_y^2)\zeta_z^-$	A_{1g}
$\mathcal{F}_{ll'}^{--+-}$	$k_z(\zeta_x^0 + \zeta_y^0),\ k_z\zeta_z^0,\ k_y\zeta_x^+ + k_x\zeta_y^+,\ k_xk_yk_z\zeta_z^+$	A_{2u}
$\mathcal{F}_{ll'}^{+++-}$	$k_z(k_y\zeta_x^0\hat{\boldsymbol{x}} - k_x\zeta_y^0\hat{\boldsymbol{y}}),\ k_z(k_y\zeta_y^0\hat{\boldsymbol{x}} - k_x\zeta_x^0\hat{\boldsymbol{y}}),\ k_xk_y(\zeta_x^0 - \zeta_y^0)\hat{\boldsymbol{z}}$ $k_z(k_y\zeta_z^0\hat{\boldsymbol{x}} - k_x\zeta_z^0\hat{\boldsymbol{y}}),\ k_xk_y(k_x^2 - k_y^2)\zeta_z^0\hat{\boldsymbol{z}}$ $k_xk_y(\zeta_y^+\hat{\boldsymbol{x}} - \zeta_x^+\hat{\boldsymbol{y}}),\ k_z(k_y\zeta_y^+ - k_x\zeta_x^+)\hat{\boldsymbol{z}},\ \zeta_x^+\hat{\boldsymbol{x}} - \zeta_y^+\hat{\boldsymbol{y}}$ $k_y^2\zeta_x^+\hat{\boldsymbol{x}} - k_x^2\zeta_y^+\hat{\boldsymbol{y}},\ k_x^2\zeta_x^+\hat{\boldsymbol{x}} - k_y^2\zeta_y^+\hat{\boldsymbol{y}},\ k_z^2(\zeta_x^+\hat{\boldsymbol{x}} - \zeta_y^+\hat{\boldsymbol{y}})$ $k_z(k_x\zeta_z^+\hat{\boldsymbol{x}} - k_y\zeta_z^+\hat{\boldsymbol{y}}),\ (k_x^2 - k_y^2)\zeta_z^+\hat{\boldsymbol{z}}$	A_{1g}
$\mathcal{F}_{ll'}^{+---}$	$k_xk_yk_z(\zeta_y^-\hat{\boldsymbol{x}} - \zeta_x^-\hat{\boldsymbol{y}}),\ k_z(\zeta_x^-\hat{\boldsymbol{x}} - \zeta_y^-\hat{\boldsymbol{y}}),\ (k_y\zeta_y^- - k_x\zeta_x^-)\hat{\boldsymbol{z}}$ $k_x\zeta_z^-\hat{\boldsymbol{x}} + k_y\zeta_z^-\hat{\boldsymbol{y}},\ k_z\zeta_z^-\hat{\boldsymbol{z}}$	A_{2u}

(b) Even-frequency

	Basis functions	IR
$\mathcal{F}_{ll'}^{-+++}$	$\zeta_x^0 + \zeta_y^0,\ k_x^2\zeta_x^0 + k_y^2\zeta_y^0,\ k_y^2\zeta_x^0 + k_x^2\zeta_y^0,\ k_z^2(\zeta_x^0 + \zeta_y^0)$ $\zeta_z^0,\ (k_x^2 + k_y^2)\zeta_z^0,\ k_z^2\zeta_z^0,\ k_z(k_y\zeta_x^+ + k_x\zeta_y^+),\ k_xk_y\zeta_z^+$	A_{1g}
$\mathcal{F}_{ll'}^{---+}$	$k_y\zeta_x^- - k_x\zeta_y^-,\ k_xk_yk_z(k_x^2 - k_y^2)\zeta_z^-$	A_{2u}
$\mathcal{F}_{ll'}^{++-+}$	$\zeta_x^-\hat{\boldsymbol{x}} + \zeta_y^-\hat{\boldsymbol{y}},\ k_x^2\zeta_x^-\hat{\boldsymbol{x}} + k_y^2\zeta_y^-\hat{\boldsymbol{y}},\ k_y^2\zeta_x^-\hat{\boldsymbol{x}} + k_x^2\zeta_y^-\hat{\boldsymbol{y}},\ k_z^2(\zeta_x^-\hat{\boldsymbol{x}} + \zeta_y^-\hat{\boldsymbol{y}})$ $k_xk_y(\zeta_y^-\hat{\boldsymbol{x}} + \zeta_x^-\hat{\boldsymbol{y}}),\ k_z(k_x\zeta_x^- + k_y\zeta_y^-)\hat{\boldsymbol{z}}$ $k_z(k_x\zeta_z^-\hat{\boldsymbol{x}} + k_y\zeta_z^-\hat{\boldsymbol{y}}),\ \zeta_z^-\hat{\boldsymbol{z}},\ (k_x^2 + k_y^2)\zeta_z^-\hat{\boldsymbol{z}},\ k_z^2\zeta_z^-\hat{\boldsymbol{z}}$	A_{1g}
$\mathcal{F}_{ll'}^{+-++}$	$k_y\zeta_x^0\hat{\boldsymbol{x}} - k_x\zeta_y^0\hat{\boldsymbol{y}},\ k_y\zeta_y^0\hat{\boldsymbol{x}} - k_x\zeta_x^0\hat{\boldsymbol{y}},\ k_xk_yk_z(\zeta_x^0 - \zeta_y^0)\hat{\boldsymbol{z}}$ $k_y\zeta_z^0\hat{\boldsymbol{x}} - k_x\zeta_z^0\hat{\boldsymbol{y}},\ k_xk_yk_z(k_x^2 - k_y^2)\zeta_z^0\hat{\boldsymbol{z}}$ $k_xk_yk_z(\zeta_y^+\hat{\boldsymbol{x}} - \zeta_x^+\hat{\boldsymbol{y}}),\ k_z(\zeta_x^+\hat{\boldsymbol{x}} - \zeta_y^+\hat{\boldsymbol{y}}),\ (k_x\zeta_x^+ - k_y\zeta_y^+)\hat{\boldsymbol{z}}$ $k_x\zeta_z^+\hat{\boldsymbol{x}} - k_y\zeta_z^+\hat{\boldsymbol{y}},\ k_z(k_x^2 - k_y^2)\zeta_z^+\hat{\boldsymbol{z}}$	A_{2u}

Tables 2.3. In the table, the symmetry of the basis functions in the orbital space is described by using the following matrices:

$$\zeta_x^0 = |1\rangle \langle 1|, \quad \zeta_y^0 = |2\rangle \langle 2|, \quad \zeta_z^0 = |3\rangle \langle 3|, \tag{2.51}$$

$$\zeta_x^\pm = |3\rangle \langle 2| \pm |2\rangle \langle 3|, \quad \zeta_y^\pm = |1\rangle \langle 3| \pm |3\rangle \langle 1|, \quad \zeta_z^\pm = |2\rangle \langle 1| \pm |1\rangle \langle 2|, \tag{2.52}$$

where $|1\rangle \equiv |d_{yz}\rangle$, $|2\rangle \equiv |d_{xz}\rangle$, and $|3\rangle \equiv |d_{xy}\rangle$. When the anomalous Green's function $\mathcal{F}_{ls,l's'}(k)$ belongs to the trivial IR of D_{4h} point group, that is A_{1g} IR, only the even-parity ($\mathcal{P}^* = +1$) pair amplitudes $\mathcal{F}^{-+--}$ and $\mathcal{F}^{+++-}$ in Table 2.3 (a) are allowed. Then, the odd-parity ($\mathcal{P}^* = -1$) pair amplitudes should vanish because they do not belong to A_{1g} IR due to the sign change under space inversion operation $\mathcal{P} = \mathcal{P}^{*}$[5]. On the other hand, the odd-parity pair amplitudes can be trivial under all symmetry operations in C_{4v} point group, since D_{4h} point group can be decomposed as $D_{4h} = \{I, \mathcal{P}\} \otimes C_{4v}$, where I denotes the identity operation. Therefore, the odd-parity pair amplitudes $\mathcal{F}^{--+-}$ and $\mathcal{F}^{+---}$ belonging to A_{2u} IR in D_{4h} point group are listed in Table 2.3 (a), because A_{2u} is reduced to the trivial A_1 IR in C_{4v} point group. Note that the same holds for the even-frequency pair amplitudes shwon in Table 2.3 (b).

The odd-parity A_{2u} pair amplitudes are symmetrically forbidden in centrosymmetric D_{4h} point group, when the superconductivity belongs to the trivial IR as expected in STO. In order to induce the odd-parity A_{2u} pair amplitudes, a space inversion symmetry breaking, which descends the crystallographic point group from D_{4h} to C_{4v}, is necessary. This symmetry lowering from D_{4h} to C_{4v} can be realized by a ferroelectric phase transition (spontaneous polar inversion symmetry breaking) that actually occurs in STO [76–79].

2.6.3   Odd-frequency pair amplitudes in SrTiO$_3$

Now that we have obtained the classification table of the odd-frequency pair amplitudes in STO, we here perform numerical calculations and compare the results with the classification table. To study the interplay of odd-frequency pairing and ferroelectricity, we consider a dilute carrier density regime of STO in which only the doubly-degenerated lowest energy band intersect the Fermi level at $\gamma = 0$. As shown in the previous sections, in such a dilute density regime, the ferroelectric superconducting phase is stabilized without external magnetic field [see Fig. 2.8 (a)] owing to the Lifshitz transition associated to the ferroelectricity-induced Rashba splitting of the band structure.

The parameters are set to be $n = 5.0 \times 10^{-5}$, $V_s/t_1 = 0.28$, and $(\kappa_4, \kappa_6) = (0, 0.5)$ in the same way as the numerical calculations of the single-band regime in Sec. 2.5. Then, the ferroelectric superconducting phase is stabilized at zero magnetic field when the lattice parameter κ_2 is set to be smaller than a critical value. The value of κ_2 and obtained results of the superconducting

---

[5]Note that the action of the space permutation $\mathcal{P}^*$ for the *s*-wave superconducting state in t_{2g} electron system is equivalent to that of the full space inversion $\mathcal{P}$.

Table 2.4. Model parameters for the numerical calculations. The superconducting order parameter Δ_l and odd-parity hoping integral γ are determined by minimizing the free energy at $T/t_1 = 1.0 \times 10^{-10}$.

	paraelectric phase	ferroelectric phase
κ_2	8.00×10^{-5}	6.75×10^{-5}
γ	0	0.105
$\Delta_{1,2}$	0.00160	0.00277
Δ_3	0.000268	0.00138

order parameters and γ are summarized in Table 2.4.

On the basis of numerical solution of the electron-lattice coupled three-orbital model in Sec. 2.3, we elucidate odd-frequency pair amplitudes in bulk STO. Using the BdG Hamiltonian matrix in Eqs. (2.20) and (2.21), we obtain the full Matsubara Green's function matrix as

$$\mathcal{G}(\boldsymbol{k}, i\omega_m) = [i\omega_m \mathbb{1}_{12} - H(\boldsymbol{k})]^{-1}, \tag{2.53}$$

where $\mathbb{1}_{12}$ is a 12×12 identity matrix. The matrix structure of $\mathcal{G}(k)$ is described as

$$\mathcal{G}(k) = \begin{pmatrix} \mathcal{G}^0(k) & \mathcal{F}(k) \\ \bar{\mathcal{F}}(k) & \bar{\mathcal{G}}^0(k) \end{pmatrix}. \tag{2.54}$$

The 6×6 submatrix $\mathcal{G}^0(k)$ and $\mathcal{F}(k)$ are the normal and anomalous Green's functions, respectively. $\bar{\mathcal{G}}^0(k)$ ($\bar{\mathcal{F}}(k)$) is the particle-hole counterpart of $\mathcal{G}^0(k)$ ($\mathcal{F}(k)$). By applying Eqs. (2.43)-(2.46) to the matrix elements of $\mathcal{F}(k)$, we calculate the odd-frequency pair amplitudes in bulk STO.

In the following, we investigate the odd-frequency pair correlations in both paraelectric (nonpolar) and ferroelectric (polar) phases of bulk STO. Note that we do not address the property of the odd-frequency pairing on the border of the ferroelectric quantum critical point, where the dynamical fluctuation of the ferroelectric order might have a significant impact on the odd-frequency pair correlations. The physics of the odd-frequency superconductivity in the ferroelectric quantum critical regime is an interesting topic which is left for future studies.

Paraelectric/nonpolar phase

First, we consider the odd-frequency pairing in the paraelectric phase with D_{4h} point group symmetry. Since we assumed the s-wave (A_{1g}) pairing [Eq. (2.12)], the odd-frequency pair amplitudes should belong to A_{1g} IR in the paraelectric phase. Then, the even-parity A_{1g} odd-frequency pair amplitudes can be finite. The orbital hybridization due to the LS coupling [the second term of Eq. (2.4)] is essential for the odd-frequency Cooper pairs because
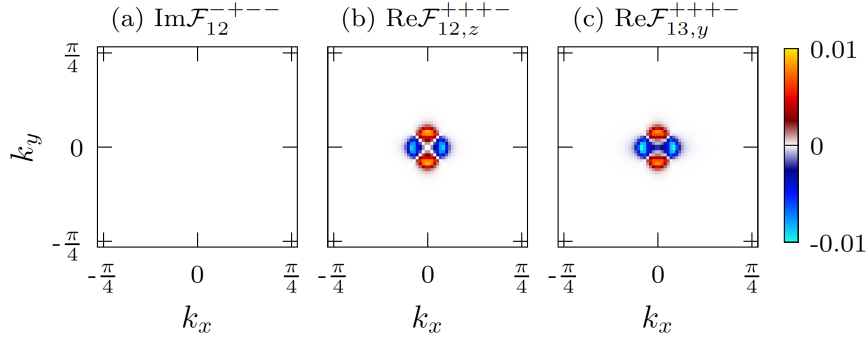
Fig. 2.11. $\boldsymbol{k}$-dependence of the even-parity odd-frequency pair amplitudes (a) $\text{Im}\mathcal{F}_{12}^{-+--}(k)$, (b) $\text{Re}\mathcal{F}_{12,z}^{+++-}(k)$, and (c) $\text{Re}\mathcal{F}_{13,y}^{+++-}(k)$ at $k_z = 0$ in the paraelectric phase. The Matsubara frequency ω_m is set to be 1 meV, and the values of the pair amplitudes are normalized by $\mathcal{F}_{\text{max}}^{\text{BCS}}(\omega_m) = 0.237808$ meV^{-1}.

they disappear in the absence of the LS coupling. The representative components of even-parity A_{1g} odd-frequency pair amplitudes at $k_z = 0$ are shown in Fig. 2.11. Because of the time-reversal symmetry, the spin-singlet (spin-triplet) even-parity orbital-singlet (orbital-triplet) odd-frequency pair amplitude $\mathcal{F}_{ll'}^{-+--}$ ($\mathcal{F}_{ll'}^{+++-}$) is pure imaginary (real). The pair amplitude is normalized by a maximum value of the BCS pair amplitude $\mathcal{F}_{\text{max}}^{\text{BCS}}(\omega_m)$ which is defined as

$$\mathcal{F}_{\text{max}}^{\text{BCS}}(\omega_m) \equiv \max_{\boldsymbol{k},l,l'} \left| \mathcal{F}_{ll'}^{-+++}(\boldsymbol{k}, i\omega_m) \right|, \qquad (2.55)$$

where $\mathcal{F}_{ll'}^{-+++}$ is given by Eq. (2.47). As shown in Fig. 2.11 (a), the spin-singlet even-parity orbital-singlet odd-frequency pair amplitude $\mathcal{F}_{ll'}^{-+--}$ is not generated in our model although it is symmetrically allowed. On the other hand, some components of the spin-triplet even-parity orbital-triplet odd-frequency pair amplitudes $\mathcal{F}_{ll'}^{+++-}$, that have d- or $s + d$-wave like $\boldsymbol{k}$-dependence, are generated although their value is small compared to the BCS pair amplitude [Figs. 2.11 (b) and 2.11 (c)]. These results can be understood on the basis of the group theoretical classification in Sec. 2.6.2. Since we assumed an intraorbital spin-singlet s-wave even-frequency superconducting order parameter (i.e., $\mathcal{SP^*OT^*} = -+++$), an orbital hybridization, which invert the orbital parity O from $O = +1$ to $O = -1$, is necessary to induce finite $\mathcal{F}_{ll'}^{-+--}$. In addition, Table 2.3 (a) shows that the $\boldsymbol{k}$-dependence of $\mathcal{F}_{ll'}^{-+--}$ is proportional to $k_\mu k_{\mu'}$ ($\mu = x, y, z$ and $\mu \neq \mu'$) near the Γ point. This means that the generation of $\mathcal{F}_{ll'}^{-+--}$ requires the existence of orbital hybridization terms proportional to $k_\mu k_{\mu'}$ in the model Hamiltonian. Indeed, the even-parity orbital hybridizations proportional to $\sin k_\mu \sin k_{\mu'}$ are allowed by symmetry, and they may generate odd-frequency pair amplitudes $\mathcal{F}_{ll'}^{-+--}$. However, we omitted such hybridizations since their amplitude is tiny in bulk STO [101–103]. Then, $\mathcal{F}_{ll'}^{-+--}$ is not induced in our model. On the other hand, a spin-dependent scattering, which invert the spin parity $\mathcal{S}$ from $\mathcal{S} = -1$ to $\mathcal{S} = +1$, is necessary to induce finite $\mathcal{F}_{ll'}^{+++-}$. Besides, Table 2.3 (a) shows that

$\boldsymbol{k}$-dependence of some components in $\mathcal{F}_{ll'}^{+++-}$ are given by a linear combination of k_μ^2, which can be induced by the single electron kinetic energy $\varepsilon_l(\boldsymbol{k})$ given by Eqs. (2.5)-(2.7) [e.g., $\mathcal{F}_{12,z}^{+++-} \sim k_x^2 - k_y^2 \sim \varepsilon_1(\boldsymbol{k}) - \varepsilon_2(\boldsymbol{k})$]. Thus, the generation of these components is guaranteed in bulk STO owing to the existence of LS coupling, which is a spin-dependent local orbital hybridization. We found finite $\mathcal{F}_{12,z}^{+++-}$, $\mathcal{F}_{13,y}^{+++-}$, and $\mathcal{F}_{23,x}^{+++-}$ in the paraelectric phase as expected. Intraorbital components $\mathcal{F}_{ll}^{+++-}$ vanish similarly to $\mathcal{F}_{ll}^{-+--}$.
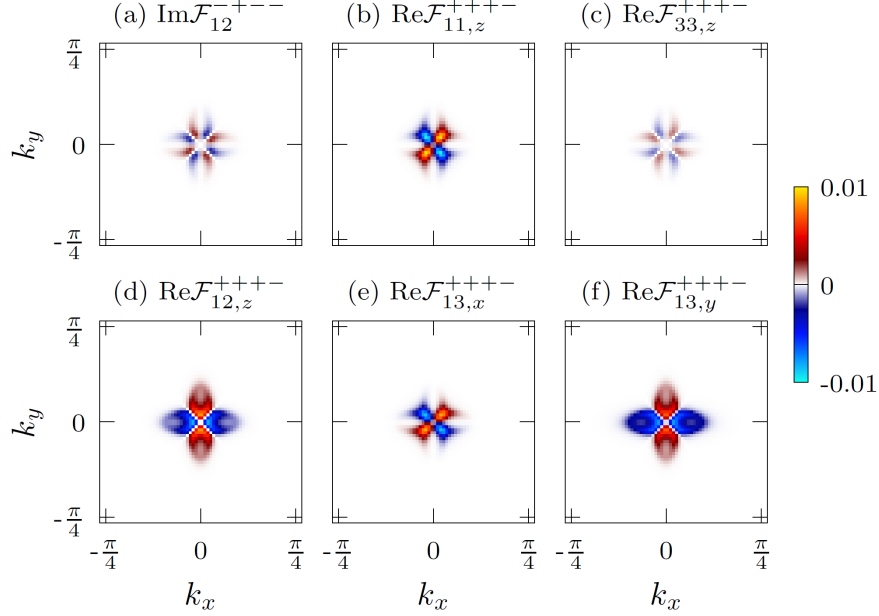
Ferroelectric/polar phase

| (a) Re$\mathcal{F}_{13}^{--+-}$ | (b) Im$\mathcal{F}_{13,z}^{+---}$ | (c) Im$\mathcal{F}_{12,x}^{+---}$ |
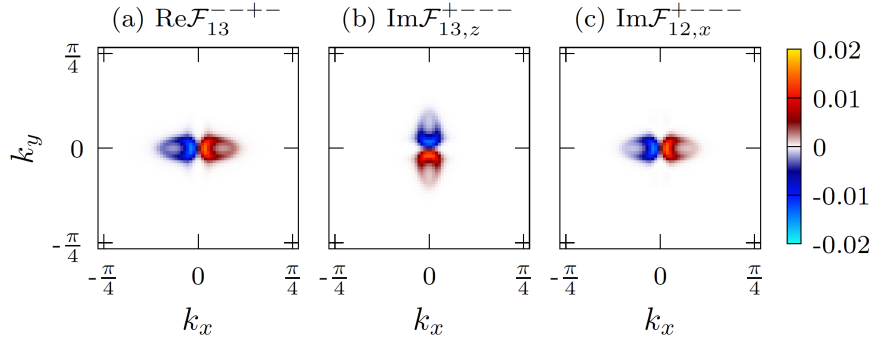
Fig. 2.12. $\boldsymbol{k}$-dependence of the odd-parity odd-frequency pair amplitudes (a) Re$\mathcal{F}_{13}^{--+-}(k)$, (b) Im$\mathcal{F}_{13,z}^{+---}(k)$, and (c) Im$\mathcal{F}_{12,x}^{+---}(k)$ at $k_z = 0$ in the ferroelectric phase. The Matsubara frequency ω_m is set to be 1 meV, and the values of the pair amplitudes are normalized by $\mathcal{F}_{\max}^{\mathrm{BCS}}(\omega_m) = 0.251432$ meV^{-1}.

Next, we investigate the odd-frequency pairing in the ferroelectric phase with C_{4v} point group symmetry. In the ferroelectric phase, the odd-parity odd-frequency pair amplitudes, that belong to A_{2u} IR, can also be induced owing to the breakdown of the space inversion symmetry. Figure 2.12 shows the $\boldsymbol{k}$-dependence of the representative components of odd-parity A_{2u} odd-frequency pair amplitudes. Owing to the time-reversal symmetry, the spin-singlet (spin-triplet) odd-parity orbital-triplet (orbital-singlet) odd-frequency pair amplitude $\mathcal{F}_{ll'}^{--+-}$ ($\mathcal{F}_{ll'}^{+---}$) is real (pure imaginary). They have p-wave like $\boldsymbol{k}$-dependence in consistent with the group theoretical classification in Table 2.3 (a). These *ferroelectricity-induced* odd-frequency pair amplitudes originate from the odd-parity interorbital hybridization $w_{x,y}(\boldsymbol{k}) \propto \sin k_{x,y}$ which appear in the ferroelectric phase [Eq. (2.11)], and hence they should have $p_{x,y}$-wave like $\boldsymbol{k}$-dependence (e.g., p_z-wave like pair amplitude $\mathcal{F}_{ll}^{--+-} \sim k_z$ is not driven by the ferroelectric order along the [001] axis, although it is allowed by symmetry). We confirmed that $\mathcal{F}_{13}^{--+-}$, $\mathcal{F}_{23}^{--+-}$, $\mathcal{F}_{13,z}^{+---}$, $\mathcal{F}_{23,z}^{+---}$, $\mathcal{F}_{12,x}^{+---}$, and $\mathcal{F}_{12,y}^{+---}$ are induced by the ferroelectric transition in bulk STO [Fig. 2.12] in accordance with the group theoretical classification as well as above discussions. Note that both the LS coupling and odd-parity orbital hybridization are responsible for finite $\mathcal{F}_{ll'}^{+---}$, since all of the spin, space, and orbital parities need to be inverted to induce this pair correlation. In addition, the odd-parity interorbital hybridization also generates some components of the

even-parity A_{1g} odd-frequency pair amplitudes, whose $\boldsymbol{k}$-dependences are proportional to $k_x^a k_y^b$ ($a, b = 0, 1, 2, \cdots$). For instance, $\mathcal{F}_{12}^{-+--} \sim k_x k_y (k_x^2 - k_y^2)$ takes a finite value in the ferroelectric phase [Fig. 2.13 (a)] although it is zero in the paraelectric phase [Fig. 2.11 (a)]. We found that $\mathcal{F}_{12}^{-+--}$, $\mathcal{F}_{11,z}^{+++-}$, $\mathcal{F}_{22,z}^{+++-}$, $\mathcal{F}_{33,z}^{+++-}$, $\mathcal{F}_{12,z}^{+++-}$, $\mathcal{F}_{13,x}^{+++-}$, $\mathcal{F}_{13,y}^{+++-}$, $\mathcal{F}_{23,x}^{+++-}$, and $\mathcal{F}_{23,y}^{+++-}$ are finite in the ferroelectric phase [Fig. 2.13].

Fig. 2.13. $\boldsymbol{k}$-dependence of the even-parity odd-frequency pair amplitudes (a) $\mathrm{Re}\mathcal{F}_{12}^{-+--}(k)$, (b) $\mathrm{Im}\mathcal{F}_{11,z}^{+++-}(k)$, (c) $\mathrm{Im}\mathcal{F}_{33,z}^{+++-}(k)$, (d) $\mathrm{Im}\mathcal{F}_{12,z}^{+++-}(k)$, (e) $\mathrm{Im}\mathcal{F}_{13,x}^{+++-}(k)$, (f) $\mathrm{Im}\mathcal{F}_{13,y}^{+++-}(k)$ at $k_z = 0$ in the ferroelectric phase. The Matsubara frequency ω_m is set to be 1 meV, and the values of the pair amplitudes are normalized by $\mathcal{F}_{\max}^{\mathrm{BCS}}(\omega_m) = 0.251432$ meV^{-1}.

2.7 Discussion and summary

In this chapter, we have studied an interplay of ferroelectric order and superconductivity in STO. In particular, we have proposed that the FESC is realized in STO near a ferroelectric transition point. The superconductivity triggers the coexisting ferroelectric order. A key ingredient is an effective electron-lattice coupling through the Rashba SOC in the ferroelectric phase.

By analyzing the realistic three-orbital model for STO, we showed that the zero field FESC is stabilized only in the dilute regime where the Lifshitz transition of the lower band can be induced by the ferroelectricity. This result is consistent with the experimental observation in $Sr_{1-x}Ca_xTiO_{3-\delta}$ [58], which indicates the ferroelectric superconducting phase only in a dilute carrier density regime. We also revealed that the ferroelectric superconducting state is stabilized under a magnetic field independent of the number of Fermi surfaces. This magnetic-field-induced phase appears because of the suppression of the Pauli depairing effect thanks to

the Rashba-type spin-momentum locking. Consequently, the upper critical field is enhanced by the ferroelectric transition. The upper critical field is particularly large in the dilute carrier density regime, because the multiorbital effect leads to a large spin-orbit splitting distinct from the conventional Rashba model. Furthermore, the high magnetic field region of dilute superconducting STO is identified as a Weyl superconducting state. This topological phase transition is realized as a result of the multiorbital effect and Lifshitz transition, in sharp contrast to the two-dimensional single-orbital model where the topological FESC is unstable [57].

In addition, we have studied the odd-frequency pair correlations in bulk STO near a ferro-electric critical point, based on the group theoretical classification and microscopic numerical calculations. First, by considering the fermionic and point group symmetries of a t_{2g} electron system, we have provided a classification table for the odd-frequency pair amplitudes. By combining with the symmetry of terms of the normal state Hamiltonian, the classification table enables us to predict which components of the odd-frequency pair correlations are generated. Then, we have calculated the odd-frequency pair amplitudes in a dilute carrier density regime of STO by using the three-orbital model. The obtained results are consistent with the group theoretical classification. In the paraelectric phase, the spin-triplet even-parity orbital-triplet odd-frequency pair correlations, that belong to A_{1g} IR of D_{4h} point group, are generated owing to the intrinsic LS coupling which leads to local spin-dependent orbital hybridization. In the ferroelectric phase, additional odd-parity odd-frequency pair correlations, that belong to A_{2u} IR of D_{4h} point group, are induced due to the odd-parity orbital mixing term proportional to the ferroelectric order parameter. This odd-parity orbital hybridization also leads to the generation of the spin-singlet even-parity orbital-singlet odd-frequency pair correlations. Since we assumed an intraorbital superconducting order parameter, the essential ingredient for the generation of the odd-frequency pair correlations is the orbital mixing in the normal state [119], which comes from the intrinsic LS coupling and polar inversion symmetry breaking.

The results of this chapter suggest a tunable crystal symmetry through superconductivity, in the presence of a coupling between spin, orbital, and lattice degrees of freedom. Most of the novel interplay of ferroelectric-like polar inversion symmetry breaking and superconductivity was uncovered in the dilute carrier density region. The dilute superconductivity in STO provides an ideal platform for the FESC. Furthermore, we have presented a first proposal of the multiorbital odd-frequency superconductivity in bulk STO. As far as we know, we have demonstrated a first example of group theoretical classification for the odd-frequency superconducting state in multiorbital systems. Our classification method is based on both fermionic symmetry of the anmalous Green's function (Berezinskii rule) and space group symmetry of the system, and may provide a useful tool for searching the odd-frequency pair correlations in multiorbital systems. Finally, it should be noticed that the results of this chapter are based on a simple BCS-type pairing interaction, which may not be appropriate for the dilute superconductivity in STO. Although we think that inclusion of dynamical electron-phonon

couplings and Coulomb interactions will not dramatically alter the results, such calculation is desired and left for a future study.

Chapter 3

Multiple odd-parity superconducting phases in bilayer transition metal dichalcogenides

3.1 Introduction

Searching for odd-parity superconductors, which provide a platform for the intrinsic topological superconductivity [123–125], has been one of central issues in research field of the unconventional superconductivity. At present, several solid-state materials are proposed as possible candidates for the odd-parity spin-triplet superconductor, e.g., Sr_2RuO_4 [126, 127], UPt_3 [128–130], UGe_2 [131], URhGe [132], UCoGe [133], and UTe_2 [134, 135]. Note that there are now some results conflicting with the spin-triplet pairing in Sr_2RuO_4 [136–139]. Exploration of spin-triplet superconductivity in systems other than heavy fermions is an important issue.

There are two important factors for realizing spin-triplet pairing states in solid-state materials, i.e., the FM spin fluctuation and the Fermi surface structure. In the absence of notable Fermi surface nesting, the FM fluctuation is enhanced when the Fermi energy lies near the van Hove singularity (vHS). Specifically, the so-called type-II vHS [140–142], whose saddle points are not located at the time-reversal invariant momenta, is preferable for the odd-parity superconductivity. On the other hand, a disconnected form of the Fermi surface is favorable for the odd-parity pairing since generation of gap nodes is avoidable [143, 144]. Stabilization of odd-parity spin-triplet pairing states has been theoretically proposed in a variety of systems with disconnected Fermi surfaces, e.g., $(TMTSF)_2X$ (X = PF_6,ClO_4) [143, 145–148], $Na_xCoO_2 \cdot yH_2O$ [149–157], SrPtAs [158, 159], and doped Kane-Mele model [160]. Note that some experimental results suggest that $Na_xCoO_2 \cdot yH_2O$ is a spin-singlet superconductor [161, 162].

Another intriguing topic for the unconventional superconductivity is relation between crystalline symmetry and the pairing states [163]. Particularly, various exotic superconducting

phenomena have been elucidated in locally NCS systems [31–38, 164, 165]. As explained in Sec. 1.1, a key microscopic aspect of locally NCS systems is the sublattice-dependent antisymmetric SOC, which leads to various exotic superconducting phenomena. Especially, it has been clarified that odd-parity topological superconductivity is realized by a combination of antiferromagnetic spin fluctuations and the sublattice-dependent antisymmetric SOC [38]. Thus, it is interesting to study interplay of FM-fluctuation-driven superconductivity and locally NCS crystal structure, in the sense of comparison with the case of the antiferromagnetic-fluctuation-driven superconductivity.

Considering the above-mentioned aspects, we provide a thorough microscopic investigation of unconventional superconductivity in a two-dimensional locally NCS triangular lattice [Fig. 3.1] with disconnected Fermi surfaces. The model is relevant to bilayer transition metal dichalcogenides (TMDs) with $2H_b$ stacking structure, which is favored in group-VI TMDs such as MX_2 (M = Mo, W and X = S, Se) [166, 167]. In a few layer group-VI TMDs, disconnected Fermi surfaces are formed around K and K′ points owing to the triangular lattice structure. Assuming a strong electron correlation, we clarify dominant FM-like spin fluctuations assisted by a type-II vHS. In fact, ferromagnetism has been recently observed in a few-layer VSe_2 [168] and $MnSe_2$ [169]. Since the conduction electrons in TMDs have d-orbital character, correlation effects are expected to have considerable impacts on the superconductivity [170–174]. We show that odd-parity superconducting state with f-wave symmetry is stabilized by the FM fluctuation in the absence of the SOC. On the other hand, the local inversion symmetry breaking in the crystal structure induces layer-dependent staggered Rashba and Zeeman SOC. The SOC breaks the spin SU(2) symmetry and lifts the degeneracy of spin-triplet superconducting states. Thus, the SOC controls the internal degree of freedom of odd-parity superconductivity and its topological property. We elucidate that multiple odd-parity superconducting phases with either p-wave or f-wave pairing, which belong to different IRs of the crystal point group, appear by increasing magnitude of the staggered SOC. It is shown that the multiple superconducting phase diagram is a consequence of the selection rule for locally NCS superconductors [31] and SOC-induced magnetic anisotropy. In addition, topological properties of the stable odd-parity superconducting states are studied. A chiral p-wave pairing state in a moderate Zeeman SOC region is identified as a topological superconducting state in class D.

The rest of this chapter is organized as follows. In Sec. 3.2, we introduce a two-dimensional bilayer triangular lattice Hubbard model including the layer-dependent staggered antisymmetric SOC. The formulation for the microscopic calculations based on the random phase approximation (RPA) and linearized Eliashberg equation is provided. In Sec. 3.3, we study the magnetic fluctuations. The dominance of the FM spin fluctuation and the magnetic anisotropy under the SOC are discussed. Numerical results of the Eliashberg equation are shown in Sec. 3.4. Topological properties of these superconducting states are also investigated. Finally, we present a summary of this chapter in Sec. 3.5.
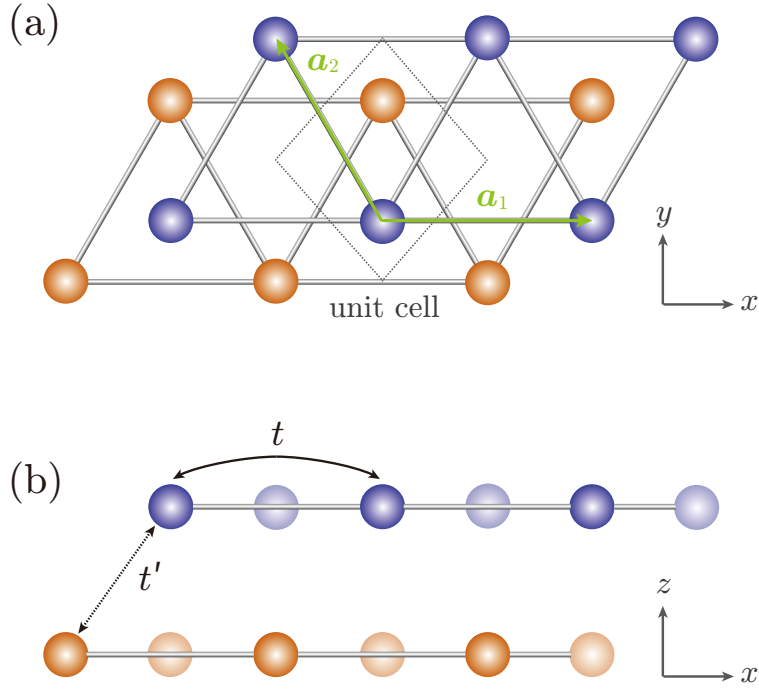
Fig. 3.1. Crystal structure of the bilayer triangular lattice. (a) is the top view and (b) is the side view. $\boldsymbol{a}_1$ and $\boldsymbol{a}_2$ are the lattice vectors. t and t' are the intralayer and interlayer hopping integrals, respectively.

3.2 Model and formulation

We consider a two-dimensional bilayer triangular lattice with the lattice vectors $\boldsymbol{a}_1 = (1, 0)$ and $\boldsymbol{a}_2 = (-1/2, \sqrt{3}/2)$ [Fig. 3.1], which is classified into D_{3d} point group. The crystal structure is equivalent to that of bilayer TMDs with $2H_b$ stacking. Recently, superconductivity in bilayer MoS_2 was realized by symmetric gating [175]. On this lattice, we introduce a single-orbital Hubbard model $\mathcal{H} = \mathcal{H}_0 + \mathcal{H}_{\text{int}}$. Note that we do not address the multiorbital physics in this study to perform material-independent general calculations and electron doped MoS_2 is indeed a single-orbital system. The single-particle Hamiltonian $\mathcal{H}_0$ with SOC is written as

$$\mathcal{H}_0 = \sum_{\boldsymbol{k},m,s} (\varepsilon(\boldsymbol{k}) - \mu) \, c^\dagger_{\boldsymbol{k},ms} c_{\boldsymbol{k},ms}$$
$$+ \sum_{\boldsymbol{k},s} \left(\eta(\boldsymbol{k}) c^\dagger_{\boldsymbol{k},as} c_{\boldsymbol{k},bs} + \text{H.c.} \right)$$
$$+ \sum_{\boldsymbol{k},\zeta,\zeta'} \sum_{j=1,2} \alpha_j \boldsymbol{g}_j(\boldsymbol{k}) \cdot \boldsymbol{\sigma}_{ss'} \tau^z_{mm'} c^\dagger_{\boldsymbol{k},ms} c_{\boldsymbol{k},ms'}, \qquad (3.1)$$

where $c_{\boldsymbol{k},ms}$ is the annihilation operator for an electron with momentum $\boldsymbol{k}$ and spin $s = \uparrow, \downarrow$ on layer $m = a, b$. $\zeta = (m, s)$ is the abbreviated notation, and σ^μ (τ^ν) is the Pauli matrix for spin (layer) degrees of freedom. The first term is the kinetic energy term. The single-electron kinetic

energy is described as

$$\varepsilon(\mathbf{k}) = 2t \left[\cos \mathbf{k} \cdot \mathbf{a}_1 + \cos \mathbf{k} \cdot \mathbf{a}_2 + \cos \mathbf{k} \cdot (\mathbf{a}_1 + \mathbf{a}_2) \right], \tag{3.2}$$

by taking into account the nearest-neighbor hopping. We choose the hopping integral t as a unit of energy ($t = 1$). The chemical potential μ is determined to fix the carrier density as n. The second term is the interlayer coupling. The interlayer hybridization function is given by

$$\eta(\mathbf{k}) = t' \left[1 + e^{-i\mathbf{k}\cdot\mathbf{a}_2} + e^{-i\mathbf{k}\cdot(\mathbf{a}_1+\mathbf{a}_2)} \right]. \tag{3.3}$$

In this study, we assume that the interlayer hopping integral t' is smaller than the intralayer hopping integral t (i.e., $t' < t$). The third term is the layer-dependent staggered SOC, which is originated from the locally NCS crystal structure and a spin-dependent intralayer hopping. Since the local site symmetry is C_{3v}, the g-vector $\mathbf{g}_j(\mathbf{k})$ should belong to A_{2u} IR of D_{3d} which becomes trivial A_1 IR in C_{3v} [see Table 3.1]. In this study, we consider two kinds of g-vectors as

$$\mathbf{g}_1(\mathbf{k}) = \frac{1}{\Lambda} \left[\frac{\sqrt{3}}{2} \left\{ \sin \mathbf{k} \cdot (\mathbf{a}_1 + \mathbf{a}_2) + \sin \mathbf{k} \cdot \mathbf{a}_2 \right\} \hat{\mathbf{x}} \right.$$
$$\left. - \left\{ \sin \mathbf{k} \cdot \mathbf{a}_1 + \frac{\sin \mathbf{k} \cdot (\mathbf{a}_1 + \mathbf{a}_2) - \sin \mathbf{k} \cdot \mathbf{a}_2}{2} \right\} \hat{\mathbf{y}} \right], \tag{3.4}$$

$$\mathbf{g}_2(\mathbf{k}) = \frac{2}{3\sqrt{3}} \left[\sin \mathbf{k} \cdot \mathbf{a}_1 + \sin \mathbf{k} \cdot \mathbf{a}_2 - \sin \mathbf{k} \cdot (\mathbf{a}_1 + \mathbf{a}_2) \right] \hat{\mathbf{z}}, \tag{3.5}$$

where $\Lambda = 1.7602$. Equations (3.4) and (3.5) are the Rashba and Zeeman SOC, respectively. Both terms belong to A_{2u} IR. The Rashba (Zeeman) SOC originates from the out-of-plane (in-plane) local inversion symmetry breaking at each layers. The constant factors are chosen as $\text{Max}_\mathbf{k} |\mathbf{g}_j(\mathbf{k})| = 1$. Although the Rashba SOC is negligible compared to the Zeeman SOC in some TMDs [11, 33], we treat both of them on equal footing to provide a general calculation not limited to existing TMDs. The on-site Coulomb interaction is given by

$$\mathcal{H}_{\text{int}} = U \sum_{\mathbf{i},m} n_{\mathbf{i},m\uparrow} n_{\mathbf{i},m\downarrow}, \tag{3.6}$$

where $n_{\mathbf{i},ms} = c_{\mathbf{i},ms}^\dagger c_{\mathbf{i},ms}$ is the electron density operator on site $\mathbf{i}$. Strong repulsive electron-electron interaction may be present owing to the d-orbital character of conduction carries in TMDs. We treat $\mathcal{H}_{\text{int}}$ in the RPA.

We study the superconducting instability in this model by solving the linearized Eliashberg
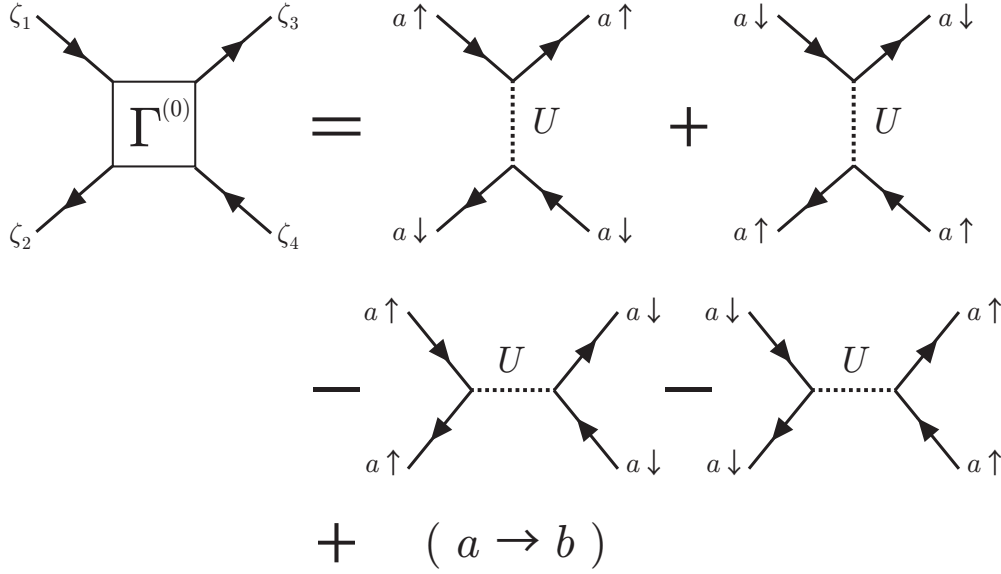
Fig. 3.2. Diagrammatic representation of the bare irreducible vertex Γ^0.

equation

$$\lambda \Delta_{\zeta\zeta'}(k) = -\frac{T}{N} \sum_{k'} \sum_{\{\zeta_j\}} V_{\zeta\zeta_1,\zeta_2\zeta'}(k-k') \mathcal{G}^0_{\zeta_3\zeta_1}(-k') \Delta_{\zeta_3\zeta_4}(k') \mathcal{G}^0_{\zeta_4\zeta_2}(k'),$$ (3.7)

where we used the abbreviated notation $k = (\boldsymbol{k}, i\omega_p)$ and $\omega_p = (2p+1)\pi T$ is the fermionic Matsubara frequency. The noninteracting temperature Green's function is given by $\mathcal{G}^0(k) = [i\omega_p \mathbb{1} - H_0(\boldsymbol{k})]^{-1}$. λ and $\Delta(k)$ are the eigenvalue and gap function, respectively. In the RPA, the effective pairing interaction $V(q)$ can be described as

$$V(q) = -\Gamma^0 \chi(q) \Gamma^0 - \Gamma^0,$$ (3.8)

by using the RPA susceptibility

$$\chi(q) = \chi^0(q)[\mathbb{1} - \Gamma^0 \chi^0(q)]^{-1}.$$ (3.9)

Here, the irreducible susceptibility is defined as

$$\chi^0_{\zeta_1\zeta_2,\zeta_3\zeta_4}(q) = -\frac{T}{N} \sum_k \mathcal{G}^0_{\zeta_3\zeta_1}(k) \mathcal{G}^0_{\zeta_2\zeta_4}(k+q).$$ (3.10)

The bare irreducible vertex in this model is obtained as

$$\Gamma^0_{\zeta_1\zeta_2,\zeta_3\zeta_4} = \frac{U}{2} \delta_{m_1 m_2} \delta_{m_3 m_4} \delta_{m_1 m_3} (\boldsymbol{\sigma}_{s_1 s_2} \cdot \boldsymbol{\sigma}_{s_4 s_3} - \delta_{s_1 s_2} \delta_{s_4 s_3}).$$ (3.11)

The diagrammatic representation of Eq. (3.11) is shown in Fig. 3.2. In the following numerical

calculations, we set $T/t = 0.02$, 64×64 $\boldsymbol{k}$-points, and 1024 Matsubara frequencies.

3.3 Magnetic fluctuation

In this section, we study the magnetic fluctuation by introducing magnetic susceptibilities as follows:

$$\chi_{mm'}^{\mu\nu}(q) = \sum_{\{s_j\}} \sigma_{s_1 s_2}^{\mu} \chi_{ms_1 ms_2, m's_3 m's_4}(q) \sigma_{s_4 s_3}^{\nu}, \tag{3.12}$$

where $\mu, \nu = x, y, z$. The magnetic fluctuation parallel (perpendicular) to the c-axis is charac-terized by $\chi^{\parallel} \equiv \chi^{zz}$ ($\chi^{\perp} \equiv (\chi^{xx} + \chi^{yy})/2$). In the following, we consider low doping regimes, in which small disconnected Fermi pockets are formed around the K and K' points [see Fig. 3.3(a)]. This condition is relevant to electron-doped bilayer TMDs with $2H_b$ stacking structure [175].
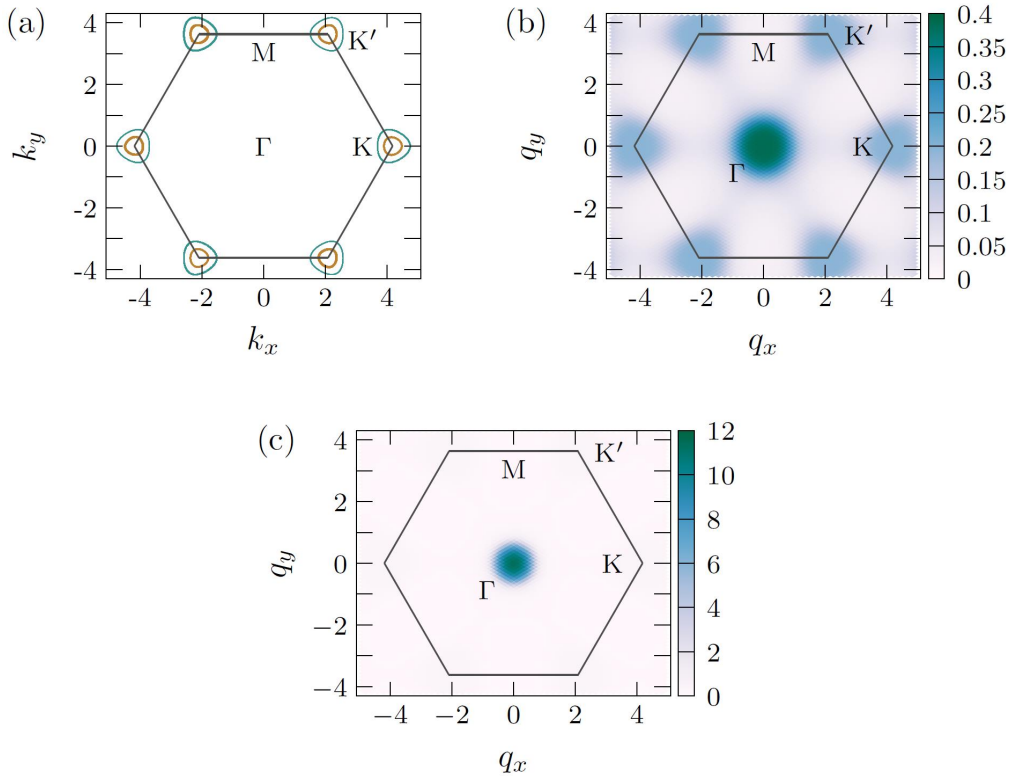
Fig. 3.3. (a) Fermi surfaces. (b) and (c) Momentum dependence of the intralayer magnetic susceptibility $\chi_{aa(=bb)}^{S}(\boldsymbol{q}, 0)$ for (b) $U = 0$ and (c) $U = 5.0$. We set $t'/t = 0.2$, $n = 0.1$, and $\alpha_j = 0$.

First, we investigate the magnetic fluctuations in the absence of the SOC. In this case, there is no magnetic anisotropy, and hence $\chi^{\parallel} = \chi^{\perp} (\equiv \chi^{S})$. In Figs. 3.3 (b) and 3.3 (c), we show momentum dependence of the intralayer magnetic susceptibility $\chi_{aa}^{S} (= \chi_{bb}^{S})$ for $t'/t = 0.2$,
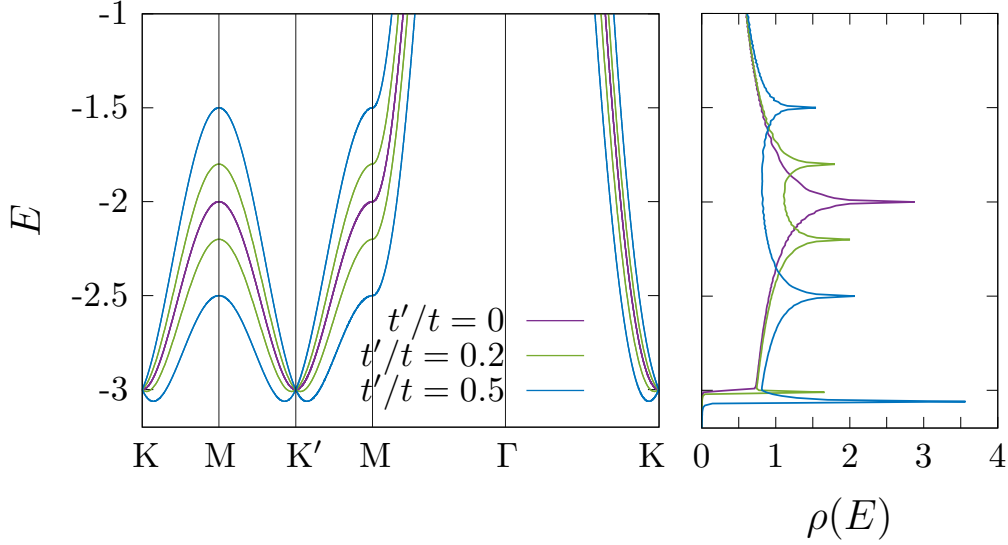
Fig. 3.4. Band structure and DOS for $\alpha_j = 0$ and $\mu = 0$.

$n = 0.1$ and $\alpha_j = 0$. In the absence of the Coulomb interaction, the magnetic susceptibility takes the maximum value at $\boldsymbol{q} = \boldsymbol{0}$ [see Fig. 3.3 (b)] which imply FM spin fluctuation in this system. By introducing the Coulomb interaction, the peak at $\boldsymbol{q} = \boldsymbol{0}$ becomes sharper [see Fig. 3.3 (c)], and the FM fluctuation is enhanced. The FM fluctuation is partially owing to the smallness of the Fermi surface. Besides, the FM fluctuation is enhanced because the Fermi level lies near the type-II vHS, which is associated to the saddle points located slightly away from the K (K′) point. This type-II vHS originates from the band splitting at the band bottom due to a finite interlayer coupling, and hence it is a fingerprint of the bilayer structure. In the 2H$_b$ stacking, the interlayer hybridization vanishes at the K (K′) points as ensured by the threefold rotational symmetry [167, 176, 177]. Therefore, Dirac-type linear dispersion appears around the K (K′) point [see Fig. 3.4], and it gives rise to the type-II vHS similar to the Rashba model [57]. Indeed, Fig. 3.4 reveals a large DOS near the band bottom.

Next, we show the magnetic fluctuations in the presence of the SOC. In locally NCS systems, a sublattice-dependent staggered SOC gives a significant impact on the electronic structure when the ratio of the SOC and the intersublattice coupling is large [165]. Since the interlayer coupling $\eta(\boldsymbol{k})$ vanishes at the K (K′) point [167, 176, 177], the ratio $\varphi_j(\boldsymbol{k}) \equiv |\alpha_j \boldsymbol{g}_j(\boldsymbol{k})|/|t'\eta(\boldsymbol{k})|$ can be large on the Fermi surface. Hence, the magnetic fluctuation is strongly affected by the staggered SOC. The SOC dependences of the magnetic susceptibilities are shown in Fig. 3.5. The sharp peak of the magnetic susceptibility at the Γ point is gradually suppressed by increasing α_j [Figs. 3.5 (a) and 3.5 (c)], and the FM fluctuation is weakened. The suppression of the FM fluctuation is significant in the case of the Zeeman SOC, since the ratio of the SOC and interlayer coupling has a larger value than that in the case of the Rashba SOC [i.e., $\varphi_2(\boldsymbol{k}_{\mathrm{F}}) > \varphi_1(\boldsymbol{k}_{\mathrm{F}})$]. Figures 3.5 (b) and 3.5 (d) reveal appearance of the magnetic anisotropy ($\chi^{\|} \neq \chi^{\perp}$) owing to the violation of the spin rotational symmetry. The Rashba SOC monotonically increases the
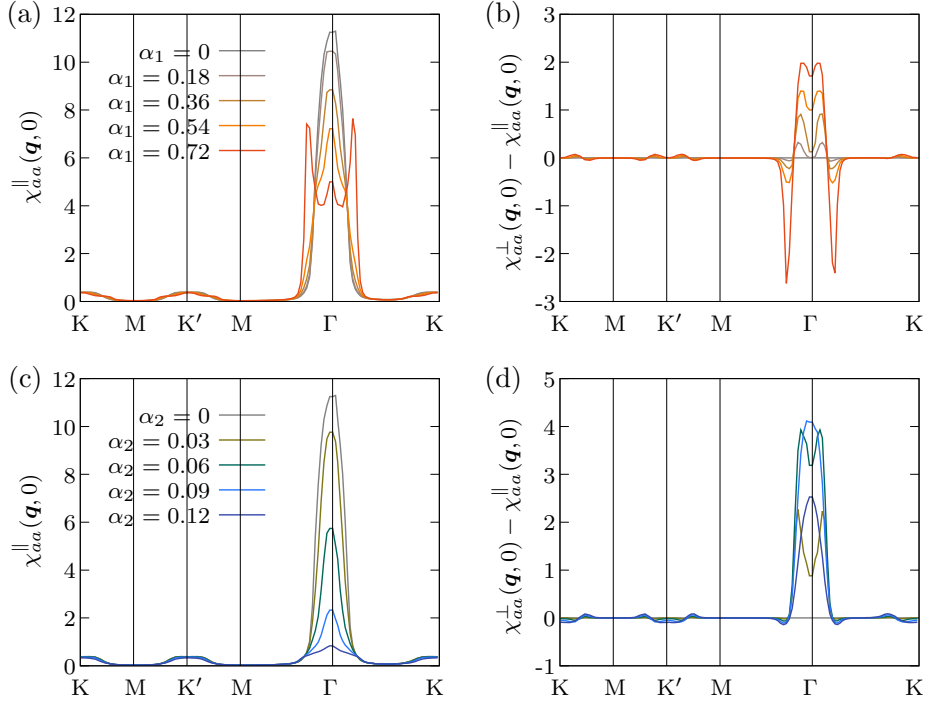
Fig. 3.5. Momentum dependence of the magnetic susceptibilities along the symmetry axis for several values of (a), (b) the Rashba SOC α_1 and (c), (d) Zeeman SOC α_2. Parameters are set to be $t'/t = 0.2$, $n = 0.1$, $U = 5.0$, and $T = 0.02$. (a), (c) An intralayer c-axis component $\chi_{aa}^{\parallel}(\boldsymbol{q}, 0)$, and (b), (d) the anisotropy $\chi_{aa}^{\perp}(\boldsymbol{q}, 0) - \chi_{aa}^{\parallel}(\boldsymbol{q}, 0)$.

magnetic anisotropy mainly at around the Γ point [Fig. 3.5 (b)]. On the other hand, the growth of the magnetic anisotropy by the Zeeman SOC is nonmonotonic [Fig. 3.5 (d)]. Although the SOC dependence of the magnetic anisotropy is complicated, we find that $\chi^{\perp} > \chi^{\parallel}$ is always realized at the Γ point. Thus, a FM-like magnetic structure with an in-plane spin-alignment is favored in the presence of the SOC. It should be noticed that such an in-plane FM ordering has been observed in atomically thin film of group-V TMD VSe$_2$ [168]. The superconductivity is significantly affected by this magnetic anisotropy as we demonstrate in Sec. 3.4.2.

3.4   Superconductivity

Here, we illustrate numerical results of the Eliashberg equation in the framework of the RPA. We specify the momentum- and layer-dependence of the gap functions from the numerical results of the eigenfunctions of the Eliashberg equation. The superconducting phase diagrams, which illustrate the most stable superconducting states with the largest eigenvalue, are obtained as a function of the Coulomb interaction, interlayer hopping, carrier density, and SOC. Then, multiple odd-parity superconducting phases stabilized by FM fluctuations are demonstrated.

### 3.4.1 Superconductivity without spin-orbit coupling
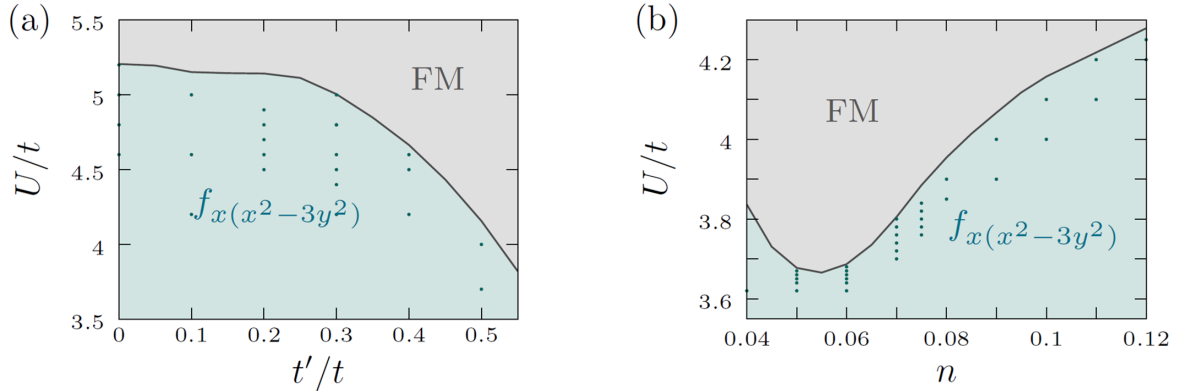
Fig. 3.6. (a) Phase diagram for the Coulomb interaction U and interlayer hopping t' at $n = 0.1$ and $T = 0.02$. (b) Phase diagram for the Coulomb interaction U and carrier density n at $t'/t = 0.5$ and $T = 0.02$. The solid line is the phase boundary between FM-like ordered state and paramagnetic state, at which the Stoner factor $S = \max[\hat{\Gamma}^{(0)} \hat{\chi}(q)]$ becomes unity. In the paramagnetic phase, the $f_{x(x^2-3y^2)}$-wave pairing state is stabilized.

First, we show the superconducting phases in the absence of the SOC. Figure 3.6 (a) (Figure 3.6 (b)) shows phase diagrams as a function of the interlayer hopping t' (carrier density n) and Coulomb interaction U at $n = 0.1$ ($t'/t = 0.5$). Owing to the dominant FM spin fluctuations, odd-parity spin-triplet $f_{x(x^2-3y^2)}$-wave superconducting states, which are classified into A_{2u} or E_u IRs in the presence of the SOC, are stabilized in the whole parameter region. This $f_{x(x^2-3y^2)}$-wave superconducting state is a full gap state and mainly caused by intralayer Cooper pairing. The gap function for the $f_{x(x^2-3y^2)}$-wave superconducting state is almost the same as Fig. 3.10 (a). Since the effective pairing interaction for spin-triplet superconductivity is approximated as $V^{\text{triplet}} \simeq -(U^2/2)\chi^S$ in the absence of SOC, the magnetic fluctuation favors the gap function with the same sign on each pieces of the Fermi surface connected by a vector $\boldsymbol{Q}$. Here, $\boldsymbol{Q}$ is the wave vector at which the magnetic susceptibility is enhanced. As shown in Fig. 3.3 (c), the magnetic susceptibility is sharply peaked at $\boldsymbol{q} \simeq \boldsymbol{0}$ (i.e., $\boldsymbol{Q} \simeq \boldsymbol{0}$). Thus, the $f_{x(x^2-3y^2)}$-wave superconducting state is stabilized to avoid generation of gap nodes at the K and K′ points [143, 144].

3.4.2 Superconductivity and spin-orbit coupling

Next, we investigate superconductivity in the presence of the layer-dependent staggered SOC. In the following discussion, we describe the superconducting gap function as $\Delta^i_{ms,m's'}(k) = \sum_{\mu\nu} d^{\mu\nu}_i(k)\bar{\sigma}^\mu_{ss'}\tau^\nu_{mm'}$, where $i = 1, 2$ is the index for two-dimensional IRs and $\bar{\sigma}^\mu_{ss'} = [\sigma^\mu i\sigma^y]_{ss'}$ ($\mu = 0, x, y, z$). In the presence of the SOC, symmetry of superconducting states is classified based on the crystallographic point group. Then, the gap function belongs to one of IRs of
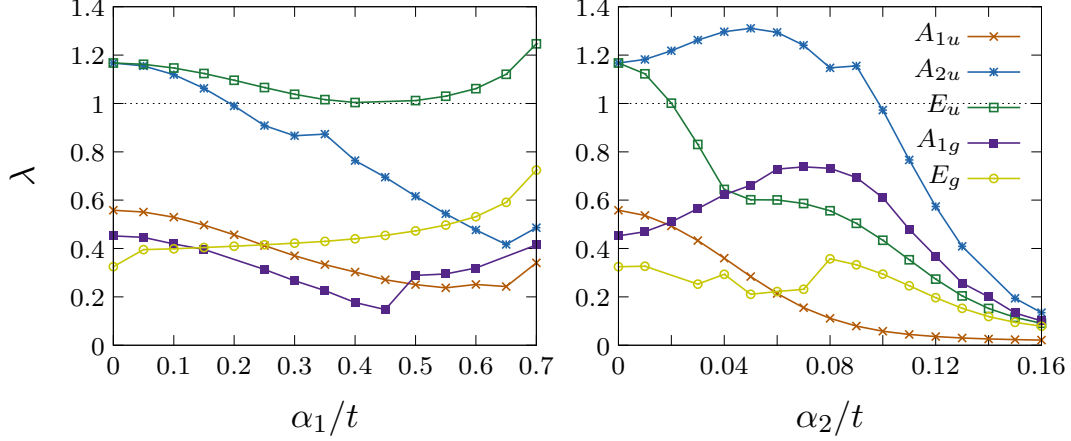
Fig. 3.7. SOC dependence of eigenvalues of the Eliashberg equation λ at $t'/t = 0.2$, $n = 0.1$, $U = 4.8$, and $T = 0.02$. The eigenvalues for A_{1u} (p-wave), A_{2u} ($f_{x^2(x^2-3y^2)}$-wave), E_u ($f_{x^2(x^2-3y^2)}$-wave or p-wave), A_{1g} (s-wave), and E_g (d-wave) pairing states are illustrated.
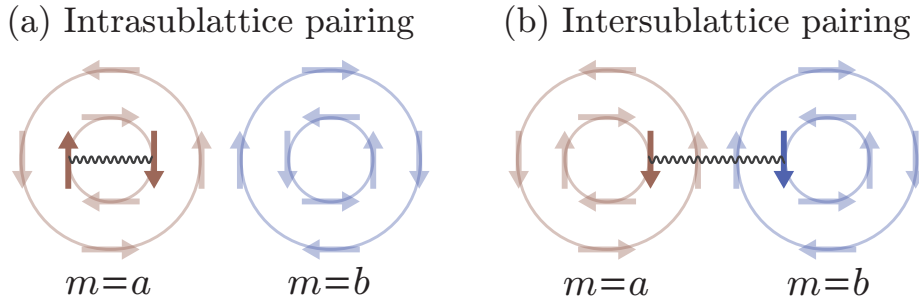
D_{3d} point group shown in Table 3.1. The superconducting instability is discussed by solving the Eliashberg equation under symmetry constraints for each of the IRs (see Appendix B). Note that the symmetry constraints are technically introduced to avoid numerical errors.

Table 3.1. Two-dimensional basis gap functions for the IRs of trigonal D_{3d} point group without sublattice degrees of freedom. The second column shows the compatibility relations between D_{3d} and C_{3v}.

D_{3d}	$D_{3d} \downarrow C_{3v}$	Basis functions with $k_z = 0$
A_{1g}	A_1	$\bar{\sigma}^0$
A_{2g}	A_2	$k_x k_y (k_x^2 - 3k_y^2)(3k_x^2 - k_y^2)\bar{\sigma}^0$
E_g	E	$\{k_x k_y, k_x^2 - k_y^2\}\bar{\sigma}^0$
A_{1u}	A_2	$k_x \bar{\sigma}^x + k_y \bar{\sigma}^y,\ k_y(3k_x^2 - k_y^2)\bar{\sigma}^z$
A_{2u}	A_1	$k_x \bar{\sigma}^y - k_y \bar{\sigma}^x,\ k_x(k_x^2 - 3k_y^2)\bar{\sigma}^z$
E_u	E	$\{k_x \bar{\sigma}^y + k_y \bar{\sigma}^x, k_x \bar{\sigma}^x - k_y \bar{\sigma}^y\},\ \{k_x, k_y\}\bar{\sigma}^z$ $k_x(k_x^2 - 3k_y^2)\{\bar{\sigma}^x, \bar{\sigma}^y\},\ k_y(3k_x^2 - k_y^2)\{\bar{\sigma}^x, \bar{\sigma}^y\}$

Figure 3.7 shows the SOC dependence of eigenvalues of the Eliashberg equation λ at $t'/t = 0.2$, $n = 0.1$, and $U = 4.8$. Owing to the dominant FM fluctuation, the intralayer $f_{x(x^2-3y^2)}$-wave (A_{2u} or E_u) pairing state is predominant and the p-wave (A_{1u}, A_{2u}, or E_u) pairing state is subdominant for $\alpha_j = 0$. On the other hand, the eigenvalues of even-parity s-wave (A_{1g}) and d-wave (E_g) pairing states are smaller than those of odd-parity pairing states. The eigenvalues of the A_{2u} and E_u superconducting states are equal at $\alpha_j = 0$, since the spin part of the gap function is threefold degenerated in the absence of the SOC. By turning on the staggered Rashba (Zeeman) SOC, the degeneracy is lifted due to violation of the spin rotational symmetry, and the E_u (A_{2u}) superconducting state is stabilized as $\lambda^{A_{2u}} < \lambda^{E_u}$ ($\lambda^{A_{2u}} > \lambda^{E_u}$). For

these parameters, the spin direction of the superconducting state is determined by the selection rule for locally NCS superconductors [31, 38], which originates from a modulation of the one-particle Green's function by the staggered SOC. As explained in Sec. 1.1, the selection rule determines the symmetry of the stable superconducting state depending on whether the leading superconducting order parameter is intrasublattice component or intersublattice component [see Fig. 3.8 for an illustration]. For intrasublattice pairing, the spin-singlet superconducting state or spin-triplet superconducting state with $d(k) \parallel g(k)$ are stabilized. On the other hand, only the spin-triplet superconducting state with $d(k) \perp g(k)$ is stable for intersublattice pairing. In a small SOC region, the leading order parameter for the A_{2u} (E_u) pairing state possesses the intralayer $f_{x(x^2-3y^2)}$-wave symmetry with $d \parallel \hat{z}$ ($d \parallel \hat{x}, \hat{y}$). Thus, the A_{2u} (E_u) superconducting state is destabilized by the staggered Rashba (Zeeman) SOC, since the leading intralayer order parameter with $d \perp g_1$ ($d \perp g_2$) is incompatible with the selection rule. In addition, to be compatible with the selection rule, the gap function is modified in a large SOC region. For example, the leading order parameter of the E_u pairing state exhibits p-wave symmetry for $\alpha_2/t \gtrsim 0.04$, while that shows $f_{x(x^2-3y^2)}$-wave symmetry for $\alpha_2/t \lesssim 0.04$ [see right panel of Fig. 3.7]. As demonstrated above, competition of various superconducting states with different pairing symmetry can be controlled by the staggered SOC.

(a) Intrasublattice pairing $\qquad$ (b) Intersublattice pairing

$\qquad m=a \qquad\qquad m=b \qquad\qquad\qquad m=a \qquad\qquad m=b$

Fig. 3.8. Schematic figure of the Cooper pairing in a two-sublattice system with the staggered Rashba SOC. The spin texture, which is opposite in each sublattice, can be defined in the absence of intersublattice hybridization as shown in the figure. (a) By choosing the Rashba-type g-vector $g(k)$ as the spin quantization axis at each momentum, an intrasublattice Cooper pair wave function can be described as $\Psi_k^{\text{intra}} = |k, \sigma; a\rangle |-k, \bar{\sigma}; a\rangle$, where $|k, \sigma; m\rangle$ denotes the wave function for an electron with momentum k and spin σ on sublattice $m = a, b$. Ψ_k^{intra} is decomposed to the spin-singlet state and spin-triplet state with $d(k) \parallel g(k)$, and hence only these pairing states are stabilized for intrasublattice pairing. (b) A Cooper pair wave function for the intersublattice pairing state is described as $\Psi_k^{\text{inter}} = |k, \sigma; a\rangle |-k, \sigma; b\rangle$. This means that the spin-triplet pairing state with $d(k) \perp g(k)$ is stable for intersublattice pairing.

As explained in Sec. 1.1, the selection rule is derived in the framework of the mean-field theory with assuming a simple pairing interaction [31]. Therefore, it is uncertain whether or not the selection rule holds in the presence of the modification of the effective pairing interaction by the SOC and Coulomb interaction, although it looks to hold in Fig. 3.7. In

order to clarify the applicability of the selection rule in this model, we investigate detailed behaviors of the superconductivity against the staggered SOC and Coulomb interaction in the following part. Figure 3.9 shows phase diagrams as a function of the staggered SOC α_j and Coulomb interaction U. We found that an odd-parity superconducting state with either A_{2u} or E_u symmetry is stabilized and it is controlled by magnitude of the SOC and Coulomb interaction. The gap functions for these odd-parity superconducting states are illustrated in Table 3.2 and Figs. 3.10 and 3.11. It should be noticed that the Zeeman SOC significantly affects the superconductivity compared to the Rashba SOC because the Zeeman SOC takes a large magnitude near the K point. Therefore, superconductivity in a trigonal system with in-plane inversion symmetry breaking is affected by a moderate SOC.
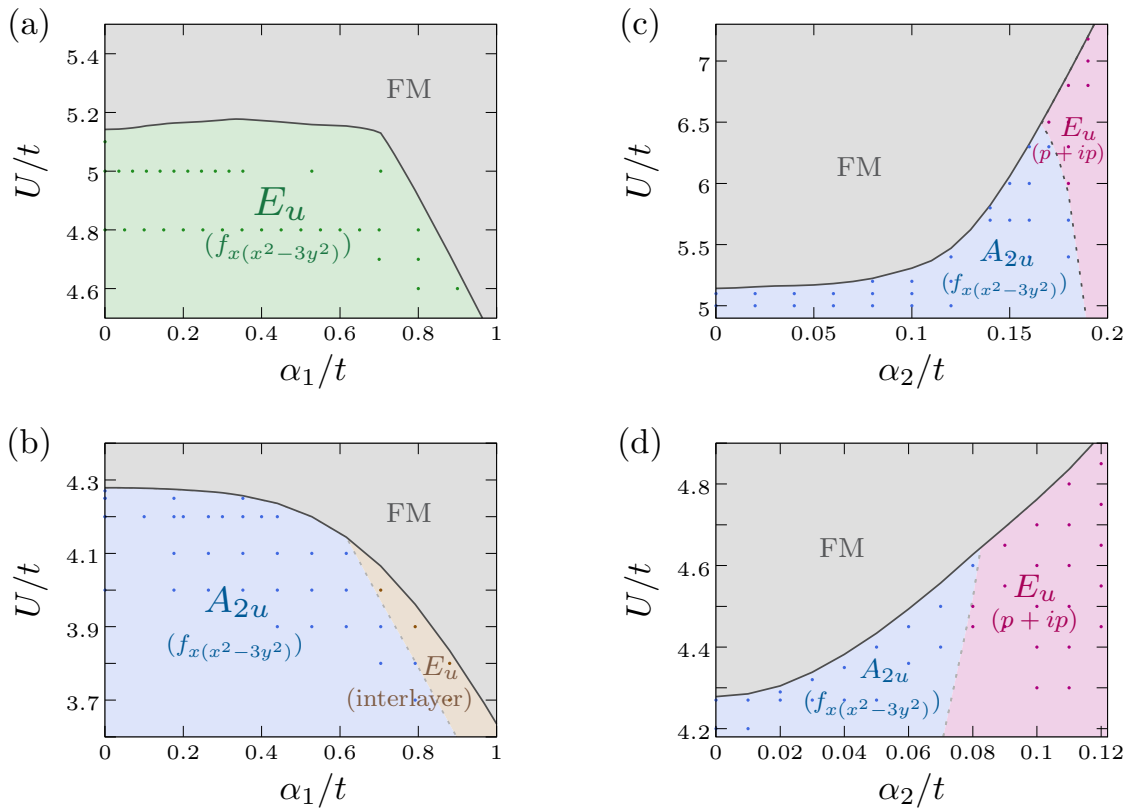
Fig. 3.9. (a) and (b) Phase diagram for the Coulomb interaction U and staggered Rashba SOC α_1 at $\alpha_2 = 0$ and $T = 0.02$. (c) and (d) Phase diagram for the Coulomb interaction U and staggered Zeeman SOC α_2 at $\alpha_1 = 0$ and $T = 0.02$. (a) and (c) $t'/t = 0.2$ and $n = 0.1$, while (b) and (d) $t'/t = 0.5$ and $n = 0.12$. The solid line is the phase boundary between FM-like ordered state and paramagnetic state. In the paramagnetic phase, the odd-parity A_{2u} and E_u superconducting states are illustrated.

In the presence of the Rashba SOC, the superconductivity exhibits different behaviors depending on the magnitude of the interlayer hopping. In the case of a small interlayer hopping $t'/t = 0.2$, the staggered Rashba SOC stabilizes only the E_u superconducting state [Fig. 3.9 (a)], whose leading order parameters are intralayer spin-triplet components $\{d_1^{y0}, d_2^{x0}\}$ with $f_{x(x^2-3y^2)}$-wave symmetry [Figs. 3.11 (a) and 3.11 (b)]. This E_u $f_{x(x^2-3y^2)}$-wave superconducting state

Table 3.2. Leading order parameters and parity-mixing-induced components for the odd-parity A_{2u} and E_u superconducting states. Δ^s, Δ^{px}, Δ^{py}, $\Delta^{d_{x^2-y^2}}$, $\Delta^{d_{xy}}$, and Δ^f denote gap functions which possess momentum dependence with s-wave, p_x-wave, p_y-wave, $d_{x^2-y^2}$-wave, d_{xy}-wave, and $f_{x(x^2-3y^2)}$-wave symmetry. The third column shows the phase diagram in which the corresponding superconducting state is stabilized. The last column indicates figures which illustrate the gap functions.

IR	Leading component	Parity mixing	Phase diagram	Gap function
A_{2u}	$\Delta^f \bar{\sigma}^z \tau^0$	$\Delta^s \bar{\sigma}^0 \tau^z$	Figs. 3.9 (b), (c), (d)	Fig. 3.10
	$\{\Delta^f \bar{\sigma}^y, \Delta^f \bar{\sigma}^x\}\tau^0$		Fig. 3.9 (a)	Figs. 3.11 (a), (b)
E_u	$\{\Delta^{px}, \Delta^{py}\}\bar{\sigma}^z \tau^0$	$\{\Delta^{d_{x^2-y^2}}, \Delta^{d_{xy}}\}\bar{\sigma}^0 \tau^z$	Figs. 3.9 (c), (d)	Figs. 3.11 (c), (d)
	$\{\Delta^f \tau^x, \Delta^s \tau^y\}\bar{\sigma}^z$		Fig. 3.9 (b)	Figs. 3.11 (e), (f)

is compatible with the selection rule as we already demonstrate for Fig. 3.7. On the other hand, in the case of a large interlayer hopping $t'/t = 0.5$, the A_{2u} or E_u superconducting states are stabilized depending on the magnitude of the Rashba SOC [Fig. 3.9 (b)]. The A_{2u} superconducting state is favored for a small Rashba SOC region ($0 \lesssim \alpha_1/t \lesssim 0.8$), while the E_u superconducting state is favored for a large Rashba SOC region ($\alpha_1/t \gtrsim 0.8$). This multiple superconducting phase diagram is a consequence of competition between the selection rule and magnetic anisotropy. The A_{2u} superconducting state with the $f_{x(x^2-3y^2)}$-wave leading order parameter d^{z0} is incompatible with the selection rule because $\boldsymbol{d} \perp \boldsymbol{g}_1$ in the whole Brillouin zone. The stabilization of the A_{2u} superconducting state may be attributed to the magnetic anisotropy. The magnetic anisotropy under the Rashba SOC is always $\chi^\perp > \chi^\parallel$ near the Γ point like that for $t'/t = 0.2$ [see Fig. 3.5 (b)]. Since the effective pairing interaction for the spin-triplet pair amplitude $d^{z\nu}$ can be approximated as $V^{\text{eff}} \approx -(U^2/2)(2\chi^\perp - \chi^\parallel)$, the magnetic anisotropy $\chi^\perp > \chi^\parallel$ favors the spin-triplet pairing with $\boldsymbol{d} \parallel \hat{z}$. Thus, the A_{2u} superconducting state is stabilized contrary to the selection rule. Note that impacts of a sublattice-dependent staggered SOC on the electronic structure are generally weakened by increasing the intersublattice coupling [165]. Thus, the selection rule is less important for larger t'/t. Leading order parameter of the E_u superconducting state for $\alpha_1/t \gtrsim 0.8$ is interlayer spin-triplet components $\{d_1^{zx}, d_2^{zy}\}$ [Figs. 3.11 (e) and 3.11 (f)], which are compatible with the selection rule. The enhancement of the interlayer order parameters $\{d_1^{zx}, d_2^{zy}\}$ is attributed to the large interlayer coupling and magnetic anisotropy $\chi^\perp > \chi^\parallel$. Note that the interlayer component of the effective interaction vertex $\hat{V}(q)$ [Eq. (3.8)] is induced by a finite interlayer hopping contained in the RPA susceptibility $\hat{\chi}(q)$, although the original electron-electron interaction $\mathcal{H}_{\text{int}}$ [Eq. (3.6)] does not couple the layers.

We also investigated superconductivity based on the Kohn-Luttinger framework within the second order perturbation theory [178]. In this approximation, the intrasublattice E_u $f_{x(x^2-3y^2)}$-

wave state is always stable and we do not find violation of the selection rule. This is because the magnetic anisotropy in the bare susceptibility is weak and its effect on superconductivity is negligible. In other words, exchange enhancement of magnetic anisotropy, that is taken into account in the RPA, plays an essential role to stabilize the A_{2u} state violating the selection rule.

On the other hand, the superconducting phase diagram in the presence of the Zeeman SOC is qualitatively the same irrespective of the magnitude of the interlayer hopping [Figs. 3.9 (c) and 3.9 (d)]. The staggered Zeeman SOC stabilizes the A_{2u} or E_u superconducting states, depending on magnitude of the Zeeman SOC. The A_{2u} superconducting state is stabilized in a small Zeeman SOC region, while the E_u superconducting state is stabilized in a large Zeeman SOC region. Both superconducting states are indeed compatible with the selection rule. The leading order parameter for the A_{2u} (E_u) superconducting state is d^{z0} ($\{d_1^{z0}, d_2^{z0}\}$) with $f_{x(x^2-3y^2)}$-wave (p-wave) symmetry [Fig. 3.10 (a)] ([Figs. 3.11 (c) and 3.11 (d)]). Note that the leading order parameter for the E_u superconducting state changes as $\{d_1^{y0}, d_2^{x0}\}$ ($f_{x(x^2-3y^2)}$-wave) $\rightarrow \{d_1^{z0}, d_2^{z0}\}$ (p-wave) by increasing the SOC α_2 so as to be compatible with the selection rule. The stabilization of the E_u superconducting state against the A_{2u} superconducting state may be attributed to the local parity-mixing effect for the intralayer pairing. In locally NCS crystals, local parity-mixing effect induces an intrasublattice staggered spin-singlet (spin-triplet) component for odd-parity (even-parity) superconducting states. The symmetry of the parity-mixing-induced component is determined by the compatibility relation between the global symmetry and the local site symmetry. In our model, the global and local site symmetries are classified as D_{3d} and C_{3v}, respectively. Then, the local parity-mixing occurs between A_{1g} and A_{2u}, A_{2g} and A_{1u}, and E_g and E_u [see second column of Table 3.1] at each layer. As shown in Fig. 3.10, the local parity-mixing effect induces an s-wave component d^{0z} in the A_{2u} superconducting state, and it becomes comparable to the leading $f_{x(x^2-3y^2)}$-wave component d^{z0} in the large Zeeman SOC region. On the other hand, an intrasublattice staggered d-wave component [not shown] appears in the E_u superconducting state as a consequence of the local parity-mixing effect. Since the s-wave pairing is unfavorable in the presence of the Coulomb interaction, the strongly parity-mixed $f + s$-wave A_{2u} superconducting state is overwhelmed by the $p + d$-wave E_u superconducting state in the large Zeeman SOC region. The critical value $\alpha_2 \sim 0.1$ corresponds to $\alpha_2 = 20$ meV when we adopt $t = 200$ meV [167]. This value lies in the realistic range of TMDs. Finally we note that the competition between the selection rule and magnetic anisotropy does not occur in the case of the Zeeman SOC, in contrast to the case of the Rashba SOC.

3.4.3 Topological superconductivity

Finally, we discuss topological superconductivity. The $\mathbb{Z}_2$ part of topological invariants for the odd-parity superconducting states is determined by the occupation numbers at the time-
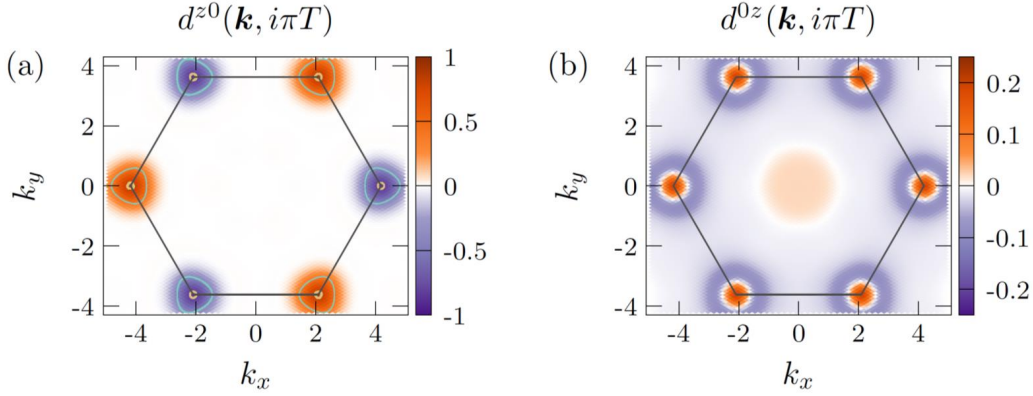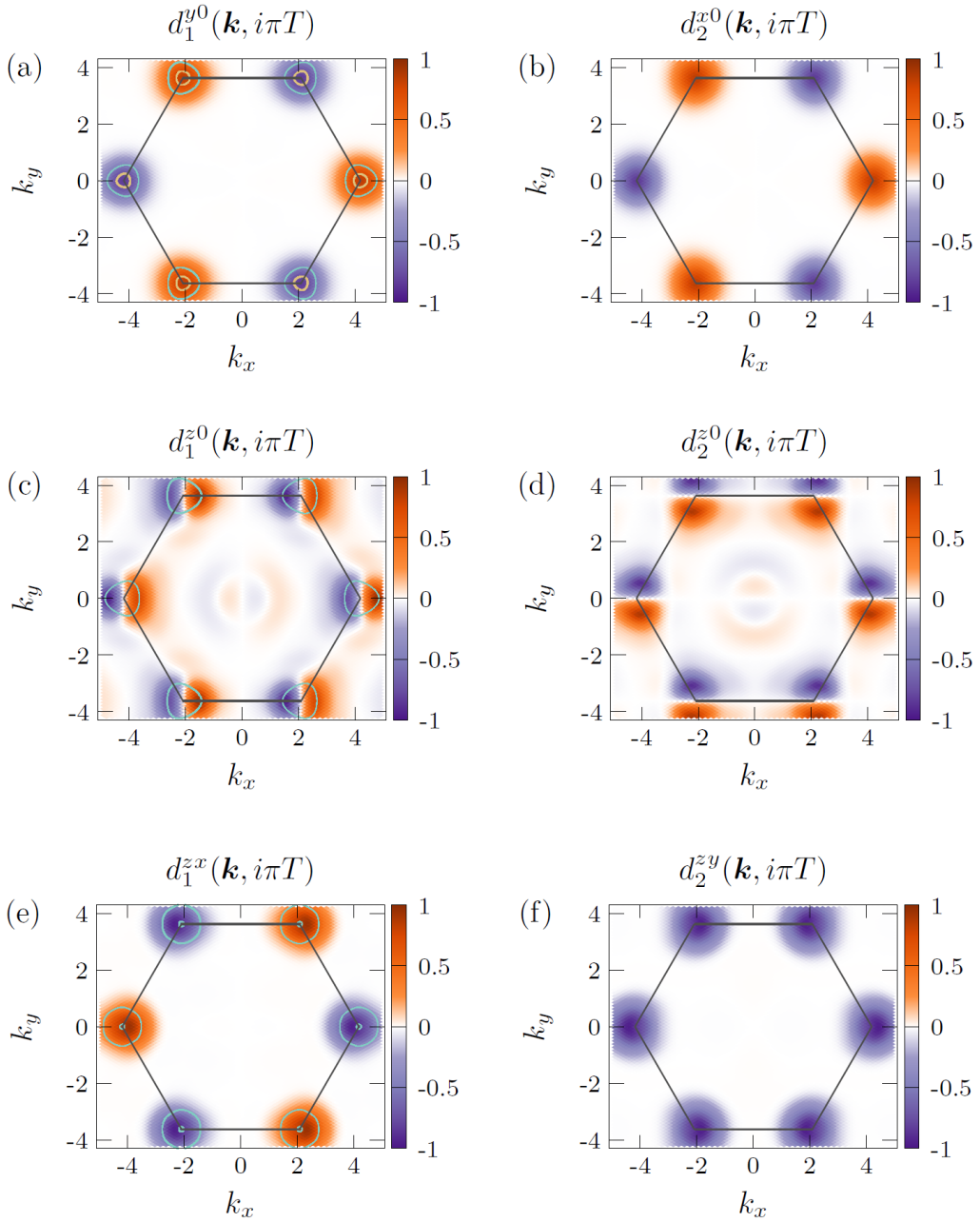
Fig. 3.10. Gap functions for the A_{2u} superconducting state at $t'/t = 0.2$, $n = 0.1$, $\alpha_2 = 0.1$, and $U = 5.2$. (a) Leading intralayer $f_{x(x^2-3y^2)}$-wave component $d^{z0}(\boldsymbol{k}, i\pi T)$ and (b) parity-mixing-induced s-wave component $d^{0z}(\boldsymbol{k}, i\pi T)$. The gap functions are normalized so that the maximum amplitude of the leading order parameter becomes unity. Corresponding Fermi surface is illustrated in the left panel. Eigenvalues of the Eliashberg equation is $\lambda = 2.83905$.

reversal invariant momenta in the Brillouin zone [123–125]. In our model, the number of disconnected Fermi surfaces enclosing the time-reversal invariant momenta (Γ and M points) is even. Thus, the $\mathbb{Z}_2$ invariant for a time-reversal invariant odd-parity superconducting state (DIII class) is trivial. The superconducting states that belong to one-dimensional IRs do not break the time-reversal symmetry, and hence the A_{1u} and A_{2u} superconducting states are topologically trivial.

On the other hand, the superconducting states classified into two-dimensional IRs may realize spontaneous time-reversal symmetry breaking, depending on the superposition of two gap functions. Then, the integer topological invariant (Chern number in class D) can be a nonzero even number. For instance, the E_u p-wave superconducting state in a large Zeeman SOC region [Figs. 3.9 (c) and 3.9 (d)] should be a chiral $p_x + ip_y$ paring state in order to fully gap out the Fermi surface (i.e., the order parameter is written as $\sim (\Delta^{p_x} \pm i\Delta^{p_y})\bar{\sigma}^z\tau^0$). This E_u $p_x + ip_y$-wave pairing state is identified as a topological superconducting state in class D with the Chern number $\nu_{\text{Ch}} = \pm 4$ (see Appendix D). A similar topological superconducting state is proposed in monolayer TMDs [173], while it is a parity-mixed chiral $p + d$-wave pairing state owing to violation of the global inversion symmetry.

In contrast, the E_u f-wave superconducting states under the Rashba SOC do not break the time-reversal symmetry, and therefore, they are topologically trivial. In order to fully gap out the Fermi surface, indeed, the order parameter for the E_u $f_{x(x^2-3y^2)}$-wave pairing state [Fig. 3.9 (a)] should be $\sim \Delta^f(\bar{\sigma}^x \pm \bar{\sigma}^y)\tau^0$, while that for the E_u interlayer pairing state [Fig. 3.9 (b)] should be $\sim (\Delta^f\tau^x \pm \Delta^s\tau^y)\bar{\sigma}^z$. Time-reversal symmetry is preserved, while these states may realize nematic superconductivity with spontaneous rotation symmetry breaking. When we assume superposition breaking the time-reversal symmetry, the non-unitary superconducting

Fig. 3.11. Leading components of the gap function for the E_u superconducting states. (a), (b) $t'/t = 0.2$, $n = 0.1$, $\alpha_1 = 0.35204$, and $U = 5.0$. (c), (d) $t'/t = 0.2$, $n = 0.1$, $\alpha_2 = 0.19$, and $U = 7.18$. (e), (f) $t'/t = 0.5$, $n = 0.12$, $\alpha_1 = 0.8801$, and $U = 3.8$. The gap functions are normalized so that the maximum amplitude of the leading order parameter becomes unity. Corresponding Fermi surfaces are illustrated in the left panels. Eigenvalues of the Eliashberg equation is $\lambda = 2.1145, 1.04829, 2.32491$ in (a,b), (c,d), and (e,f), respectively.

state gains less condensation energy, and it is unstable.

3.5 Discussion and summary

In summary, we have studied unconventional superconductivity in a two-dimensional locally NCS triangular lattice, which is relevant to the crystal structure of bilayer TMDs with $2H_b$ stacking. By assuming disconnected Fermi surfaces and strong electron correlation, we have clarified the dominant FM spin fluctuations on the basis of the RPA. The significant enhancement of the FM fluctuation is assisted by the type-II vHS due to a finite interlayer coupling, and hence it is a characteristic of the bilayer structure. The superconducting instability has been discussed based on the analysis of the linearized Eliashberg equation. The odd-parity spin-triplet superconductivity is favored by the FM fluctuation, and we found that fully gapped f-wave pairing state is stabilized in a wide range of the interlayer coupling and carrier density. Furthermore, impacts of the staggered Rashba or Zeeman antisymmetric SOC on the magnetic fluctuation and superconductivity have been elucidated. The magnetic anisotropy is enhanced by increasing the SOC, and a FM-like magnetic structure with in-plane spin alignment, such as in a few-layer VSe_2 [168], is favored by either Rashba or Zeeman SOC. We found that the odd-parity A_{2u} or E_u superconducting states with either f-wave or p-wave gap functions are stabilized depending on magnitude of the SOC, interlayer hopping, and Coulomb interaction. The stability of each odd-parity superconducting states is determined by a combination of the selection rule for locally NCS superconductors [31, 38], magnetic anisotropy, and local parity-mixing effect in the superconducting state. In addition, topological properties of the stable odd-parity pairing states have been studied based on the Fermi surface formula [123–125] and estimation of topological invariants. Then, the E_u $p + ip$-wave pairing state has been identified as a topological superconducting state in class D with the Chern number $\nu_{Ch} = 4$. This state is stabilized by a moderate Zeeman SOC realistic in TMDs.

Our results suggest odd-parity superconductivity ubiquitous in $2H_b$-stacked bilayer TMDs, such as bilayer MoS_2 in which gate-induced superconductivity is realized [175, 179]. An essential ingredient for the odd-parity superconductivity is underlying FM fluctuations induced by a strong electron correlation. Although dominance of the electron-phonon coupling for the superconductivity in a few-layer TMDs is proposed by some theoretical studies [180–182], the electron-electron interaction is also expected to affect the superconductivity owing to the d-orbital character of carriers in TMDs [170–173]. Indeed, a recent tunneling spectroscopy measurement for monolayer MoS_2 has revealed anisotropic superconducting gap, which suggests that the microscopic origin of the superconductivity cannot be captured by a conventional phonon-driven mechanism [183]. Evidence of topological superconductivity with topological nodal-points is also obtained in $4H_b$-TaS_2 [174]. Thus, various bilayer TMDs have a potential for hosting FM fluctuations and odd-parity superconductivity. This study clarifies a way to control

odd-parity superconducting phases by SOC and carrier doping, and to realize topological superconductivity in two-dimensional TMDs.

Our study also sheds light on a possibility of odd-parity superconductivity in a variety of two-dimensional magnetic van der Waals materials [184] not only TMDs. In van der Waals materials, strong enhancement of spin fluctuations, which potentially leads to unconventional superconductivity, is expected owing to the two-dimensional nature. In fact, ferromagnetism has been detected in atomically thin film of CrI_3 [185], $Cr_2Ge_2Te_6$ [186], VSe_2 [168], V_5Se_8 [187], and $MnSe_x$ [169]. Such FM van der Waals materials may offer a platform for multiple odd-parity superconducting phases.

Chapter 4

Anapole superconductivity from $\mathcal{PT}$-symmetric mixed-parity interband pairing

4.1   Introduction

Parity symmetry ($\mathcal{P}$-symmetry) and time-reversal symmetry ($\mathcal{T}$-symmetry) are fundamental properties of quantum materials, such as insulators, metals, magnets, and superconductors. Superconductivity is caused by the quantum condensation of either even-parity or odd-parity Cooper pairs corresponding to spin-singlet or spin-triplet superconductivity due to the fermion antisymmetry [163]. The order parameter of conventional superconductors breaks neither $\mathcal{P}$-symmetry nor $\mathcal{T}$-symmetry. However, competition and coexistence of multiple pairing instabilities lead to exotic superconductivity, such as chiral superconductivity with spontaneous $\mathcal{T}$-symmetry breaking [188] related to the nontrivial topology [2, 3] and anomalous transport [189]. In particular, mixed-parity superconductivity with coexistent even- and odd-parity pairing channels has been widely discussed in NCS superconductors [5, 190], ultracold fermion systems [191, 192], and spin-orbit-coupled systems in the vicinity of the $\mathcal{P}$-symmetry breaking [48–50, 193, 194]. As discussed in Sec. 1.3, the $\mathcal{P}$-symmetry is broken in such superconductors, and spontaneous $\mathcal{T}$-symmetry breaking realized by the $\pm\pi/2$ phase difference between even- and odd-parity pairing potentials is energetically favored [8, 62, 63] (Fig. 4.1a) when the SOC due to NCS crystal structure is absent or weak. This class of superconducting states spontaneously breaks both $\mathcal{P}$- and $\mathcal{T}$-symmetries but maintain the combined $\mathcal{PT}$-symmetry. There have been considerable interests in studying such $\mathcal{PT}$-*symmetric mixed-parity superconductivity*. The three-dimensional $s + ip$-wave superconductivity has attracted much theoretical attention as a superconducting analog of axion insulators [195–200]. The $\mathcal{T}$-symmetry breaking mixed-parity pairing has also been theoretically proposed in Sr_2RuO_4 [201]. Furthermore, a

a

b

c
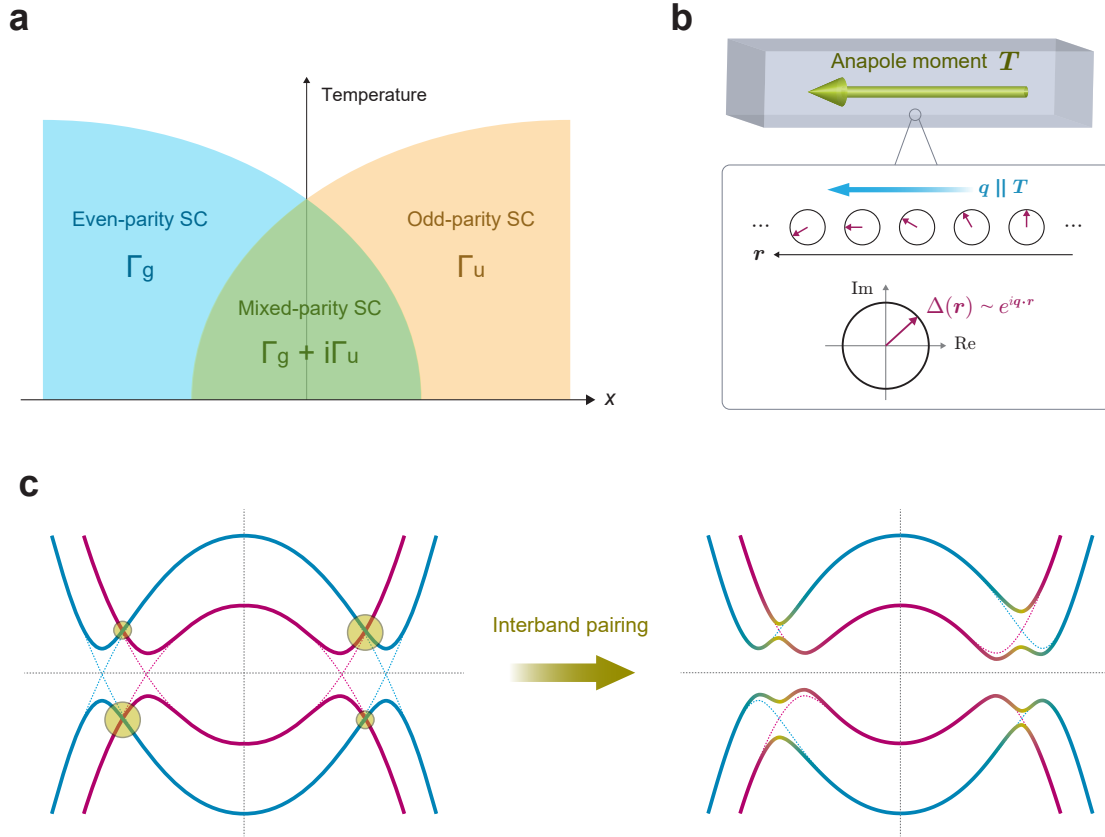
Fig. 4.1. Schematics of $\mathcal{PT}$-symmetric mixed-parity superconductivity. (a) Schematic phase diagram in a superconductor with comparable strength of even- and odd-parity pairing interactions. The transition between the even-parity superconducting phase (Γ_g) and the odd-parity superconducting phase (Γ_u) is induced by tuning a control parameter x. For centrosymmetric systems with $\mathcal{T}$-symmetry, there is generally an intermediate mixed-parity superconducting phase ($\Gamma_g + i\Gamma_u$) where even- and odd-parity pairing components are coexistent with the relative phase difference $\pm\pi/2$. (b) Schematic figure of the anapole superconducting states. In real space, the phase of the superconducting order parameter becomes nonuniform along a direction parallel to the effective anapole moment $\boldsymbol{T}$ as $\Delta(\boldsymbol{r}) \propto e^{i\boldsymbol{q}\cdot\boldsymbol{r}}$ with $\boldsymbol{q} \parallel \boldsymbol{T}$. (c) Illustration for a mechanism of the asymmetric Bogoliubov spectrum in $\mathcal{PT}$-symmetric mixed-parity multiband superconductors. $\mathcal{P}$- and $\mathcal{T}$-symmetry breaking interband pairing induces an asymmetric modulation of the Bogoliubov spectrum.

mixed-parity superconducting state in UTe$_2$ [202] has been predicted to explain experimentally-observed multiple superconducting phases [203–206].

In previous works, the mixed-parity superconductivity has been theoretically studied mainly in single-band models for spin-1/2 fermions [8, 63, 195–198, 200]. On the other hand, it has recently been recognized that the multiband structure of the Cooper pair's wave function arising from internal electronic degrees of freedom (DOF) (e.g., orbital and sublattice) induces exotic superconducting phenomena. For instance, multiband superconductors have attracted much attention as a platform realizing odd-frequency pairing [119]. In $\mathcal{T}$-symmetry breaking superconductors, an intrinsic anomalous Hall effect emerges owing to the multiband nature of Cooper pairs [189, 207–210]. In particular, even-parity $\mathcal{T}$-symmetry breaking superconductors host topologically protected Bogoliubov Fermi surfaces in the presence of interband pairing [211, 212].

In this chapter, we show that $\mathcal{PT}$-symmetric mixed-parity superconducting states generally exhibit an asymmetric Bogoliubov spectrum in multiband systems, although it is overlooked in single-band models. We demonstrate that such asymmetric deformation of the Bogoliubov spectrum is induced by a nonunitary interband pairing (see Fig. 4.1c), and derive the necessary conditions for generic two-band models. Although we consider two-band systems for simplicity throughout this chapter, our theory is relevant for any multiband superconductors with multiple bands near the Fermi level. In addition, we show that the Bogoliubov quasiparticles with asymmetric Bogoliubov spectrum stabilize the FFLO superconductivity [213, 214], which is evident from the Lifshitz invariants [215], namely linear gradient terms, in the GL free energy. The Lifshitz invariants are nonzero only for the *anapole superconducting states*, whose order parameters are equivalent to an anapole (magnetic toroidal) moment, namely a polar and time-reversal odd multipole [216], from the viewpoint of symmetry. It is shown that the phase of the superconducting order parameter is spatially modulated along the effective anapole moment of the superconducting state (see Fig. 4.1b). The concept of anapole order has been employed in nuclear physics [217], magnetic materials science [216], strongly correlated electron systems [218, 219], and optoelectronics [220, 221], and it is extended to superconductors by this work. In previous works, the FFLO superconductivity has been proposed in the presence of an external magnetic field [14, 213–215] or coexistent magnetic multipole order [55, 56]. However, the magnetic field causes superconducting vortices, prohibiting pure FFLO states, and the proposed multipole superconducting state has not been established in condensed matters. In contrast, the anapole superconductivity realizes the FFLO state without the aid of any other perturbation or electronic order. Note that an intrinsic nonuniform superconducting state has also been discussed in the Bogoliubov Fermi surface states [222], although its mechanism and symmetry are different from those of the anapole FFLO state. Based on the obtained results, we predict the possible asymmetric Bogoliubov spectrum and anapole superconductivity in UTe$_2$, a recently-discovered candidate of a spin-triplet superconductor [134]. The multiple pairing

instabilities [203–206, 223–226] and $\mathcal{T}$-symmetry breaking [227–230] were recently observed there.

The rest of this chapter is organized as follows. In Sec. 4.2, we introduce a generic two-band model for mixed-parity superconducting states. In Sec. 4.3, we study a microscopic mechanism to realize the asymmetric Bogoliubov spectrum in mixed-parity superconducting states. In Sec. 4.4, we show that the FFLO-like nonuniform superconducting state is stabilized by the effective anapole moment based on the Ginzburg-Landau (GL) theory. In Sec. 4.5, we apply our theory to possible mixed-parity superconducting states in UTe$_2$. Finally, we present a discussion and summary in Sec. 4.6.

4.2 Model

We begin our discussion by considering the general form of the BdG Hamiltonian for two-band systems:

$$\mathcal{H} = \frac{1}{2} \sum_{k} (\hat{c}_{k}^{\dagger}, \hat{c}_{-k}^{\mathrm{T}}) \begin{pmatrix} H_0(k) & \Delta(k) \\ \Delta^{\dagger}(k) & -H_0^*(-k) \end{pmatrix} \begin{pmatrix} \hat{c}_{k} \\ \hat{c}_{-k}^* \end{pmatrix}, \tag{4.1}$$

where $\hat{c}_{k}^{\mathrm{T}} = (c_{k1\uparrow}, c_{k1\downarrow}, c_{k2\uparrow}, c_{k2\downarrow})$ is a spinor encoding the four internal electronic DOF stem from spin-1/2 and extra two-valued DOF, such as orbitals and sublattices. Then, the 4×4 matrices $H_0(k)$ and $\Delta(k)$ can be generally expressed as a linear combination of $\sigma_\mu \otimes \tau_\nu$ matrices, where σ_μ and τ_ν ($\mu, \nu = 0, x, y, z$) are the Pauli matrices for the spin and extra DOF, respectively. However, we here introduce a more convenient form of the two-band BdG Hamiltonian using the Euclidean Dirac matrices γ_n ($n = 1, 2, 3, 4, 5$), which satisfy $\{\gamma_m, \gamma_n\} = 2\delta_{mn}$. See Appendix E for the correspondence between the $\sigma_\mu \otimes \tau_\nu$ and Dirac matrices. Assuming that the normal state preserves both $\mathcal{P}$- and $\mathcal{T}$-symmetries, the general form of the normal state Hamiltonian $H_0(k)$ can be expressed as

$$H_0(k) = (\epsilon_k^0 - \mu)\mathbb{1}_4 + \boldsymbol{\epsilon}_k \cdot \boldsymbol{\gamma}, \tag{4.2}$$

where $\mathbb{1}_4$ is the 4×4 unit matrix, $\boldsymbol{\gamma} = (\gamma_1, \gamma_2, \gamma_3, \gamma_4, \gamma_5)$ is the vector of the five Dirac matrices, ϵ_k^0 and $\boldsymbol{\epsilon}_k = (\epsilon_k^1, \epsilon_k^2, \epsilon_k^3, \epsilon_k^4, \epsilon_k^5)$ are the real-valued coefficients of these matrices, and μ is the chemical potential. Whereas ϵ_k^0 is an even function of momentum, k-parity of other coefficients ϵ_k^n ($n > 0$) depends on the details of the extra DOF. The superconducting state is assumed to be a mixture of even- and odd-parity pairing components. The pairing potential $\Delta(k)$ for such mixed-parity superconducting states has the general form

$$\hat{\Delta}(k) = \Delta_1(\eta_k^0 \mathbb{1}_4 + \boldsymbol{\eta}_k \cdot \boldsymbol{\gamma}) + \Delta_2 \sum_{m<n} \eta_k^{mn} i\gamma_m \gamma_n, \tag{4.3}$$

where $\hat{\Delta}(\boldsymbol{k}) \equiv \Delta(\boldsymbol{k})U_T^\dagger$ and U_T is the unitary part of the time-reversal operator. The complex-valued constants Δ_1 and Δ_2 represent the superconducting order parameters for the even- and odd-parity pairing channels, respectively. As a consequence of the fermionic antisymmetry $\Delta(\boldsymbol{k}) = -\Delta^{\mathrm{T}}(-\boldsymbol{k})$, the even-parity (odd-parity) part of $\hat{\Delta}(\boldsymbol{k})$ is expressed by a linear combination of $\mathbb{1}_4$ and γ_n ($i\gamma_m\gamma_n$) as shown in Eq. (4.3) (see Appendix E). The real-valued functions $\eta_{\boldsymbol{k}}^0$, $\boldsymbol{\eta_k} = (\eta_{\boldsymbol{k}}^1, \eta_{\boldsymbol{k}}^2, \eta_{\boldsymbol{k}}^3, \eta_{\boldsymbol{k}}^4, \eta_{\boldsymbol{k}}^5)$, and $\eta_{\boldsymbol{k}}^{mn}$ ($1 \le m < n \le 5$) determines the details of order parameters. Whereas $\eta_{\boldsymbol{k}}^0$ is an even function of momentum, $\boldsymbol{k}$-parity of others $\eta_{\boldsymbol{k}}^n$ and $\eta_{\boldsymbol{k}}^{mn}$ depends on the details of the extra DOF. Note that the $\boldsymbol{k}$-parity of $\eta_{\boldsymbol{k}}^n$ must be the same as that of $\epsilon_{\boldsymbol{k}}^n$. Although we adopt a BCS-type description of superconductivity in this work, we consider that our argument is hardly affected by enhanced quantum fluctuations in low-dimensional systems when the long-range order occurs.

4.3 Asymmetric Bogoliubov spectrum

We here consider general BdG Hamiltonian including more than two band models, and later focus on the two-band models. In the following, we assume that each band is weakly coupled and the intraband pairing is dominant compared to the interband pairing. In such situations, spontaneous $\mathcal{T}$-symmetry breaking with maintaining the $\mathcal{PT}$-symmetry is energetically favored in the mixed-parity superconducting states [8, 63] (see Sec. 1.3 for details), and the symmetry of the superconducting order parameter becomes equivalent to that of odd-parity magnetic multipoles [216]. A characteristic feature of the odd-parity magnetic multipole ordered state is the asymmetric modulation of the band structure [55, 56, 231, 232], which leads to peculiar nonequilibrium responses such as nonreciprocal transport [233], magnetopiezoelectric effect [234–236], and photocurrent generation [220, 221]. Therefore, the appearance of the asymmetric Bogoliubov spectrum is naturally expected in the $\mathcal{PT}$-symmetric mixed-parity superconductors. However, the asymmetric Bogoliubov spectrum is not obtained in single-band models (see later discussions).

4.3.1 $\mathcal{P}, \mathcal{T}$-odd bilinear product

To induce such asymmetric modulation in the Bogoliubov spectrum, effects of the $\mathcal{P}$- and $\mathcal{T}$-symmetry breaking in the particle-particle superconducting channel should be transferred into the particle-hole channel. This suggests that it is not sufficient to consider only the pairing potential $\Delta(\boldsymbol{k})$, since it is not gauge invariant. Instead of $\Delta(\boldsymbol{k})$ alone, we need to consider gauge-invariant bilinear products of $\Delta(\boldsymbol{k})$ and $\Delta^\dagger(\boldsymbol{k})$ [208] in order to reveal conditions for realizing the asymmetric Bogoliubov spectrum. Here, we focus on the simplest bilinear products, that is, $\Delta(\boldsymbol{k})\Delta^\dagger(\boldsymbol{k})$. The parity-odd and time-reversal-odd ($\mathcal{P}, \mathcal{T}$-odd) part of this bilinear product

is calculated as

$$M_-^{(1)}(\boldsymbol{k}) = \frac{1}{2}\left([\hat{\Delta}^g(\boldsymbol{k}), \hat{\Delta}^{u\dagger}(\boldsymbol{k})] + [\hat{\Delta}^u(\boldsymbol{k}), \hat{\Delta}^{g\dagger}(\boldsymbol{k})]\right), \tag{4.4}$$

where $\hat{\Delta}^g(\boldsymbol{k})$ and $\hat{\Delta}^u(\boldsymbol{k})$ are the even- and odd-parity part of $\hat{\Delta}(\boldsymbol{k})$, respectively (see Appendix F for the derivation of Eq. (4.4)). Owing to the gauge invariance and $\mathcal{P}, \mathcal{T}$-odd behavior of $M_-^{(1)}(\boldsymbol{k})$, a nonzero $M_-^{(1)}(\boldsymbol{k})$ can be a measure of the $\mathcal{P}$- and $\mathcal{T}$-symmetry breaking in the particle-hole channel, which permits emergence of the asymmetric Bogoliubov spectrum. Note that the pairing state must be nonunitary to induce a nonzero $M_-^{(1)}(\boldsymbol{k})$, since $M_-^{(1)}(\boldsymbol{k}) = 0$ when $\Delta(\boldsymbol{k})\Delta^\dagger(\boldsymbol{k})$ is proportional to the unit matrix. In analogy with the spin polarization of nonunitary spin-triplet superconducting states in spin-1/2 single-band models [163], the $\mathcal{P}, \mathcal{T}$-odd bilinear product $M_-^{(1)}(\boldsymbol{k})$ can be interpreted as a polarization of an internal DOF in the superconducting state.

4.3.2 Interband pairing

The emergence of a nonzero $\mathcal{P}, \mathcal{T}$-odd bilinear product $M_-^{(1)}(\boldsymbol{k})$ requires the interband pairing. To see this, we consider the problem in the band basis. Since $H_0(\boldsymbol{k})$ is assumed to preserve the $\mathcal{P}$- and $\mathcal{T}$-symmetries, the energy eigenvalues are doubly degenerate and labelled by a pseudospin index. Especially, we choose the so-called manifestly covariant Bloch basis [49], in which the pseudospin index transforms like a true spin-1/2 under time-reversal and crystalline symmetry operations. In this basis, the intraband pairing potential is generally expressed as

$$\Delta_{\boldsymbol{k}} = (\psi_{\boldsymbol{k}} + \boldsymbol{d}_{\boldsymbol{k}} \cdot \boldsymbol{s})is_y, \tag{4.5}$$

where $\boldsymbol{s} = (s_x, s_y, s_z)$ are Pauli matrices in pseudospin space. The complex-valued functions $\psi_{\boldsymbol{k}}$ and $\boldsymbol{d}_{\boldsymbol{k}}$ are even and odd functions of $\boldsymbol{k}$, respectively. Then, in the absence of the interband pairing, the multiband BdG Hamiltonian matrix reduces to a series of decoupled blocks describing spin-1/2 single-band superconductors. The bilinear product for this intraband pairing potential is obtained as

$$\Delta_{\boldsymbol{k}}\Delta_{\boldsymbol{k}}^\dagger = (|\psi_{\boldsymbol{k}}|^2 + |\boldsymbol{d}_{\boldsymbol{k}}|^2)\mathbb{1}_2 + 2\text{Re}(\psi_{\boldsymbol{k}}\boldsymbol{d}_{\boldsymbol{k}}^*) \cdot \boldsymbol{s} + i(\boldsymbol{d}_{\boldsymbol{k}} \times \boldsymbol{d}_{\boldsymbol{k}}^*) \cdot \boldsymbol{s}. \tag{4.6}$$

In Eq. (4.6), the second and third terms are nonunitary components that break $\mathcal{P}$- and $\mathcal{T}$-symmetries, respectively. However, there appears no term breaking both $\mathcal{P}$- and $\mathcal{T}$-symmetries, and hence the $\mathcal{P}, \mathcal{T}$-odd bilinear product for this $\Delta_{\boldsymbol{k}}$ must vanish. This indicates that the interband pairing is necessary for a nonzero $\mathcal{P}, \mathcal{T}$-odd bilinear product $M_-^{(1)}(\boldsymbol{k})$, which is essential for realizing the asymmetric Bogoliubov spectrum. This is also the reason the asymmetric Bogoliubov spectrum is not obtained in single-band models.

As explained in Sec. 1.1, the presence of interband pairing can be characterized by the

so-called superconducting fitness $F(\boldsymbol{k})$ [29, 30], which is defined as

$$F(\boldsymbol{k})U_T = H_0(\boldsymbol{k})\Delta(\boldsymbol{k}) - \Delta(\boldsymbol{k})H_0^*(-\boldsymbol{k}). \tag{4.7}$$

Since a nonvanishing $F(\boldsymbol{k})F^\dagger(\boldsymbol{k})$ quantifies the strength of interband pairing by definition [29, 30], its $\mathcal{P}, \mathcal{T}$-odd part should be nonzero to realize a nonvanishing $M_-^{(1)}(\boldsymbol{k})$. The $\mathcal{P}, \mathcal{T}$-odd part of $F(\boldsymbol{k})F^\dagger(\boldsymbol{k})$ is obtained as

$$M_-^{(2)}(\boldsymbol{k}) = \frac{1}{2}\left([F^g(\boldsymbol{k}), F^{u\dagger}(\boldsymbol{k})] + [F^u(\boldsymbol{k}), F^{g\dagger}(\boldsymbol{k})]\right), \tag{4.8}$$

where $F^g(\boldsymbol{k})$ and $F^u(\boldsymbol{k})$ are the even- and odd-parity part of $F(\boldsymbol{k})$, respectively. If the normal state preserves both $\mathcal{P}$- and $\mathcal{T}$-symmetries, they are obtained as $F^{g,u}(\boldsymbol{k}) = [H_0(\boldsymbol{k}), \hat{\Delta}^{g,u}(\boldsymbol{k})]$ and $M_-^{(2)}(\boldsymbol{k})$ can be explicitly written as

$$M_-^{(2)}(\boldsymbol{k}) = \frac{1}{2}\left(\left[[H_0(\boldsymbol{k}), \hat{\Delta}_g(\boldsymbol{k})], [\hat{\Delta}_u^\dagger(\boldsymbol{k}), H_0(\boldsymbol{k})]\right] + \left[[H_0(\boldsymbol{k}), \hat{\Delta}_u(\boldsymbol{k})], [\hat{\Delta}_g^\dagger(\boldsymbol{k}), H_0(\boldsymbol{k})]\right]\right). \tag{4.9}$$

Note that the $\mathcal{P}, \mathcal{T}$-odd part of $F(\boldsymbol{k})F^\dagger(\boldsymbol{k})$ can be extracted in the same way as $\Delta(\boldsymbol{k})\Delta^\dagger(\boldsymbol{k})$ [compare Eq. (4.8) with Eq. (4.4)], since the transformation of $F(\boldsymbol{k})F^\dagger(\boldsymbol{k})$ under space-inversion $\mathcal{P}$ and time-reversal $\mathcal{T}$ can be described in the same way as that of $\Delta(\boldsymbol{k})\Delta^\dagger(\boldsymbol{k})$. Based on Eq. (4.8), not only the pair potential $\Delta(\boldsymbol{k})$ but also the normal part $H_0(\boldsymbol{k})$ must satisfy a proper condition to realize $M_-^{(2)}(\boldsymbol{k}) \neq 0$ and asymmetric Bogoliubov spectrum.

4.3.3   Application to two-band model

From the above discussions, we conclude that the necessary (but not sufficient) condition for the asymmetric Bogoliubov spectrum can be written as $M_-^{(1)}(\boldsymbol{k}) \neq 0 \cap M_-^{(2)}(\boldsymbol{k}) \neq 0$, which implies the superconductivity-driven $\mathcal{P}$- and $\mathcal{T}$-symmetry breaking in the particle-hole channel. We here write down this necessary condition for the general two-band BdG Hamiltonian. By substituting Eqs. (4.2) and (4.3) to Eqs. (4.4) and (4.8), we obtain the $\mathcal{P}, \mathcal{T}$-odd bilinear products $M_-^{(1)}(\boldsymbol{k})$ and $M_-^{(2)}(\boldsymbol{k})$ as follows:

$$M_-^{(1)}(\boldsymbol{k}) = 2\mathrm{Im}(\Delta_1\Delta_2^*)\sum_{m<n}\eta_{\boldsymbol{k}}^{mn}(\eta_{\boldsymbol{k}}^n\gamma_m - \eta_{\boldsymbol{k}}^m\gamma_n), \tag{4.10}$$

$$M_-^{(2)}(\boldsymbol{k}) = \mathrm{Tr}[M_-^{(1)}(\boldsymbol{k})\tilde{H}_0(\boldsymbol{k})]\tilde{H}_0(\boldsymbol{k}), \tag{4.11}$$

where $\tilde{H}_0(\boldsymbol{k}) \equiv H_0(\boldsymbol{k}) - (\epsilon_{\boldsymbol{k}}^0 - \mu)\mathbb{1}_4$. We see that $M_-^{(1)}(\boldsymbol{k})$ appears inside the expression of $M_-^{(2)}(\boldsymbol{k})$, and hence the necessary condition for the asymmetric Bogoliubov spectrum can be simplified as $\mathrm{Tr}[M_-^{(1)}(\boldsymbol{k})\tilde{H}_0(\boldsymbol{k})] \neq 0$ in two-band models. Note that it is not clear whether $M_-^{(2)}(\boldsymbol{k})$ can be written in terms of $M_-^{(1)}(\boldsymbol{k})$ in more than two band models since Equation (4.11)

is derived for the general two-band model by using the properties of Dirac matrices. From Eqs. (4.10) and (4.11), the necessary condition (i.e., $\text{Tr}[M_-^{(1)}(\boldsymbol{k})\tilde{H}_0(\boldsymbol{k})] \neq 0$) can be summarized as following two criteria; (i) the relative phase difference between even- and odd-parity pairing potentials must be nonzero so that $\text{Im}(\Delta_1\Delta_2^*) \neq 0$, and (ii) the BdG Hamiltonian must satisfy $\epsilon_{\boldsymbol{k}}^m \eta_{\boldsymbol{k}}^n \eta_{\boldsymbol{k}}^{mn} \neq 0$ or $\epsilon_{\boldsymbol{k}}^n \eta_{\boldsymbol{k}}^m \eta_{\boldsymbol{k}}^{mn} \neq 0$ for $1 \leq {}^{\exists}m < {}^{\exists}n \leq 5$. Interpretations of these requirements in the $\sigma_\mu \otimes \tau_\nu$ basis are shown in Appendix E.

We now confirm that the asymmetric Bogoliubov spectrum indeed appears when the above two criteria are fulfilled. A minimal two-band model satisfying the criterion (ii) can be obtained by substituting $\boldsymbol{\epsilon_k} = r\epsilon_{\boldsymbol{k}}^a \boldsymbol{e}_a + (1-r)\epsilon_{\boldsymbol{k}}^b \boldsymbol{e}_b$, $\boldsymbol{\eta_k} = (1-r)\eta_{\boldsymbol{k}}^a \boldsymbol{e}_a + r\eta_{\boldsymbol{k}}^b \boldsymbol{e}_b$, and $\eta_{\boldsymbol{k}}^{mn} = \delta_{ma}\delta_{nb}\eta_{\boldsymbol{k}}^{ab}$ into Eqs. (4.2) and (4.3). Here, a and b are specific integers satisfying $1 \leq a < b \leq 5$, $\boldsymbol{e}_n$ is the unit vector for the n-th component, and r takes the value either 0 or 1. Under this setup, we can analytically diagonalize the BdG Hamiltonian as

$$\begin{pmatrix} H_0(\boldsymbol{k}) & \Delta(\boldsymbol{k}) \\ \Delta^\dagger(\boldsymbol{k}) & -H_0^*(-\boldsymbol{k}) \end{pmatrix} \rightarrow \text{diag}(E_{\boldsymbol{k}}^+ \mathbb{1}_2, E_{\boldsymbol{k}}^- \mathbb{1}_2, -E_{-\boldsymbol{k}}^+ \mathbb{1}_2, -E_{-\boldsymbol{k}}^- \mathbb{1}_2), \qquad (4.12)$$

where $\mathbb{1}_2$ is the 2×2 unit matrix. Based on the correspondence between the Dirac matrices and $\sigma_\mu \otimes \tau_\nu$ matrices (see Appendix E), the energy spectrum $E_{\boldsymbol{k}}^\pm$ can be obtained as

$$E_{\boldsymbol{k}}^\pm = \sqrt{\xi_{\boldsymbol{k}}^2 + \frac{1}{4}\left\{ \text{Tr}[\Delta(\boldsymbol{k})\Delta^\dagger(\boldsymbol{k})] \pm \frac{\text{Tr}[M_-^{(1)}(\boldsymbol{k})\tilde{H}_0(\boldsymbol{k})]}{r\epsilon_{\boldsymbol{k}}^a + (1-r)\epsilon_{\boldsymbol{k}}^b} \right\}} \pm [r\epsilon_{\boldsymbol{k}}^a + (1-r)\epsilon_{\boldsymbol{k}}^b], \qquad (4.13)$$

where $\xi_{\boldsymbol{k}} \equiv \epsilon_{\boldsymbol{k}}^0 - \mu$. By using the transformation properties of the BdG Hamiltonian under space-inversion and time-reversal, we can confirm that Eq. (4.13) satisfies $E_{-\boldsymbol{k}}^+ \neq E_{\boldsymbol{k}}^\pm$ and $E_{-\boldsymbol{k}}^- \neq E_{\boldsymbol{k}}^\pm$ (i.e., the Bogoliubov spectrum is asymmetric) when $\text{Tr}[M_-^{(1)}(\boldsymbol{k})\tilde{H}_0(\boldsymbol{k})] \neq 0$ as follows. For $r = 1$, Eq. (4.13) leads to

$$E_{\boldsymbol{k}}^\pm = \sqrt{\xi_{\boldsymbol{k}}^2 + |\Delta_1 \eta_{\boldsymbol{k}}^b|^2 + |\Delta_2 \eta_{\boldsymbol{k}}^{ab}|^2 \pm 2\text{Im}(\Delta_1 \Delta_2^*)\eta_{\boldsymbol{k}}^b \eta_{\boldsymbol{k}}^{ab}} \pm \epsilon_{\boldsymbol{k}}^a. \qquad (4.14)$$

Then, we need to specify the $\boldsymbol{k}$-parity of $\epsilon_{\boldsymbol{k}}^a$, $\eta_{\boldsymbol{k}}^b$, and $\eta_{\boldsymbol{k}}^{ab}$, which depend on the details of the extra DOF, to investigate the property of the Bogoliubov spectrum $E_{-\boldsymbol{k}}^\pm$. We here denote $\epsilon_{-\boldsymbol{k}}^a = p_a \epsilon_{\boldsymbol{k}}^a$, $\eta_{-\boldsymbol{k}}^b = p_b \eta_{\boldsymbol{k}}^b$, and $\eta_{-\boldsymbol{k}}^{ab} = p_{ab}\eta_{\boldsymbol{k}}^{ab}$ ($p_a, p_b, p_{ab} = \pm 1$). From $\mathcal{P}$- and $\mathcal{T}$-symmetric behavior of $H_0(\boldsymbol{k})$ (see Eqs. (E.1) and (E.2)), we obtain $p_a\gamma_a = U_T^\dagger \gamma_a^* U_T = U_P^\dagger \gamma_a U_P$. On the other hand, the $\mathcal{P}, \mathcal{T}$-odd behavior of $M_-^{(1)}(\boldsymbol{k}) = 2\text{Im}(\Delta_1\Delta_2^*)\eta_{\boldsymbol{k}}^b \eta_{\boldsymbol{k}}^{ab}\gamma_a$ leads to $-p_b p_{ab}\gamma_a = U_T^\dagger \gamma_a^* U_T = U_P^\dagger \gamma_a U_P$. Thus, $p_a = -p_b p_{ab}$ holds in general. Using this relation, we obtain

$$E_{-\boldsymbol{k}}^\pm = \sqrt{\xi_{\boldsymbol{k}}^2 + |\Delta_1 \eta_{\boldsymbol{k}}^b|^2 + |\Delta_2 \eta_{\boldsymbol{k}}^{ab}|^2 \mp p_a 2\text{Im}(\Delta_1 \Delta_2^*)\eta_{\boldsymbol{k}}^b \eta_{\boldsymbol{k}}^{ab}} \pm p_a \epsilon_{\boldsymbol{k}}^a \quad (p_a = \pm 1). \qquad (4.15)$$

Comparing Eq. (4.15) with (4.14), we can safely say that $E_{-\boldsymbol{k}}^\pm \neq E_{\boldsymbol{k}}^+, E_{\boldsymbol{k}}^-$ and the Bogoliubov

spectrum is asymmetric. In the same manner, we can prove the asymmetry of Eq. (4.13) for $r = 0$. This result implies that $M_{-}^{(1)}(\boldsymbol{k}) \neq 0 \cap M_{-}^{(2)}(\boldsymbol{k}) \neq 0$ is indeed a necessary condition for emergence of the asymmetric Bogoliubov spectrum.

4.4   Anapole superconductivity

To obtain further insight into the asymmetric Bogoliubov spectrum, we now investigate the free energy of the above minimal model satisfying $M_{-}^{(1)}(\boldsymbol{k}) \neq 0 \cap M_{-}^{(2)}(\boldsymbol{k}) \neq 0$. By differentiating Eq. (4.13) with respect to Δ_j and Δ_j^* ($j = 1, 2$), the GL free energy for superconductivity is derived as follows (see Appendix G for the derivation):

$$
\begin{aligned}
\mathcal{F} = \ & \alpha_1 |\Delta_1|^2 + \alpha_2 |\Delta_2|^2 + \beta_1 |\Delta_1|^4 + \beta_2 |\Delta_2|^4 \\
& + 4\tilde{\beta} |\Delta_1|^2 |\Delta_2|^2 - \tilde{\beta}(\Delta_1^2 \Delta_2^{*2} + \Delta_2^2 \Delta_1^{*2}) \\
& + \sum_{\nu=x,y,z} (\kappa_{1,\nu} |\Delta_1|^2 + \kappa_{2,\nu} |\Delta_2|^2) q_\nu^2 + \boldsymbol{T} \cdot \boldsymbol{q},
\end{aligned}
\tag{4.16}
$$

where $\boldsymbol{q} = (q_x, q_y, q_z)$ is the center-of-mass momentum of Cooper pairs. The analytical expressions of α_j, $\beta_j (> 0)$, $\tilde{\beta} (> 0)$, and $\kappa_{j,\nu} (> 0)$ are shown in Appendix G. The last term is the Lifshitz invariant [215] stabilizing the FFLO state with $\boldsymbol{q} \parallel \boldsymbol{T}$. Since the Cooper pair condensation occurs at a single $\boldsymbol{q}$ in our model, the superconducting order parameter is expressed as $\Delta(\boldsymbol{r}) \propto e^{i\boldsymbol{q}\cdot\boldsymbol{r}}$ in real space (Fig. 4.1b). The coefficient vector $\boldsymbol{T} = (T_x, T_y, T_z)$ is given by

$$
\boldsymbol{T} = \rho_0 \langle \mathrm{Tr}[M_{-}^{(1)}(\boldsymbol{k})\tilde{H}_0(\boldsymbol{k})]\boldsymbol{v_k} \rangle_{\mathrm{FS}} \frac{7\zeta(3)}{16\pi^2 T^2},
\tag{4.17}
$$

where ρ_0 is the DOS at the Fermi energy, $\langle \cdots \rangle_{\mathrm{FS}}$ denotes the average over the Fermi surface, $\boldsymbol{v_k} \equiv \nabla_k \xi_k$, T is the temperature, and $\zeta(x)$ is the Riemann zeta function. $\boldsymbol{T}$ can be interpreted as the effective anapole moment of the superconducting state. To see this, we here consider conditions for $\boldsymbol{T} \neq \boldsymbol{0}$. Eq. (4.17) indicates that $\boldsymbol{T}$ is nonzero only for $\mathcal{P}$- and $\mathcal{T}$-symmetry breaking pairing states with $M_{-}^{(1)}(\boldsymbol{k}) \neq 0$. In addition, $\langle \mathrm{Tr}[M_{-}^{(1)}(\boldsymbol{k})\tilde{H}_0(\boldsymbol{k})]\boldsymbol{v_k} \rangle_{\mathrm{FS}}$ is nonzero only when the superconducting order parameter belongs to a polar IR, since the velocity $\boldsymbol{v_k}$ is a polar vector and $\tilde{H}_0(\boldsymbol{k})$ is assumed to be $\mathcal{P}$-symmetric. Therefore, $\boldsymbol{T}$ is a polar and time-reversal-odd vector; the symmetry is equivalent to the anapole moment [216, 217]. Hereafter, we refer to the superconductivity with $\boldsymbol{T} \neq \boldsymbol{0}$ as the *anapole superconductivity*. The anapole superconductivity realizes a nonuniform FFLO state with $\boldsymbol{q} \parallel \boldsymbol{T}$ (see Fig. 4.1b) to compensate a polar asymmetry in the Bogoliubov spectrum. The $\mathcal{PT}$-symmetric mixed-parity pairing is an origin of the anapole superconductivity. Although the stability of such pairing has been revealed [8], a self-consistent calculation is desirable to justify the stability of the anapole FFLO state and clarify the properties further. Such detailed analysis is left for future work.

Finally, we comment that the anapole moment must be aligned in the conducting direction
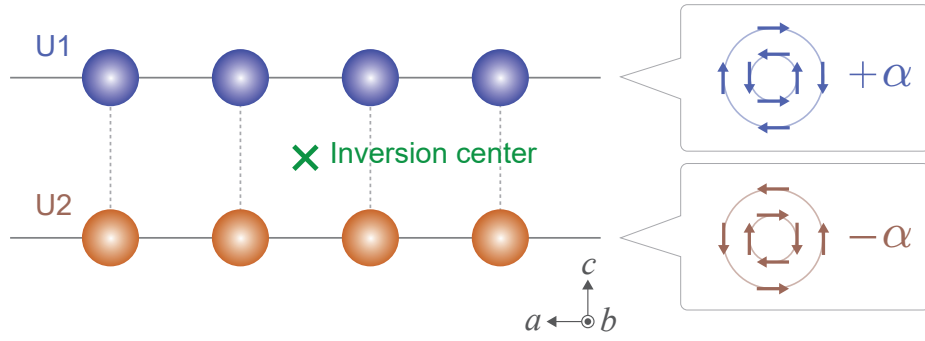
Fig. 4.2. Schematic of local $\mathcal{P}$-symmetry breaking in UTe$_2$. U atoms form a ladder structure along the a-axis. This locally NCS crystal structure leads to a sublattice-dependent staggered form of Rashba-type SOC.

in low-dimensional systems. This restriction naturally appears through the above expression (4.17) of the effective anapole moment $\boldsymbol{T}$.

4.5 Application to UTe$_2$

We now discuss the asymmetric Bogoliubov spectrum and anapole superconductivity in UTe$_2$. Intensive studies after the discovery of superconductivity evidenced odd-parity spin-triplet superconductivity in UTe$_2$ [134, 135, 227, 228, 237–249]. However, multiple superconducting phases similar to Fig. 4.1a have been observed under pressure [203–206, 223–226], and the antiferromagnetic quantum criticality implies the spin-singlet superconductivity there [225]. A theoretical study based on the periodic Anderson model verified this naive expectation and predicted the parity-mixed superconducting state in the intermediate pressure region [202]. Note that the interband pairing, which is an essential ingredient for the asymmetric Bogoliubov spectrum and anapole superconductivity, may have considerable impacts on the superconductivity in UTe$_2$ owing to multiple bands near the Fermi level [202, 250–256].

First, let us discuss the symmetry of superconductivity. Since the crystal structure of UTe$_2$ preserves D_{2h} point group symmetry, the superconducting order parameter is classified based on the IRs of D_{2h}. Below we consider all the odd-parity IRs, namely, A_u, B_{1u}, B_{2u}, and B_{3u}, although the A_u and B_{3u} IRs may be promising candidates [202, 247, 248, 250, 257]. Moreover, a recent calculation has shown that the even-parity A_g superconducting state is favored by antiferromagnetic fluctuation under pressure [202]. Therefore, we study a mixture of the even-parity A_g and odd-parity either A_u, B_{1u}, B_{2u}, or B_{3u} states, while we particularly focus on the A_u or B_{3u} pairing.

Table 4.1. Basis functions of $d_{\boldsymbol{k}}^{g,u}$ and corresponding $\boldsymbol{g}_{\boldsymbol{k}} \cdot (d_{\boldsymbol{k}}^{g} \times d_{\boldsymbol{k}}^{u})$ for possible $\mathcal{PT}$-symmetric mixed-parity pairing states in UTe$_2$. The last column shows the form of the effective anapole moment $\boldsymbol{T}$ for each pairing state.

Pairing	$d_{\boldsymbol{k}}^{g}$	$d_{\boldsymbol{k}}^{u}$	$\boldsymbol{g}_{\boldsymbol{k}} \cdot (d_{\boldsymbol{k}}^{g} \times d_{\boldsymbol{k}}^{u})$	$\boldsymbol{T}$
$A_g + iA_u$	$\phi_x^g k_y \hat{\boldsymbol{x}} + \phi_y^g k_x \hat{\boldsymbol{y}}$	$\phi_x^u k_x \hat{\boldsymbol{x}} + \phi_y^u k_y \hat{\boldsymbol{y}} + \phi_z^u k_z \hat{\boldsymbol{z}}$	$\alpha(\phi_x^g + \phi_y^g)\phi_z^u k_x k_y k_z$	$\boldsymbol{T} = \boldsymbol{0}$
$A_g + iB_{3u}$	$\phi_x^g k_y \hat{\boldsymbol{x}} + \phi_y^g k_x \hat{\boldsymbol{y}}$	$\phi_y^u k_z \hat{\boldsymbol{y}} + \phi_z^u k_y \hat{\boldsymbol{z}}$	$\alpha(\phi_x^g + \phi_y^g)\phi_z^u k_x k_y^2$	$\boldsymbol{T} \parallel \hat{\boldsymbol{x}}$
$A_g + iB_{2u}$	$\phi_x^g k_y \hat{\boldsymbol{x}} + \phi_y^g k_x \hat{\boldsymbol{y}}$	$\phi_x^u k_z \hat{\boldsymbol{x}} + \phi_z^u k_x \hat{\boldsymbol{z}}$	$\alpha(\phi_x^g + \phi_y^g)\phi_z^u k_x^2 k_y$	$\boldsymbol{T} \parallel \hat{\boldsymbol{y}}$
$A_g + iB_{1u}$	$\phi_x^g k_y \hat{\boldsymbol{x}} + \phi_y^g k_x \hat{\boldsymbol{y}}$	$\phi_x^u k_y \hat{\boldsymbol{x}} + \phi_y^u k_x \hat{\boldsymbol{y}} + \phi_z^u k_x k_y k_z \hat{\boldsymbol{z}}$	$\alpha(\phi_x^g + \phi_y^g)\phi_z^u k_x^2 k_y^2 k_z$	$\boldsymbol{T} \parallel \hat{\boldsymbol{z}}$

Based on the above facts, we introduce a minimal model for UTe$_2$ as follows:

$$H_0(\boldsymbol{k}) = (\varepsilon_{\boldsymbol{k}} - \mu)\sigma_0 \otimes \tau_0 + \boldsymbol{g}_{\boldsymbol{k}} \cdot \boldsymbol{\sigma} \otimes \tau_z, \tag{4.18}$$

$$\hat{\Delta}(\boldsymbol{k}) = \Delta_1(\psi_{\boldsymbol{k}}^g \sigma_0 \otimes \tau_0 + d_{\boldsymbol{k}}^g \cdot \boldsymbol{\sigma} \otimes \tau_z)$$
$$+ \Delta_2(d_{\boldsymbol{k}}^u \cdot \boldsymbol{\sigma} \otimes \tau_0 + \psi_{\boldsymbol{k}}^u \sigma_0 \otimes \tau_z), \tag{4.19}$$

where τ_ν represents the Pauli matrix for a sublattice DOF originating from a ladder structure of U atoms (Fig. 4.2). We assume a simple form of the single-particle kinetic energy as $\varepsilon_{\boldsymbol{k}} = -2\sum_{\nu=x,y,z} t_\nu \cos k_\nu$. The second term of Equation (4.18) is a sublattice-dependent staggered form of Rashba SOC with $\boldsymbol{g}_{\boldsymbol{k}} = \alpha(\sin k_y \hat{\boldsymbol{x}} - \sin k_x \hat{\boldsymbol{y}})$, which originates from the local $\mathcal{P}$-symmetry breaking at U sites [202, 258]. Since the local site symmetry descends to C_{2v} from D_{2h} owing to the ladder structure of U atoms, the existence of the Rashba-type SOC with opposite coupling constants $\pm\alpha$ at each sublattices is naturally expected (see Fig. 4.2). The local $\mathcal{P}$-symmetry breaking also leads to a sublattice-dependent parity mixing of the pair potential [31]. Then, the even-parity (odd-parity) pair potential is assumed to be a mixture of intrasublattice spin-singlet (spin-triplet) and staggered spin-triplet (spin-singlet) components as shown in Eq. (4.19). We assume the form of the $\boldsymbol{k}$-dependent coefficients $\psi_{\boldsymbol{k}}^g$ and $d_{\boldsymbol{k}}^g$ ($d_{\boldsymbol{k}}^u$ and $\psi_{\boldsymbol{k}}^u$) so as to be consistent with the basis functions of the A_g IR (A_u, B_{1u}, B_{2u}, or B_{3u} IRs).

We now consider the necessary conditions for an asymmetric Bogoliubov spectrum in UTe$_2$. As discussed in the above sections, a nonzero $\text{Tr}[M_-^{(1)}(\boldsymbol{k})\tilde{H}_0(\boldsymbol{k})]$ is necessary for the asymmetric Bogoliubov spectrum in a two-band model. For Eqs. (4.18) and (4.19), this quantity is obtained as $\text{Tr}[M_-^{(1)}(\boldsymbol{k})\tilde{H}_0(\boldsymbol{k})] = -8\text{Im}(\Delta_1\Delta_2^*)[\boldsymbol{g}_{\boldsymbol{k}} \cdot (d_{\boldsymbol{k}}^g \times d_{\boldsymbol{k}}^u)]$. Therefore, $\boldsymbol{g}_{\boldsymbol{k}} \cdot (d_{\boldsymbol{k}}^g \times d_{\boldsymbol{k}}^u) \neq 0$ must be satisfied to realize the asymmetric Bogoliubov spectrum. This indicates that the sublattice-dependent SOC and spin-triplet pairing components $d_{\boldsymbol{k}}^{g,u}$ are essential for the appearance of the asymmetric Bogoliubov spectrum. On the other hand, the spin-singlet pairing components $\psi_{\boldsymbol{k}}^{g,u}$ do not play an important role for realizing the asymmetric Bogoliubov spectrum in this model. Hereafter, we assume $\psi_{\boldsymbol{k}}^g = 1$ and $\psi_{\boldsymbol{k}}^u = 0$ for simplicity. The basis functions of $d_{\boldsymbol{k}}^{g,u}$ and corresponding $\boldsymbol{g}_{\boldsymbol{k}} \cdot (d_{\boldsymbol{k}}^g \times d_{\boldsymbol{k}}^u)$ for possible mixed-parity superconducting states in UTe$_2$ are

summarized in Table 4.1. As shown in Table 4.1, $g_k \cdot (d_k^g \times d_k^u) \propto \alpha(\phi_x^g + \phi_y^g)\phi_z^u$ for all patterns of the superconducting state, where $\phi_\nu^{g,u}$ is a real-valued coefficient of the ν-th component of $d_k^{g,u}$. Therefore, $\phi_x^g + \phi_y^g \neq 0$ and $\phi_z^u \neq 0$ are necessary for the asymmetric Bogoliubov spectrum. According to a recent numerical calculation in Ref. [202], the magnetic anisotropy of UTe$_2$ leads to $|\phi_y^g| \gg |\phi_x^g|$ for the A_g state. Then, we assume $d_k^g = \sin k_x \hat{y}$ (i.e., $\phi_x^g = 0$ and $\phi_y^g = 1$) in the following calculations. On the other hand, we assume $\phi_\nu^u = \delta_{\nu z}$ for the odd-parity pairing component to extract only the essential ingredient for the asymmetric Bogoliubov spectrum and make a clear discussion.

The numerical results of the Bogoliubov spectrum for this UTe$_2$ model are shown in Fig. 4.3. We here consider only the $A_g + iA_u$ and $A_g + iB_{3u}$ states as promising candidates of the $\mathcal{PT}$-symmetric mixed-parity superconductivity in UTe$_2$. It is shown that the Bogoliubov spectrum of both $A_g + iA_u$ and $A_g + iB_{3u}$ states are indeed asymmetric along some directions in the Brillouin zone (see Figs. 4.3a and 4.3c). The Bogoliubov spectrum in the $A_g + iA_u$ state exhibits a $k_x k_y k_z$-type tetrahedral asymmetry as depicted in Fig. 4.3b, while the Bogoliubov spectrum in the $A_g + iB_{3u}$ state shows a $k_x k_y^2$-type unidirectional asymmetry as depicted in Fig. 4.3d. Consistent with these numerical results, Table 4.1 reveals that $g_k \cdot (d_k^g \times d_k^u)$ of the $A_g + iA_u$ and $A_g + iB_{3u}$ states are proportional to $k_x k_y k_z$ and $k_x k_y^2$, respectively. This implies that the type of asymmetry in the Bogoliubov spectrum is determined by the symmetry of $\text{Tr}[M_-^{(1)}(k)\tilde{H}_0(k)]$, which is an essential ingredient for realizing the asymmetric Bogoliubov spectrum.

Finally, we discuss the possible anapole superconductivity in UTe$_2$. The $A_g + iA_u$ state belongs to the nonpolar A_u^- IR (IRs with odd time-reversal parity are denoted by Γ^-), which corresponds to nonpolar odd-parity magnetic multipoles such as magnetic monopole, quadrupole, and hexadecapole from the viewpoint of symmetry. On the other hand, the $A_g + iB_{3u}$ state belongs to the polar B_{3u}^- IR with the polar x-axis, which is symmetrically equivalent to the anapole moment T_x. Since the anapole superconducting states are allowed only when the superconducting order parameter belongs to a polar IR, the $A_g + iB_{3u}$ state is a possible candidate of the anapole superconductivity. Indeed, as discussed above, the Bogoliubov spectrum of the $A_g + iB_{3u}$ state exhibits a polar $k_x k_y^2$-type asymmetry, while the Bogoliubov spectrum of the $A_g + iA_u$ state exhibits a nonpolar $k_x k_y k_z$-type asymmetry (see Fig. 4.3). It should also be noted that the Bogoliubov spectrum in the $A_g + iB_{3u}$ state possesses the polarity along the k_x-axis, which coincides with the polar axis of the B_{3u}^- IR.

Based on the above classification and the GL free energy (4.16), the anapole FFLO state with $q \propto T \parallel \hat{x}$ should be naturally realized in the $A_g + iB_{3u}$ state. In the same manner, we expect the realization of anapole superconducting states with $T \parallel \hat{y}$ and $T \parallel \hat{z}$ in the $A_g + iB_{2u}$ and $A_g + iB_{1u}$ states, respectively. See Appendix H for a comprehensive symmetry analysis for possible anapole superconductivity in UTe$_2$.
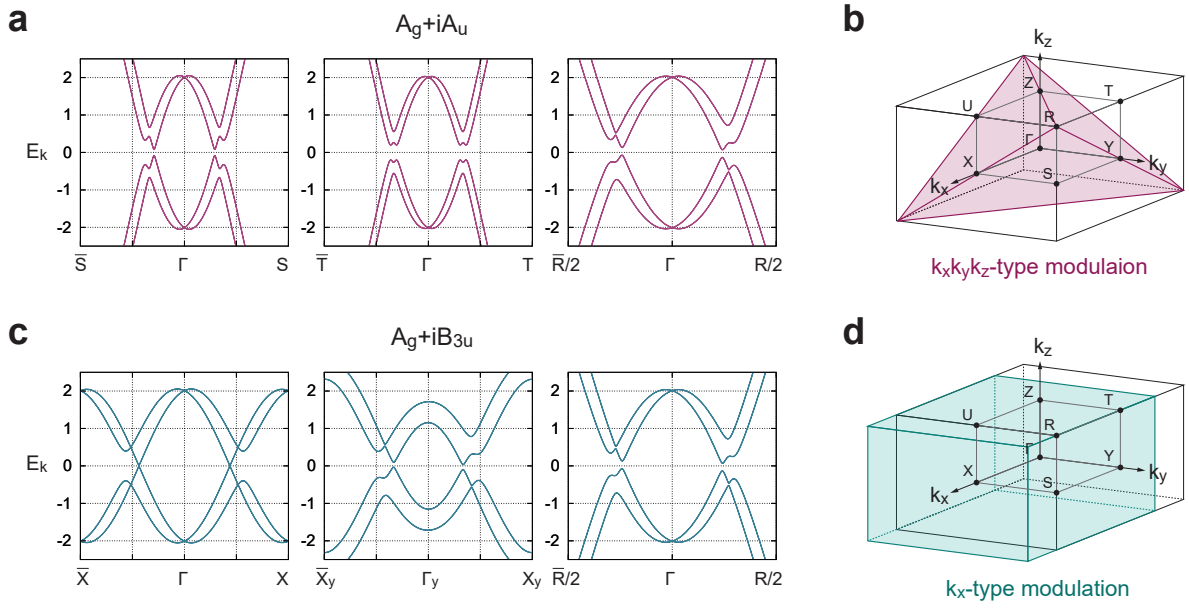
Fig. 4.3. Asymmetric Bogoliubov spectrum for the UTe$_2$ model. (a) Bogoliubov spectrum in the $A_g + iA_u$ state with $(\Delta_1, \Delta_2) = (0.2, 0.2i)$ and $\boldsymbol{d}_{\boldsymbol{k}}^u = \sin k_z \hat{\boldsymbol{z}}$. (b) Schematic of $k_x k_y k_z$-type asymmetric modulation in the Brillouin zone. (c) Bogoliubov spectrum in the $A_g + iB_{3u}$ state with $(\Delta_1, \Delta_2) = (0.2, 0.2i)$ and $\boldsymbol{d}_{\boldsymbol{k}}^u = \sin k_y \hat{\boldsymbol{z}}$. (d) Schematic of k_x-type asymmetric modulation. The symbols of the horizontal axis in (a) and (c) denote the $\boldsymbol{k}$-points in the Brillouin zone of a primitive orthorhombic lattice; $\Gamma = (0, 0, 0)$, X $= -\bar{\text{X}} = (\pi, 0, 0)$, S $= -\bar{\text{S}} = (\pi, \pi, 0)$, T $= -\bar{\text{T}} = (0, \pi, \pi)$, R $= -\bar{\text{R}} = (\pi, \pi, \pi)$, $\Gamma_y = (0, \pi/4, 0)$, and X$_y = -\bar{\text{X}}_y = (\pi, \pi/4, 0)$. In the numerical calculations, parameters are set to be $t_\nu = 1.0$, $\mu = -4.0$, and $\alpha = 0.4$. The asymmetric Bogoliubov spectrum appears in (a) and (c) consistent with the symmetry analysis of $\text{Tr}[M_{-}^{(1)}(\boldsymbol{k})\tilde{H}_0(\boldsymbol{k})] \propto \boldsymbol{g_k} \cdot (\boldsymbol{d}_{\boldsymbol{k}}^g \times \boldsymbol{d}_{\boldsymbol{k}}^u)$.

4.6 Discussion and summary

From the analogy with magnetic states, we can predict various exotic superconducting phenomena closely related to the asymmetric Bogoliubov spectrum. For instance, the asymmetry of the Bogoliubov spectrum will significantly affect the superconducting piezoelectric effect [236], nonreciprocal optical responses [259], and nonreciprocal Meissner effect [260]. All of these phenomena are caused by the absence of $\mathcal{P}$- and $\mathcal{T}$-symmetries in the superconducting state. Hence, they will be useful probes to offer conclusive evidence for the $\mathcal{P}, \mathcal{T}$-symmetry breaking and the Bogoliubov spectrum asymmetry in superconductors. Studies for the interplay of these exotic superconducting phenomena and asymmetric Bogoliubov spectrum will be presented elsewhere.

Experimental detection of the anapole superconductivity should be possible by observing its domain structure. The anapole superconducting state effectively carries a supercurrent along the anapole moment $\boldsymbol{T}$, since the order parameter is spatially modulated with $e^{i\boldsymbol{q}\cdot\boldsymbol{r}} \sim e^{i\boldsymbol{T}\cdot\boldsymbol{r}}$. This indicates the emergence of superconducting vortices at the anapole domain boundaries (see Fig. 4.4a) even though an external magnetic field is absent. The anapole domains can be generally formed owing to the degeneracy between the $\Gamma_g + i\Gamma_u$ pairing and $\Gamma_g - i\Gamma_u$ pairing states, which have the opposite anapole moment. Therefore, the observation of vortices at a zero magnetic field can be solid evidence of the anapole superconductivity. In addition, the anapole domain can be switched by the supercurrent in a similar way to the electrical switching of antiferromagnets [261, 262]. In an anapole superconductor, the effective anapole moment $\boldsymbol{T}$ couples to the applied electric current $\boldsymbol{j}$, which is a symmetry-adapted field of the anapole moment. Then, the anapole superconducting domain should be switched to align the effective anapole moments along the injected supercurrent $\boldsymbol{j}$ (see Fig. 4.4b). It should also be noticed that the anapole domain switching eliminates the internal magnetic field from the vortices at the domain boundaries, since the domain structure disappears by applying the supercurrent. Therefore, the anapole superconducting domain switching can be regarded as a process of erasing magnetic information. These properties indicate potential applications of anapole superconductivity as a novel quantum device for magnetic information storage and processing.

In summary, we have established that the $\mathcal{PT}$-symmetric mixed-parity superconducting states generally possess asymmetry in the energy spectrum of the Bogoliubov quasiparticles. We have clarified that the asymmetric Bogoliubov spectrum can be induced by $\mathcal{P}, \mathcal{T}$-odd nonunitary part of the bilinear product $\Delta\Delta^{\dagger}$ that originates from the interband pairing. This means that the multiband effects on superconductivity, which have not been taken into account in the previous works, are essential for realizing the asymmetric Bogoliubov spectrum. Based on the above insights, we have explicitly derived the necessary conditions for the emergence of asymmetric Bogoliubov spectrum in $\mathcal{PT}$-symmetric superconductors. Especially, we have shown that an
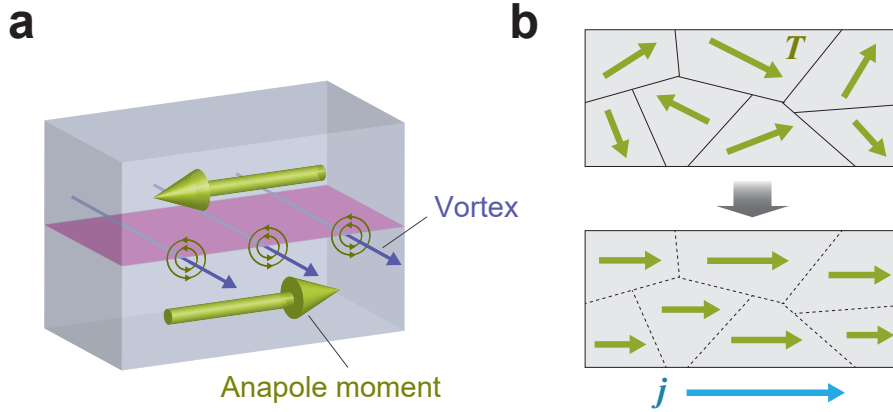
Fig. 4.4. Anapole domain and domain switching through supercurrent. (a) Vortices at the boundary of anapole superconducting domains. (b) The proposed domain switching in anapole superconductors. The effective anapole moment T is aligned along the injected supercurrent j.

FFLO-like state, which we call anapole superconducting state, is stabilized in the absence of an external magnetic field when the superconducting state belongs to a polar and time-reversal-odd IR. The stabilization of the anapole superconducting state is evidenced by the emergence of Lifshitz invariants in the GL free energy due to the effective anapole moment. The physics of asymmetric Bogoliubov spectrum appears in any multiband superconductors when even- and odd-parity pairing interactions are comparable in strength. As a specific example, we considered the mixed-parity pairing states in UTe_2, which is caused by an accidental competition of ferromagnetic and antiferromagnetic spin fluctuations under pressure [202]. We have shown that the mixed-parity superconductivity in UTe_2 can realize the asymmetric Bogoliubov spectrum and anapole superconductivity owing to the sublattice-dependent staggered antisymmetric SOC and locally parity-mixed Cooper pairing, which originates from the locally NCS ladder structure of U atoms. The asymmetric Bogoliubov spectrum may be linked to the asymmetric spectrum in the STM measurement [227], although it was interpreted based on the chiral superconductivity. The vortex structure near the anapole domain boundary (Fig. 4.4a) may also cause the polar Kerr effect, reported for UTe_2 [230]. Spontaneous ordering of strongly parity-mixed pairing state and resulting asymmetric Bogoliubov spectrum can also be expected in superconductivity mediated by parity-breaking fluctuations [48]. To further broaden the scope of application of our theory, it is important to find microscopic electronic interactions that induce competing even- and odd-parity pairing instabilities.

We predicted various superconducting phenomena induced by the asymmetric Bogoliubov spectrum, such as the superconducting piezoelectric effect, nonlinear optical responses, non-reciprocal Meissner effect, and anapole domain switching from the analogy with magnetic materials. Topological properties and collective modes associated with the asymmetric Bogoliubov spectrum may also be intriguing issues. Exploration of such exotic phenomena will be a

promising route for future research.

Chapter 5

Summary

In this thesis, we have investigated various exotic superconductivity associated with parity-symmetry breaking.

In Chap. 2, we have studied the interplay of superconductivity, ferroelectricity, and multiorbital/multiband effects by analyzing a three-orbital model for STO. We have clarified two distinct stabilization mechanisms for the FESC that rely on the presence of SOC. First, we demonstrated that the ferroelectricity-induced Lifshitz transition stabilizes the FESC in a very low carrier density regime. This result is in good agreement with the experimental result of FESC in STO. Second, we showed that the Rashba-type spin-momentum locking in the ferroelectric ordered state triggers the stabilization of FESC under magnetic fields, which is independent of the carrier density. Interestingly, the stability of the FESC based on the above two mechanisms is enhanced by the multiorbital/multiband effects in STO. Furthermore, we found exotic superconducting phenomena induced by the coexistent ferroelectric order. Under a high magnetic field, the FESC realizes a topological Weyl superconducting state in a low carrier density regime. On the other hand, at zero magnetic fields, the ferroelectric superconducting state hosts the multiorbital odd-frequency pair correlations.

In Chap. 3, exotic correlations between FM-fluctuation-mediated odd-parity superconductivity and locally NCS crystal structure have been elucidated in a two-dimensional bilayer triangular lattice Hubbard model. By analyzing this model within the RPA, we demonstrated the dominance of the FM spin fluctuations in a broad range of parameter regimes, which is caused by the disconnected Fermi surface structure and underlying type-II vHS. In addition, by performing the numerical calculations of the linearized Eliashberg equation, we showed that the odd-parity spin-triplet f-wave superconductivity is stabilized by the FM fluctuations. Then, we investigated the impacts of the layer-dependent staggered antisymmetric SOC on spin fluctuations and superconductivity. We clarified that the multiple superconducting transitions between distinct odd-parity pairing states including topologically nontrivial superconducting states are induced by tuning the antisymmetric SOC. The appearance of the multiple odd-parity superconducting instabilities is explained by the delicate balance between the selection rule for

locally NCS superconductors, anisotropy of the magnetic susceptibility, and local parity-mixing effect of superconductivity. Based on the obtained results, we have discussed the possibility of odd-parity superconductivity in bilayer TMDs and van der Waals ferromagnets.

In Chap. 4, we have studied the spontaneously ordered $\mathcal{PT}$-symmetric mixed-parity superconductivity in multiband systems. By analyzing a generic two-band model, we have demonstrated that the $\mathcal{PT}$-symmetric mixed-parity multiband superconductors generally exhibit unusual asymmetry in the Bogoliubov spectrum. From the analogy with parity-breaking magnetic materials, the asymmetric Bogoliubov spectrum is expected to host various nonequilibrium superconducting phenomena. The essential ingredient for the asymmetric Bogoliubov spectrum is the $\mathcal{P}$- and $\mathcal{T}$-symmetry breaking nonunitary component of the gap function arising from the interband pairing. Therefore, the multiband nature of superconductivity is essential. Furthermore, by analyzing the free energy, we also demonstrated that the asymmetric Bogoliubov spectrum leads to the stabilization of an FFLO-like nonuniform state, namely anapole superconducting state, at zero magnetic fields. The anapole superconductivity is caused by an effective anapole moment of the pairing state, which appears only when the superconducting order parameter belongs to a polar IR and the Bogoliubov spectrum possesses a polar asymmetry. Based on the obtained results, we discussed the possibility of asymmetric Bogoliubov spectrum and anapole superconductivity in UTe$_2$ owing to the locally NCS crystal structure. Finally, we proposed the experimental detection of anapole superconductivity through the observation of vortices at the anapole domain boundary.

We have uncovered the novel interplay of superconductivity and parity symmetry breaking from fresh viewpoints. Since some of the obtained results are based on simplified assumptions or methods, one of the important future issues is further developing the theories presented in this thesis. On the other hand, at present, there are not so many candidate materials to experimentally verify our theoretical findings. Therefore, searching for new candidate materials and establishing new experimental methods are essential for the future development of this research field.

Appendix A

Effective Rashba spin-orbit coupling

In the Appendix, we clarify the origin of the unconventional Rashba SOC in STO (Sec. 2.4) by deriving the effective Hamiltonian from two approaches.

A.1   Perturbation analysis for LS coupling

First, we carry out the perturbation analysis for the LS coupling λ and the odd-parity hybridization γ. This analysis is valid when λ is much smaller than other energy scales such as the band-width. As a result of the first-order perturbation expansion for λ, we obtain a new $\boldsymbol{k}$-dependent basis as follows:

$$|d_{yz}, \sigma\rangle_{\boldsymbol{k},\lambda} = |d_{yz}, \sigma\rangle + \frac{\lambda \mathcal{S}_\sigma}{2} \left(\frac{|d_{xy}, \overline{\sigma}\rangle}{\delta_{3,1}(\boldsymbol{k})} + \frac{i\,|d_{xz}, \sigma\rangle}{\delta_{2,1}(\boldsymbol{k})} \right), \tag{A.1}$$

$$|d_{xz}, \sigma\rangle_{\boldsymbol{k},\lambda} = |d_{zx}, \sigma\rangle + \frac{\lambda}{2} \left(\frac{i\,|d_{xy}, \overline{\sigma}\rangle}{\delta_{3,2}(\boldsymbol{k})} + \frac{i\mathcal{S}_\sigma\,|d_{yz}, \sigma\rangle}{\delta_{2,1}(\boldsymbol{k})} \right), \tag{A.2}$$

$$|d_{xy}, \sigma\rangle_{\boldsymbol{k},\lambda} = |d_{xy}, \sigma\rangle + \frac{\lambda}{2} \left(\frac{\mathcal{S}_\sigma\,|d_{yz}, \overline{\sigma}\rangle}{\delta_{3,1}(\boldsymbol{k})} + \frac{i\,|d_{xz}, \overline{\sigma}\rangle}{\delta_{3,2}(\boldsymbol{k})} \right), \tag{A.3}$$

where $|t_{2g}, \sigma\rangle$ ($t_{2g} = d_{yz}, d_{xz}, d_{xy}$, $\sigma = \uparrow, \downarrow$) is the wave function of the local t_{2g} orbitals, $\delta_{l,l'}(\boldsymbol{k}) \equiv \varepsilon_l(\boldsymbol{k}) - \varepsilon_{l'}(\boldsymbol{k})$, and $\mathcal{S}_\sigma = \pm 1$ for $\sigma = \uparrow, \downarrow$. Then, we carry out the $\boldsymbol{k}$-dependent basis transformation for $\mathcal{H}_0 + \mathcal{H}_{\mathrm{pol}}$ from the local t_{2g} orbital space $|t_{2g}, \sigma\rangle$ to the renormalized t_{2g} orbital space $|t_{2g}, \sigma\rangle_{\boldsymbol{k},\lambda}$. In addition, we perform a block diagonalization for up and down pseudospin sectors to derive the effective SOC. Finally, we neglect the interorbital component since the orbital hybridizations by λ and γ are assumed to be small. Thus, in the case of a weak

spin-orbit coupling, the effective Hamiltonian is described as

$$\tilde{\mathcal{H}}_0^L = \sum_{\boldsymbol{k},\alpha,\sigma} \left(\varepsilon_\alpha^L(\boldsymbol{k}) - \mu\right) c_{\boldsymbol{k},\alpha\sigma}^\dagger c_{\boldsymbol{k},\alpha\sigma}$$
$$+ \sum_{\boldsymbol{k},\alpha,\sigma,\sigma'} \boldsymbol{g}_\alpha^L(\boldsymbol{k}) \cdot \boldsymbol{\sigma}_{\sigma\sigma'} c_{\boldsymbol{k},\alpha\sigma}^\dagger c_{\boldsymbol{k},\alpha\sigma'}, \tag{A.4}$$

where the lower, middle, and upper bands are denoted by the band index $\alpha = 1, 2, 3$. The renormalized single-particle energy $\varepsilon_\alpha^L(\boldsymbol{k})$ are described as

$$\varepsilon_1^L(\boldsymbol{k}) = \frac{1}{2}\left(\varepsilon_1(\boldsymbol{k}) + \varepsilon_2(\boldsymbol{k}) - |\delta_{2,1}(\boldsymbol{k})|\right), \tag{A.5}$$

$$\varepsilon_2^L(\boldsymbol{k}) = \frac{1}{2}\left(\varepsilon_1(\boldsymbol{k}) + \varepsilon_2(\boldsymbol{k}) + |\delta_{2,1}(\boldsymbol{k})|\right), \tag{A.6}$$

$$\varepsilon_3^L(\boldsymbol{k}) = \varepsilon_3(\boldsymbol{k}), \tag{A.7}$$

and the effective g-vector $\boldsymbol{g}_\alpha^L(\boldsymbol{k})$ are obtained as

$$\boldsymbol{g}_1^L(\boldsymbol{k}) = 2\lambda\gamma \begin{pmatrix} \sin k_y \left(\dfrac{1 - \text{sgn}[\delta_{2,1}(\boldsymbol{k})]}{\delta_{3,2}(\boldsymbol{k})}\right) \\ -\sin k_x \left(\dfrac{1 + \text{sgn}[\delta_{2,1}(\boldsymbol{k})]}{\delta_{3,1}(\boldsymbol{k})}\right) \\ 0 \end{pmatrix}, \tag{A.8}$$

$$\boldsymbol{g}_2^L(\boldsymbol{k}) = 2\lambda\gamma \begin{pmatrix} \sin k_y \left(\dfrac{1 + \text{sgn}[\delta_{2,1}(\boldsymbol{k})]}{\delta_{3,2}(\boldsymbol{k})}\right) \\ -\sin k_x \left(\dfrac{1 - \text{sgn}[\delta_{2,1}(\boldsymbol{k})]}{\delta_{3,1}(\boldsymbol{k})}\right) \\ 0 \end{pmatrix}, \tag{A.9}$$

$$\boldsymbol{g}_3^L(\boldsymbol{k}) = -2\lambda\gamma \begin{pmatrix} \sin k_y \left(\dfrac{1}{\delta_{3,2}(\boldsymbol{k})}\right) \\ -\sin k_x \left(\dfrac{1}{\delta_{3,1}(\boldsymbol{k})}\right) \\ 0 \end{pmatrix}. \tag{A.10}$$

Figure A.1 shows the $\boldsymbol{k}$-dependence of the effective g-vector $\boldsymbol{g}_\alpha^L(\boldsymbol{k})$ for each Rashba split bands at $k_z = 0$. We see that the unconventional Rashba spin-orbit splitting in the bulk STO [Fig. 2.4] is well reproduced by the above perturbation analysis.

According to Eqs. (A.8), (A.9), and (A.10), the multiorbital effect is reflected in the SOC
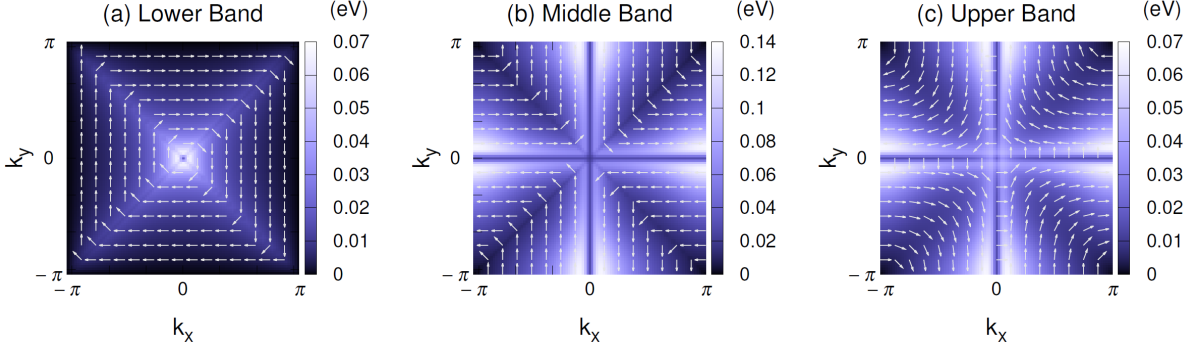
Fig. A.1. The magnitude of the spin-orbit splitting, which is derived by the perturbation analysis for λ and γ, in the (a) lower band, (b) middle band, and (c) upper band at $k_z = 0$. The odd-parity hopping integral is set to $\gamma/t_1 = 0.105$. The arrows show the direction of the effective g-vector $\boldsymbol{g}_\alpha^L(\boldsymbol{k})$.

through the energy difference $\delta_{ll'}(\boldsymbol{k})$ in two ways. One is the denominators, i.e., $\delta_{3,1}(\boldsymbol{k})$ and $\delta_{3,2}(\boldsymbol{k})$, and the other is the numerator, i.e., $1 \pm \text{sgn}[\delta_{2,1}(\boldsymbol{k})]$. The origin of the unconventional Rashba splitting in the upper band $\delta\mathcal{E}_3(\boldsymbol{k})$ is explained by the former multiorbital effect in the denominator of Eq. (A.10) [100]. The magnitude of $\delta\mathcal{E}_3(\boldsymbol{k})$ is small on the line $\boldsymbol{k} \parallel [100]$ [Fig. A.1(c)] since $\delta_{3,1}(\boldsymbol{k})$ is large and the y component of the g-vector $\boldsymbol{g}_3^L(\boldsymbol{k})$ is small. On the other hand, a large x component of $\boldsymbol{g}_3^L(\boldsymbol{k})$ appears upon moving slightly away from the Γ-X line because of the small value of its denominator $\delta_{3,2}(\boldsymbol{k})$. Thus, the spin-orbit splitting in the upper band is large at $\boldsymbol{k}$ slightly away from the Γ-X line as shown in Figs. 2.4(a) and A.1(c).

The unconventional Rashba splitting in the lower and middle bands are explained by the combination of two multiorbital effects represented by the denominator and numerator of Eqs. (A.8) and (A.9). Since the denominators of Eqs. (A.8) and (A.9) are the same as those of Eq. (A.10), the Rashba splitting different from that of the upper band originates from the numerator $1 \pm \text{sgn}[\delta_{2,1}(\boldsymbol{k})]$. The $\boldsymbol{k}$-dependence of $1 \pm \text{sgn}[\delta_{2,1}(\boldsymbol{k})]$ at $k_z = 0$ is described as follows:

$$\eta_\pm(k_x, k_y) \equiv 1 \pm \text{sgn}[\delta_{2,1}(k_x, k_y, k_z = 0)]$$

$$= \begin{cases} 0 & (|k_x| \lessgtr |k_y|) \\ 1 & (|k_x| = |k_y|) \\ 2 & (|k_x| \gtrless |k_y|) \end{cases} . \tag{A.11}$$

Since $\eta_-(k_x, k_y) = 0$ ($\eta_+(k_x, k_y) = 0$) in $|k_x| > |k_y|$ ($|k_x| < |k_y|$), the x (y) component of $\boldsymbol{g}_1^L(\boldsymbol{k})$ becomes zero. Thus, $\boldsymbol{g}_1^L(\boldsymbol{k})$ is parallel to the [100] or [010] axis in the most region of Brillouin zone, and rapidly rotates by $\pi/2$ when going across the line $|k_x| = |k_y|$ as shown in Figs. 2.4(c) and A.1(a). Figure A.1(a) also shows that the spin-orbit splitting is maximized near the Γ-point, and rapidly decreases by increasing the distance from the Γ-point. From similar discussions we understand that $\boldsymbol{g}_2^L(\boldsymbol{k})$ is perpendicular to $\boldsymbol{g}_1^L(\boldsymbol{k})$ except for the line $|k_x| = |k_y|$. Consequently,

the Rashba splitting in the middle band becomes similar to that of the upper band, except the rapid $\pi/2$-rotation of the g-vector at $|k_x| = |k_y|$ [Figs. 2.4(b) and A.1(b)].

A.2 Total angular momentum description

Although the above perturbation analysis for the LS coupling reproduces many features of unconventional Rashba spin-orbit splitting in STO, it is not valid in the vicinity of the Γ-point. In particular, the disappearance of the spin-orbit splitting in the lower band near the Γ-point [Fig. 2.4(c)] is not reproduced by the perturbation analysis [Fig. A.1(a)]. This is because the wave function is appropriately labeled by the total angular momentum $J = L + S$ and the perturbation analysis breaks down. Therefore, it is desirable to derive the effective SOC in the total angular momentum description. Generally speaking, the following analysis is valid for the strong spin-orbit coupling compared to other energy scales such as the band-width. Actually, we will see that it is valid only near the Γ-point.

In the t_{2g} orbital subspace, the orbital angular momentum can be treated as $L = 1$. Thus, the total angular momentum $J = 3/2$ or $J = 1/2$ are obtained as a composition of the angular momentum $L = 1$ and $S = 1/2$. The basis wave functions in the total angular momentum space $|J, M\rangle$ are obtained as follows:

$$|\frac{3}{2}, \frac{3}{2}\rangle = -\frac{1}{\sqrt{2}}\left(|d_{yz}, \uparrow\rangle + i\,|d_{xz}, \uparrow\rangle\right), \tag{A.12}$$

$$|\frac{3}{2}, \frac{1}{2}\rangle = \frac{1}{\sqrt{6}}\left(2\,|d_{xy}, \uparrow\rangle - |d_{yz}, \downarrow\rangle - i\,|d_{xz}, \downarrow\rangle\right), \tag{A.13}$$
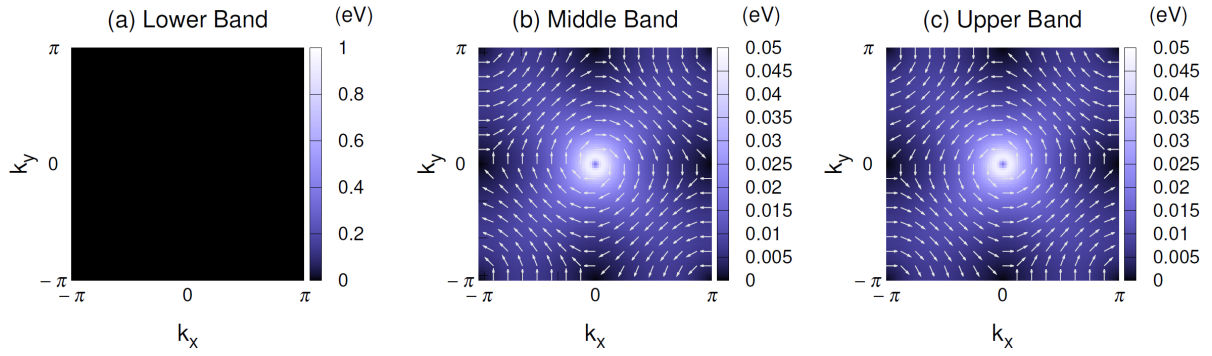
$$|\frac{3}{2}, -\frac{1}{2}\rangle = \frac{1}{\sqrt{6}}\left(|d_{yz}, \uparrow\rangle - i\,|d_{xz}, \uparrow\rangle + 2\,|d_{xy}, \downarrow\rangle\right), \tag{A.14}$$

$$|\frac{3}{2}, -\frac{3}{2}\rangle = \frac{1}{\sqrt{2}}\left(|d_{yz}, \downarrow\rangle - i\,|d_{xz}, \downarrow\rangle\right), \tag{A.15}$$

$$|\frac{1}{2}, \frac{1}{2}\rangle = \frac{1}{\sqrt{3}}\left(|d_{xy}, \uparrow\rangle + |d_{yz}, \downarrow\rangle + i\,|d_{xz}, \downarrow\rangle\right), \tag{A.16}$$

$$|\frac{1}{2}, -\frac{1}{2}\rangle = \frac{1}{\sqrt{3}}\left(|d_{yz}, \uparrow\rangle - i\,|d_{xz}, \uparrow\rangle - |d_{xy}, \downarrow\rangle\right), \tag{A.17}$$

where $M = \pm 3/2, \pm 1/2$ is the total magnetic quantum number. Then, we carry out the $\boldsymbol{k}$-independent basis transformation for $\mathcal{H}_0 + \mathcal{H}_{\mathrm{pol}}$ from the local t_{2g} orbital space $|t_{2g}, \sigma\rangle$ to the total angular momentum space $|J, M\rangle$. From the procedure similar to the previous subsection,

Fig. A.2. The magnitude of the spin-orbit splitting, which is derived by the basis transformation to the total angular momentum space, in the (a) lower band, (b) middle band, and (c) upper band at $k_z = 0$. The odd-parity hopping integral is set to $\gamma/t_1 = 0.105$. The arrows show the direction of the effective g-vector $\boldsymbol{g}_\alpha^J(\boldsymbol{k})$.

the effective Hamiltonian is derived as

$$\tilde{\mathcal{H}}_0^J = \sum_{\boldsymbol{k},\alpha,\sigma} \left(\varepsilon_\alpha^J(\boldsymbol{k}) - \mu\right) c_{\boldsymbol{k},\alpha\sigma}^\dagger c_{\boldsymbol{k},\alpha\sigma}$$
$$+ \sum_{\boldsymbol{k},\alpha,\sigma,\sigma'} \boldsymbol{g}_\alpha^J(\boldsymbol{k}) \cdot \boldsymbol{\sigma}_{\sigma\sigma'} c_{\boldsymbol{k},\alpha\sigma}^\dagger c_{\boldsymbol{k},\alpha\sigma'}. \tag{A.18}$$

Here, the renormalized energy dispersion $\varepsilon_\alpha^J(\boldsymbol{k})$ are obtained as follows:

$$\varepsilon_1^J(\boldsymbol{k}) = \frac{1}{2}\left(\varepsilon_1(\boldsymbol{k}) + \varepsilon_2(\boldsymbol{k}) - \lambda\right), \tag{A.19}$$

$$\varepsilon_2^J(\boldsymbol{k}) = \frac{1}{4}\left(\sum_l \varepsilon_l(\boldsymbol{k}) + \lambda\right) - \sqrt{f^J(\boldsymbol{k})}, \tag{A.20}$$

$$\varepsilon_3^J(\boldsymbol{k}) = \frac{1}{4}\left(\sum_l \varepsilon_l(\boldsymbol{k}) + \lambda\right) + \sqrt{f^J(\boldsymbol{k})}, \tag{A.21}$$

where

$$f^J(\boldsymbol{k}) = 2\gamma^2\left(\sin^2 k_y + \sin^2 k_x\right) + \left(\frac{\delta_{3,1}(\boldsymbol{k}) + \delta_{3,2}(\boldsymbol{k}) - \lambda}{4}\right)^2. \tag{A.22}$$

The effective g-vector $\boldsymbol{g}_\alpha^J(\boldsymbol{k})$ are described as

$$\boldsymbol{g}_1^J(\boldsymbol{k}) = \boldsymbol{0}, \tag{A.23}$$

$$\boldsymbol{g}_2^J(\boldsymbol{k}) = -\boldsymbol{g}_3^J(\boldsymbol{k}) = \frac{\lambda\gamma}{\sqrt{f^J(\boldsymbol{k})}}\begin{pmatrix} \sin k_y \\ -\sin k_x \\ 0 \end{pmatrix}. \tag{A.24}$$

Interestingly, the spin-orbit spitting vanishes in the lower band, i.e., $g_1^J(\boldsymbol{k}) = \boldsymbol{0}$. The lower band is labeled by $J = 3/2$ and $M = \pm 3/2$ in the total angular momentum picture, and $|3/2, \pm 3/2\rangle$ do not contain the d_{xy} orbital [see Eqs. (A.12) and (A.15)]. This means that the orbital parity mixing effect [100], which is a necessary condition for the Rashba spin-orbit splitting, does not occur in the lower band. Therefore, Rashba splitting does not occur in the lower band, and indeed, the Rashba splitting in the full Hamiltonian disappears near the Γ-point [Fig. 2.4(c)] where the total angular momentum description is valid. On the other hand, Eq. (A.24) shows that the magnitude of Rashba splitting in the middle band is finite and same as that in the upper band, although the sign of the g-vector is opposite. The $\boldsymbol{k}$-dependence of $g_2^J(\boldsymbol{k}) = -g_3^J(\boldsymbol{k})$ is similar to that of the conventional Rashba SOC with $\boldsymbol{g}(\boldsymbol{k}) = (\sin k_y, -\sin k_x, 0)$, except that the magnitude of the spin-orbit splitting is maximized around the Γ-point [Fig. A.2]. These momentum dependences are different from the results of numerical diagonalization [Fig. 2.4]. This means that the perturbation analysis for the LS coupling is better at most $\boldsymbol{k}$-points in the Brillouin zone.

Appendix B

Group theoretical classification of superconducting states

In this appendix, we provide a classification method of multiorbital/multisublattice superconducting states based on the space group symmetry. First, we consider the transformation of the Bloch wave function under space group operations. A creation operator of a general Bloch state can defined as

$$c^\dagger_{\mathbf{k},mls} = \sum_{\mathbf{R}} c^\dagger_{ls}(\mathbf{R} + \mathbf{r}_m)e^{-i\mathbf{k}\cdot\mathbf{R}}, \tag{B.1}$$

where m, l, and s represent the index for sublattice/layer, local orbital, and spin degrees of freedom, respectively. $\mathbf{R}$ represents the position for the unit cell and $\mathbf{r}_m$ is the relative position of the layer m in a unit cell. Using Eq. (B.1), the creation operator is transformed by a space group operation $g = \{p|\mathbf{a}\}$ as follows:

$$
\begin{aligned}
gc^\dagger_{\mathbf{k},mls}g^{-1} &= \sum_{\mathbf{R}} gc^\dagger_{ls}(\mathbf{R} + \mathbf{r}_m)g^{-1}e^{-i\mathbf{k}\cdot\mathbf{R}}, \\
&= \sum_{\mathbf{R}} e^{-i\mathbf{k}\cdot\mathbf{R}} \sum_{l',s'} c^\dagger_{l's'}(p(\mathbf{R} + \mathbf{r}_m) + \mathbf{a})D^{(\mathrm{orb})}_{l'l}(p)D^{(1/2)}_{s's}(p),
\end{aligned} \tag{B.2}
$$

where $D^{(\mathrm{orb})}(p)$ and $D^{(1/2)}(p)$ are the representation matrices of the point group operation p in the orbital and spin space, respectively. By defining $\mathbf{R}' + \mathbf{r}_{pm} \equiv p(\mathbf{R} + \mathbf{r}_m) + \mathbf{a}$, Eq. (B.2) is rewritten as

$$
\begin{aligned}
gc^\dagger_{\mathbf{k},mls}g^{-1} &= \sum_{\mathbf{R}'} e^{-i\mathbf{k}\cdot[p^{-1}(\mathbf{R}'+\mathbf{r}_{pm}-p\mathbf{r}_m-\mathbf{a})]} \sum_{l',s'} c^\dagger_{l's'}(\mathbf{R}' + \mathbf{r}_{pm})D^{(\mathrm{orb})}_{l'l}(p)D^{(1/2)}_{s's}(p), \\
&= e^{ip\mathbf{k}\cdot\mathbf{a}} \sum_{m',l',s'} c^\dagger_{p\mathbf{k},m'l's'}D^{(\mathrm{perm})}_{m'm}(p,\mathbf{k})D^{(\mathrm{orb})}_{l'l}(p)D^{(1/2)}_{s's}(p).
\end{aligned} \tag{B.3}
$$

Here, we introduced a representation matrix for the permutation of layers as

$$D_{m'm}^{(\mathrm{perm})}(p, \boldsymbol{k}) = e^{-ip\boldsymbol{k}\cdot(\boldsymbol{r}_{pm}-p\boldsymbol{r}_m)}\delta_{m',pm}. \tag{B.4}$$

We investigate the symmetry of superconducting states based on the pair amplitude

$$\mathcal{F}_{mls,m'l's'}(\boldsymbol{k}, i\omega_n) = -\int_0^\beta d\tau e^{i\omega_n\tau}\langle T_\tau c_{\boldsymbol{k},mls}(\tau)c_{-\boldsymbol{k},m'l's'}(0)\rangle, \tag{B.5}$$

where $\omega_n = (2n+1)\pi\beta$ with $n \in \mathbb{Z}$. This pair amplitude satisfies the fermionic antisymmetry as

$$\mathcal{F}_{mls,m'l's'}(\boldsymbol{k}, i\omega_n) = -\mathcal{F}_{m'l's',mls}(-\boldsymbol{k}, -i\omega_n). \tag{B.6}$$

From Eq. (B.3), the pair amplitude is transformed by a space group operation $g = \{p|\boldsymbol{a}\}$ as

$$
\begin{aligned}
g\mathcal{F}_{ms,m's'}^{\Gamma}(\boldsymbol{k}, i\omega_n)g^{-1} &= \sum_{\{m_j,l_j,s_j\}} \mathcal{F}_{m_1l_1s_1,m_2l_2s_2}^{\Gamma}(p\boldsymbol{k}, i\omega_n) \\
&\quad \times \mathcal{D}^{\Gamma}(g)\mathcal{D}_{m_1m_2,mm'}^{(\mathrm{perm})}(p, \boldsymbol{k})\mathcal{D}_{l_1l_2,ll'}^{(\mathrm{orb})}(p)\mathcal{D}_{s_1s_2,ss'}^{(1/2)}(p),
\end{aligned} \tag{B.7}
$$

where the representation matrices are introduced as

$$\mathcal{D}_{m_1m_2,mm'}^{(\mathrm{perm})}(p, \boldsymbol{k}) = D_{m_1m}^{(\mathrm{perm})}(p, \boldsymbol{k})D_{m_2m'}^{(\mathrm{perm})}(p, -\boldsymbol{k}), \tag{B.8}$$

$$\mathcal{D}_{l_1l_2,ll'}^{(\mathrm{orb})}(p) = D_{l_1l}^{(\mathrm{orb})}(p)D_{l_2l'}^{(\mathrm{orb})}(p), \tag{B.9}$$

$$\mathcal{D}_{s_1s_2,ss'}^{(1/2)}(p) = D_{s_1s}^{(1/2)}(p)D_{s_2s'}^{(1/2)}(p), \tag{B.10}$$

and $\mathcal{D}^{\Gamma}(g)$ is the representation matrix of the Γ irreducible representation (IR) for the gap function. Equations (B.6) and (B.7) are the symmetry constraints for the superconducting states. By using Eq. (B.7), we can classify the $\boldsymbol{k}$-dependence of pair amplitudes under a given space group symmetry. Note that the frequency dependence of the pair amplitude is not changed by the space group operations.

Appendix C

Spectroscopic signatures of odd-parity orbital hybridization

In this appendix, we demonstrate possible experimental signatures of the ferroelectricity-induced odd-parity orbital hybridization that leads to the FESC in STO.

C.1 Spectral function
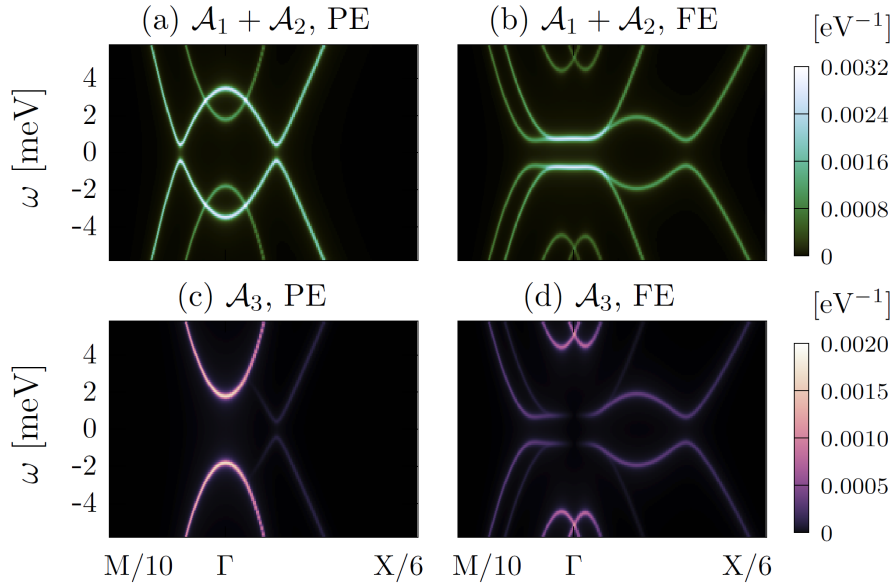
Fig. C.1. Orbital-resolved spectral functions (a) $\mathcal{A}_1(\boldsymbol{k}, \omega) + \mathcal{A}_2(\boldsymbol{k}, \omega)$ in the paraelectric phase, (b) $\mathcal{A}_1(\boldsymbol{k}, \omega) + \mathcal{A}_2(\boldsymbol{k}, \omega)$ in the ferroelectric phase, (c) $\mathcal{A}_3(\boldsymbol{k}, \omega)$ in the paraelectric phase, and (d) $\mathcal{A}_3(\boldsymbol{k}, \omega)$ in the ferroelectric phase. Γ, X, and M refer to $\boldsymbol{k} = (0, 0, 0)$, $\boldsymbol{k} = (\pi, 0, 0)$, and $\boldsymbol{k} = (\pi, \pi, 0)$, respectively.

First, we study the spectral function which can be directly measured by the angle-resolved

photoemission spectroscopy. Using the Matsubara representation of the normal Green's function $\mathcal{G}^0(k)$ in Eq. (2.54), the spectral function is obtained as

$$A(\boldsymbol{k}, \omega) = -\frac{1}{\pi} \text{Im} \mathcal{G}^0(\boldsymbol{k}, \omega + i0^+). \tag{C.1}$$

Here, we define the orbital-resolved spectral function as

$$\mathcal{A}_l(\boldsymbol{k}, \omega) = \sum_{s=\uparrow,\downarrow} A_{ls,ls}(\boldsymbol{k}, \omega), \tag{C.2}$$

whose $(\boldsymbol{k}, \omega)$-dependences are shown in Fig. C.1. The electronic structure near the Fermi level is mainly constructed from d_{yz} and d_{xz} orbitals in the paraelectric phase [Figs. C.1 (a) and C.1 (c)]. Then, d_{yz} and d_{xz} orbitals are responsible for the superconductivity, and the orbital-resolved spectral function $\mathcal{A}_1(\boldsymbol{k}, \omega) + \mathcal{A}_2(\boldsymbol{k}, \omega)$ clearly shows a single superconducting gap at zero energy. In the ferroelectric phase, the orbital-resolved spectral functions exhibit the Rashba spin-orbit splitting due to the space inversion symmetry breaking [Figs. C.1 (b) and C.1 (d)]. Since the odd-parity hybridization $w_{x,y}(\boldsymbol{k})$ induces the mixing between $d_{yz,xz}$ and d_{xy} orbitals, the weight of d_{xy} orbital at the Fermi level is enhanced by the ferroelectric transition [compare Fig. C.1 (d) with Fig. C.1 (c)]. Thus, the contribution of d_{xy} orbital to the superconductivity is increased in the ferroelectric phase.

C.2 Density of states

To see the detail of the superconducting gap structure, we here investigate the DOS which can be measured by tunneling spectroscopy. The DOS is obtained by taking the trace of the spectral function as

$$\mathcal{N}(\omega) = \sum_{\boldsymbol{k}} \text{Tr} A(\boldsymbol{k}, \omega) \equiv \sum_l \mathcal{N}_l(\omega), \tag{C.3}$$

where we defined the orbital-resolved DOS $\mathcal{N}_l(\omega) = \sum_{\boldsymbol{k}} \mathcal{A}_l(\boldsymbol{k}, \omega)$. Figure C.2 shows the total and orbital-resolved DOS in STO. Because of the 4-fold rotational symmetry of the system, the orbital-resolved DOS for d_{yz} orbital $\mathcal{N}_1(\omega)$ and that for d_{xz} orbital $\mathcal{N}_2(\omega)$ are equivalent.

In the paraelectric phase, the DOS exhibits the BCS-like form with a single set of coherence peaks [Fig. C.2 (a)]. The coherence peaks originate from $\mathcal{N}_{1,2}(\omega)$ since the electronic states near the Fermi level are mainly constructed from $d_{yz,xz}$ orbitals [see Figs. C.1 (a) and C.1 (c)]. In the ferroelectric phase, the orbital-resolved DOS for d_{xy} orbital $\mathcal{N}_3(\omega)$ becomes comparable to $\mathcal{N}_{1,2}(\omega)$ owing to the odd-parity hybridization in the ferroelectric phase [Fig. C.2 (b)]. The total DOS shows two sets of the coherence peaks in the ferroelectric phase. The lower energy coherence peaks originate from both $\mathcal{N}_{1,2}(\omega)$ and $\mathcal{N}_3(\omega)$, and hence they are generated by all of t_{2g} orbitals. On the other hand, the higher energy coherence peaks originate only from $\mathcal{N}_{1,2}(\omega)$.
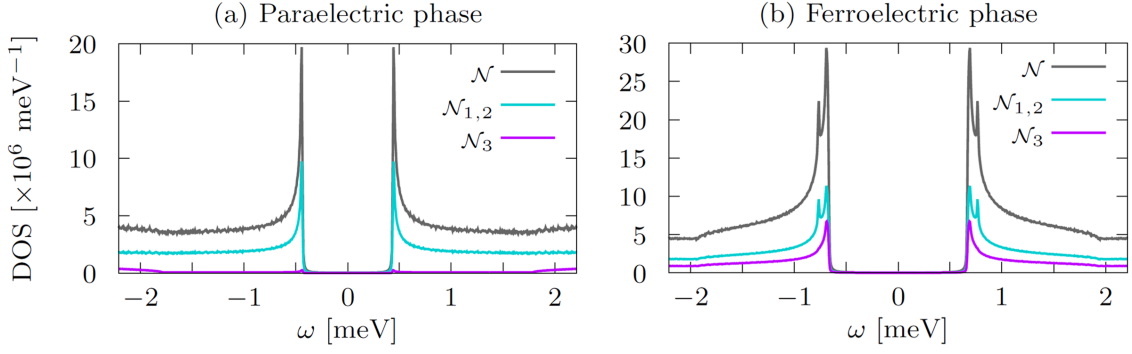
Fig. C.2. The total DOS $\mathcal{N}(\omega)$ and orbital-resolved DOS $\mathcal{N}_l(\omega)$ in the (a) paraelectric phase and (b) ferroelectric phase.

We also note that the DOS shows the ferroelectricity-induced enhancement of superconducting gap which originates from the Lifshitz transition associated to the Rashba splitting of the band structure (see Sec. 2.4.3).

C.3 Superconducting gap structure in band basis

To clarify the ferroelectricity-induced splitting of coherence peaks in the DOS, we here investigate the superconducting gap structure in the band basis. We carry out the band diagonalization for the BdG Hamiltonian as follows:

$$
U(\boldsymbol{k})H(\boldsymbol{k})U^{\dagger}(\boldsymbol{k}) = \begin{pmatrix} \hat{\mathcal{E}}_0(\boldsymbol{k}) & \hat{\Delta}_{\text{band}}(\boldsymbol{k}) \\ \hat{\Delta}^{\dagger}_{\text{band}}(\boldsymbol{k}) & -\hat{\mathcal{E}}_0(-\boldsymbol{k}) \end{pmatrix},
\tag{C.4}
$$

where the unitary matrix $U(\boldsymbol{k})$ is defined as

$$
U(\boldsymbol{k}) = \begin{pmatrix} U_0(\boldsymbol{k}) & \\ & U_0^*(-\boldsymbol{k}) \end{pmatrix}.
\tag{C.5}
$$

The unitary matrix $U_0(\boldsymbol{k})$ diagonalizes the normal state part of the BdG Hamiltonian $H_0(\boldsymbol{k})$, and then the 6×6 diagonal submatrix $\hat{\mathcal{E}}_0(\boldsymbol{k})$ is obtained as

$$
\hat{\mathcal{E}}_0(\boldsymbol{k}) = \begin{pmatrix} \hat{\mathcal{E}}_1(\boldsymbol{k}) & & \\ & \hat{\mathcal{E}}_2(\boldsymbol{k}) & \\ & & \hat{\mathcal{E}}_3(\boldsymbol{k}) \end{pmatrix}, \quad \hat{\mathcal{E}}_\alpha(\boldsymbol{k}) = \begin{pmatrix} \mathcal{E}_\alpha^-(\boldsymbol{k}) & \\ & \mathcal{E}_\alpha^+(\boldsymbol{k}) \end{pmatrix}.
\tag{C.6}
$$

Here, $\mathcal{E}_\alpha^\pm(\boldsymbol{k})$ denotes the energy spectrum in the normal state [$\mathcal{E}_\alpha^\pm(\boldsymbol{k}) \leq \mathcal{E}_{\alpha'}^\pm(\boldsymbol{k})$ ($\alpha \leq \alpha'$) and $\mathcal{E}_\alpha^-(\boldsymbol{k}) \leq \mathcal{E}_\alpha^+(\boldsymbol{k})$]. In the paraelectric phase, the energy spectrum is two-fold degenerate [i.e., $\mathcal{E}_\alpha^-(\boldsymbol{k}) = \mathcal{E}_\alpha^+(\boldsymbol{k})$] owing to the space inversion and time-reversal symmetries. The pairing part

of the BdG Hamiltonian in the band basis $\hat{\Delta}_{\text{band}}(\boldsymbol{k})$ can be described as

$$\hat{\Delta}_{\text{band}}(\boldsymbol{k}) = \begin{pmatrix} \hat{\Delta}_{11}(\boldsymbol{k}) & \hat{\Delta}_{12}(\boldsymbol{k}) & \hat{\Delta}_{13}(\boldsymbol{k}) \\ \hat{\Delta}_{21}(\boldsymbol{k}) & \hat{\Delta}_{22}(\boldsymbol{k}) & \hat{\Delta}_{23}(\boldsymbol{k}) \\ \hat{\Delta}_{31}(\boldsymbol{k}) & \hat{\Delta}_{32}(\boldsymbol{k}) & \hat{\Delta}_{33}(\boldsymbol{k}) \end{pmatrix}, \quad \hat{\Delta}_{\alpha\alpha'}(\boldsymbol{k}) = \begin{pmatrix} \Delta_{\alpha\alpha'}^{-}(\boldsymbol{k}) & \Delta_{\alpha\alpha'}^{-+}(\boldsymbol{k}) \\ \Delta_{\alpha\alpha'}^{+-}(\boldsymbol{k}) & \Delta_{\alpha\alpha'}^{+}(\boldsymbol{k}) \end{pmatrix}. \quad \text{(C.7)}$$

In our calculations, the superconductivity is dominated by the two lowest energy bands that construct the Fermi surfaces. Then, the effective two-band Hamiltonian for the two lowest energy bands $\mathcal{E}_1^{\pm}(\boldsymbol{k})$ can be obtained as

$$\hat{H}_{\text{eff}}(\boldsymbol{k}) = \begin{pmatrix} \hat{\mathcal{E}}_1(\boldsymbol{k}) & \hat{\Delta}_{11}(\boldsymbol{k}) \\ \hat{\Delta}_{11}^{\dagger}(\boldsymbol{k}) & -\hat{\mathcal{E}}_1(-\boldsymbol{k}) \end{pmatrix}, \quad \text{(C.8)}$$

by neglecting the higher energy bands that do not give rise to the Fermi surface.
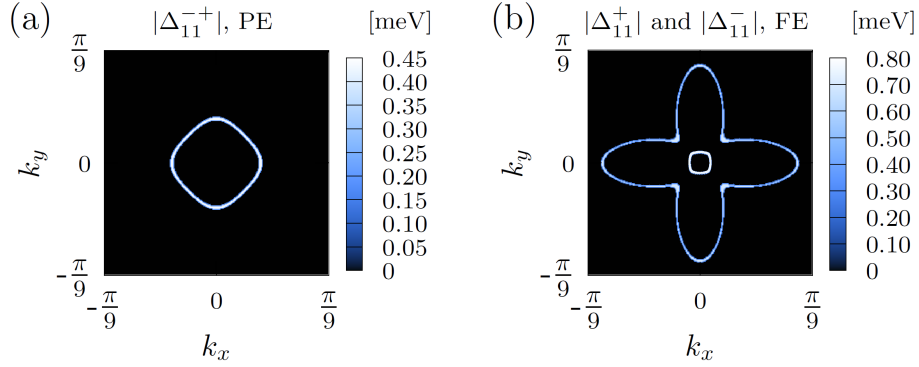
Fig. C.3. $\boldsymbol{k}$-dependence of the superconducting gap on the Fermi surfaces. (a) $|\Delta_{11}^{-+}(\boldsymbol{k})|(= |\Delta_{11}^{+-}(\boldsymbol{k})|)$ in the paraelectric phase and (b) $|\Delta_{11}^{+}(\boldsymbol{k})|$ and $|\Delta_{11}^{-}(\boldsymbol{k})|$ in the ferroelectric phase.

In the paraelectric phase, the pseudospin-singlet superconducting state is stabilized [i.e., $\Delta_{11}^{\pm}(\boldsymbol{k}) = 0$ and $\Delta_{11}^{-+}(\boldsymbol{k}) = -\Delta_{11}^{+-}(\boldsymbol{k})$]. Thus, the superconducting gap in the paraelectric phase is given by $2|\Delta_{11}^{-+}(\boldsymbol{k})|$. Figure C.3 (a) shows the superconducting gap amplitude $|\Delta_{11}^{-+}(\boldsymbol{k})|$ on the Fermi surfaces in the paraelectric phase. It is shown that the magnitude of $|\Delta_{11}^{-+}(\boldsymbol{k})|$ is consistent with the energy gap in the DOS [compare Fig. C.3 (a) with Fig. C.2 (a)].

On the other hand, in the ferroelectric phase, the intraband superconducting state is stabilized as $\Delta_{11}^{\pm}(\boldsymbol{k}) \neq 0$ and $\Delta_{11}^{\mp\pm}(\boldsymbol{k}) \simeq 0$. Then, the superconducting gaps for each Fermi surfaces are given by $2|\Delta_{11}^{\pm}(\boldsymbol{k})|$. Fig. C.3 (b) shows the superconducting gap amplitudes on the Rashba-split Fermi surfaces in the ferroelectric phase. The gap amplitude on the inner (outer) Fermi surface is given by $|\Delta_{11}^{+}(\boldsymbol{k})|$ ($|\Delta_{11}^{-}(\boldsymbol{k})|$). The difference between $|\Delta_{11}^{+}(\boldsymbol{k})|$ and $|\Delta_{11}^{-}(\boldsymbol{k})|$ leads to a two gap structure shown in Fig. C.2 (b). Here, we estimate the splitting width of the coherence

peaks in the ferroelectric phase as

$$\delta = \max_{\boldsymbol{k}_\mathrm{F}} |\Delta_{11}^+(\boldsymbol{k}_\mathrm{F})| - \max_{\boldsymbol{k}_\mathrm{F}} |\Delta_{11}^-(\boldsymbol{k}_\mathrm{F})|, \tag{C.9}$$

where $\boldsymbol{k}_\mathrm{F}$ denotes the Fermi momentum. Then, we obtain $\delta \simeq 0.0697$ meV in the ferroelectric phase, which is indeed approximately equal to the splitting width of the coherence peaks shown in Fig. C.2 (b) (i.e., ~ 0.07 meV). The difference between $|\Delta_{11}^+(\boldsymbol{k})|$ and $|\Delta_{11}^-(\boldsymbol{k})|$ originates from their different orbital character. The orbital-resolved spectral function $\mathcal{A}_3(\boldsymbol{k}, \omega)$ reveals that d_{xy} orbital does not contribute to the superconducting gap opening at Γ-point in the ferroelectric phase [see Fig. C.1 (d)], since the odd-parity hybridization vanishes at $k_{x,y} = 0$ [i.e., $w_x(0, k_y, k_z) = w_y(k_x, 0, k_z) = 0$]. On the other hand, the inner (outer) Fermi surface for the higher (lower) energy band $\mathcal{E}_1^+(\boldsymbol{k})$ ($\mathcal{E}_1^-(\boldsymbol{k})$) is located near the Γ-point (away from the Γ-point). Then, $\Delta_{11}^+(\boldsymbol{k})$ is mainly constructed from $d_{yz,xz}$ orbitals, while $\Delta_{11}^-(\boldsymbol{k})$ has contribution from d_{xy} orbital comparable to that from $d_{yz,xz}$ orbitals. Therefore, $|\Delta_{11}^+(\boldsymbol{k})| > |\Delta_{11}^-(\boldsymbol{k})|$ is realized because the superconducting order parameter for $d_{yz,xz}$ orbitals is larger than that for d_{xy} orbital (i.e., $\Delta_{1,2} > \Delta_3$) in our calculation [see Table 2.4]. Indeed, the higher energy coherence peaks at $\pm\Delta_{11}^+(\boldsymbol{k})$ for the inner Fermi surface are constructed only from $d_{yz,xz}$ orbitals. Note that the two gap structure does not appear in single-orbital s-wave Rashba superconductors[1], and it is indeed a fingerprint of multiorbital Rashba superconductors. Besides, it should be noticed that the two gap structure discussed above is essentially different from that due to parity mixing in Cooper pairs.

Finally, we investigate relationship between the value of γ and the ferroelectricity-induced

---

[1]Single-orbital Rashba superconductors can be described by the following model Hamiltonian:

$$\mathcal{H} = \sum_{\boldsymbol{k},s} \xi(\boldsymbol{k}) c_{\boldsymbol{k},s}^\dagger c_{\boldsymbol{k},s} + \sum_{\boldsymbol{k},s,s'} \alpha \boldsymbol{g}(\boldsymbol{k}) \cdot \boldsymbol{\sigma}_{ss'} c_{\boldsymbol{k},s}^\dagger c_{\boldsymbol{k},s'} + \frac{1}{2} \sum_{\boldsymbol{k},s,s'} \Delta_{ss'}(\boldsymbol{k}) c_{\boldsymbol{k},s}^\dagger c_{-\boldsymbol{k},s'}^\dagger + \mathrm{H.c.}, \tag{C.10}$$

where $c_{\boldsymbol{k},s}$ is the annihilation operator for an electron with momentum $\boldsymbol{k}$ and spin $s = \uparrow, \downarrow$. $\xi(\boldsymbol{k})$ is the single-electron kinetic energy. The Rashba spin-orbit coupling takes the form $\boldsymbol{g}(\boldsymbol{k}) = \sin k_y \hat{\boldsymbol{x}} - \sin k_x \hat{\boldsymbol{y}}$. We assume the superconducting gap function as

$$\Delta_{ss'}(\boldsymbol{k}) = \left[\left(\Delta^s \sigma^0 + \Delta^p \boldsymbol{g}(\boldsymbol{k}) \cdot \boldsymbol{\sigma} \right) i\sigma^y \right]_{ss'}, \tag{C.11}$$

where Δ^s is the spin-singlet s-wave component of the gap function, and Δ^p is the spin-triplet p-wave component. By diagonalizing the BdG Hamiltonian, we obtain the energy spectrum as follows:

$$E(\boldsymbol{k}) = \pm\sqrt{\mathcal{E}_\pm(\boldsymbol{k})^2 + |\Delta_\pm(\boldsymbol{k})|^2}, \tag{C.12}$$

where $\mathcal{E}_\pm(\boldsymbol{k}) = \xi(\boldsymbol{k}) \pm \alpha|\boldsymbol{g}(\boldsymbol{k})|$ and the superconducting gap functions in the band basis are given by

$$\Delta_\pm(\boldsymbol{k}) = \frac{\pm g_x(\boldsymbol{k}) + i g_y(\boldsymbol{k})}{|\boldsymbol{g}(\boldsymbol{k})|} \left(\Delta^s \pm \Delta^p |\boldsymbol{g}(\boldsymbol{k})| \right). \tag{C.13}$$

In the absence of the parity-mixing-induced p-wave pairing interaction ($\Delta^p = 0$), the superconducting gaps for each Rashba split bands are equal ($|\Delta_-(\boldsymbol{k})| = |\Delta_+(\boldsymbol{k})| = |\Delta^s|$). Therefore, the multiple superconducting gap structure such as in Fig. C.2 (b) is not realized in single-orbital s-wave Rashba superconductors.
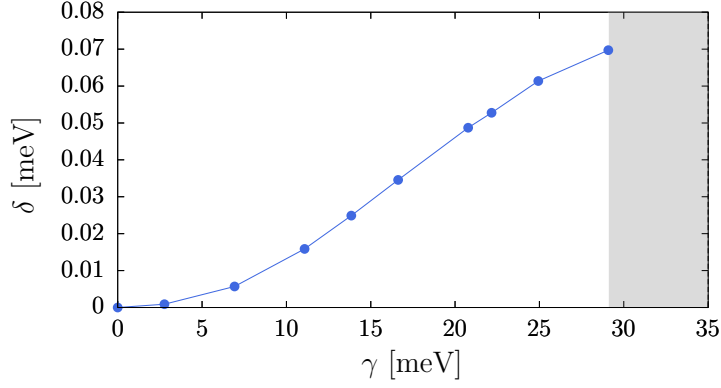
Fig. C.4. γ-dependence of the splitting width of the coherence peaks estimated as $\delta = \max_{k_F}|\Delta_{11}^+(k_F)| - \max_{k_F}|\Delta_{11}^-(k_F)|$. The carrier density and superconducting order parameters are set to be $n = 5.0 \times 10^{-5}$, $\Delta_{1,2} = 0.00277$, and $\Delta_3 = 0.00138$, respectively. In the gray area ($\gamma > 0.105t_1 \simeq 29.1$ meV), the superconducting gap $\Delta_{11}^+(k_F)$ is not defined because of the Lifshitz transition, which is associated with the disappearance of the inner Fermi surface.

splitting of the coherence peaks. It would give important insight for experimental determination of the value of γ in the ferroelectric phase of bulk STO, which is so far unknown. Figure C.4 shows the γ-dependence of the splitting width of the coherence peaks δ given by Eq. (C.9). The superconducting order parameters $\boldsymbol{\Delta} = (\Delta_1, \Delta_2, \Delta_3)$ are set to be the values in the ferroelectric phase [see the third column of Table 2.4], which are obtained by minimizing the free energy. In this setting, we change γ and calculate δ. Note that the true value of γ, which minimizes the free energy, is $\gamma_0 = 0.105t_1 \simeq 29.1$ meV in our numerical calculation. It is shown that the splitting width δ gradually increases by increasing the value of γ, and tends to saturate as the value of γ approaches to γ_0. The inner Fermi pocket disappears at slightly above $\gamma = \gamma_0$ due to the Lifshitz transition associated to the Rashba splitting, and thus δ is not calculated for $\gamma > \gamma_0$ (gray area in Fig. C.4). We note that the thermodynamically stable ferroelectric superconducting state always exhibits a nearly largest value of δ at $\gamma = \gamma_0$, since the stabilization of the ferroelectric superconducting state is owing to the enhancement of the condensation energy gain at the Lifshitz transition point $\gamma = \gamma_0$ (see Sec. 2.4.3).

Appendix D

Calculation of Chern number

In this appendix, we derive the Chern number for the E_u $p_x + ip_y$-wave pairing state in a large Zeeman SOC region [Figs. 3.9 (c) and 3.9 (d) in Sec. 3.4]. Figure D.1 illustrates the band structure near the Fermi level under a large Zeeman SOC. Since the fourfold degeneracy at the K (K′) point is lifted by the Zeeman SOC, the band structure possesses a nearly parabolic shape around the K (K′) point. In addition, the interlayer hybridization is negligible around the K (K′) point owing to the threefold rotational symmetry [167, 176, 177]. Then, the effective Hamiltonian for electrons near the Fermi level is derived as

$$
\tilde{\mathcal{H}} = \sum_{\boldsymbol{q},m,s} \left(\tilde{\varepsilon}_{\boldsymbol{q}} - \mu \right) \psi^{\dagger}_{\boldsymbol{q},ms} \psi_{\boldsymbol{q},ms}
$$
$$
+ \frac{1}{2} \sum_{\boldsymbol{q},m,s,s'} \tilde{\Delta}_{\boldsymbol{q}} \bar{\sigma}^{z}_{ss'} \psi^{\dagger}_{\boldsymbol{q},ms} \psi^{\dagger}_{-\boldsymbol{q},ms'} + \text{H.c.}, \tag{D.1}
$$

where $\tilde{\varepsilon}_{\boldsymbol{q}} = \boldsymbol{q}^2/(2m)$ is the effective kinetic energy with a parabolic dispersion, $\tilde{\Delta}_{\boldsymbol{q}} = \tilde{\Delta}^p(q_x + iq_y)$ is the effective chiral p-wave gap function, and the annihilation operators are defined as
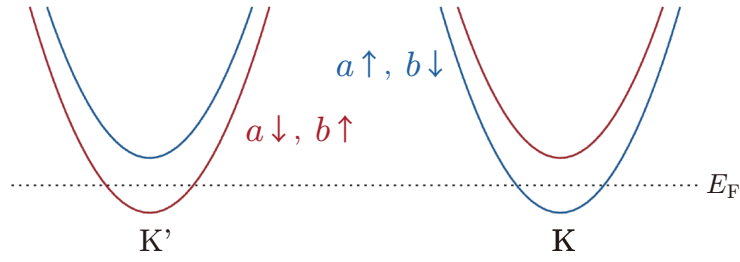
$$
\left(\psi_{\boldsymbol{q},a\uparrow}, \psi_{\boldsymbol{q},a\downarrow}, \psi_{\boldsymbol{q},b\uparrow}, \psi_{\boldsymbol{q},b\downarrow} \right) \equiv \left(c_{\mathbf{K}+\boldsymbol{q},a\uparrow}, c_{-\mathbf{K}+\boldsymbol{q},a\downarrow}, c_{-\mathbf{K}+\boldsymbol{q},b\uparrow}, c_{\mathbf{K}+\boldsymbol{q},b\downarrow} \right). \tag{D.2}
$$

We assume that $\tilde{\Delta}^p$ is a real number. By using the vector operator

$$
\hat{\Psi}^{\dagger}_{\boldsymbol{q},m} = \left(\psi^{\dagger}_{\boldsymbol{q},m\uparrow}, \psi_{-\boldsymbol{q},m\uparrow}, \psi^{\dagger}_{\boldsymbol{q},m\downarrow}, \psi_{-\boldsymbol{q},m\downarrow}, \right), \tag{D.3}
$$

we obtain the matrix representation of the effective Hamiltonian as follows:

$$
\tilde{\mathcal{H}} = \frac{1}{2} \sum_{\boldsymbol{q}} \left(\hat{\Psi}^{\dagger}_{\boldsymbol{q},a}, \hat{\Psi}^{\dagger}_{\boldsymbol{q},b} \right) \tilde{H}_{\boldsymbol{q}} \begin{pmatrix} \hat{\Psi}_{\boldsymbol{q},a} \\ \hat{\Psi}_{\boldsymbol{q},b} \end{pmatrix} + \text{const.}, \tag{D.4}
$$

Fig. D.1. Schematic of the band structure near the K and K′ points in a large Zeeman SOC region. The Fermi energy E_F lies between the Zeeman gap.

where the Hamiltonian matrix $\tilde{H}_q$ is given by

$$\tilde{H}_q = \tau^0 \otimes \begin{pmatrix} (\tilde{\varepsilon}_q - \mu)\sigma^z & \tilde{\Delta}^p \left(q_x\sigma^x - q_y\sigma^y\right) \\ \tilde{\Delta}^p \left(q_x\sigma^x - q_y\sigma^y\right) & (\tilde{\varepsilon}_q - \mu)\sigma^z \end{pmatrix}. \tag{D.5}$$

Here, we carry out an unitary transformation as

$$U\tilde{H}_q U^\dagger = \tau^0 \otimes \begin{pmatrix} \tilde{H}_q^+ & 0 \\ 0 & \tilde{H}_q^- \end{pmatrix}, \tag{D.6}$$

$$\tilde{H}_q^\pm = \begin{pmatrix} \tilde{\varepsilon}_q - \mu & \pm\tilde{\Delta}^p(q_x + iq_y) \\ \pm\tilde{\Delta}^p(q_x - iq_y) & -\tilde{\varepsilon}_q + \mu \end{pmatrix}, \tag{D.7}$$

where the unitary matrix U is defined as

$$U = \frac{1}{\sqrt{2}}\tau^0 \otimes \begin{pmatrix} \sigma^0 & \sigma^0 \\ \sigma^0 & -\sigma^0 \end{pmatrix}. \tag{D.8}$$

Equation (D.7) is the BdG Hamiltonian for the spinless chiral p-wave superconductivity. Thus, the spin-full chiral p-wave superconducting state is converted to two pairs of the spinless chiral p-wave superconducting states [173]. Since a spinless chiral p-wave superconducting state gives the Chern number 1, the total Chern number of the E_u chiral p-wave superconducting state is obtained as $\nu_{\text{Ch}} = 1 \times 2 \times 2 = 4$.

Appendix E

Correspondence between Pauli matrices and Dirac matrices

In this appendix, we demonstrate that the general form of the BdG Hamiltonian with spin-1/2 and a two-valued extra DOF can be expressed by using the Euclidean Dirac matrices as shown in Sec. 4.2.

Since we assume that the normal state preserves both $\mathcal{P}$- and $\mathcal{T}$-symmetries, $H_0(\boldsymbol{k})$ transforms under the space-inversion $\mathcal{P}$ and the time-reversal $\mathcal{T}$ as

$$H_0(\boldsymbol{k}) \xrightarrow{\mathcal{P}} U_P^\dagger H_0(-\boldsymbol{k})U_P = H_0(\boldsymbol{k}), \tag{E.1}$$

$$H_0(\boldsymbol{k}) \xrightarrow{\mathcal{T}} U_T^\dagger H_0^*(-\boldsymbol{k})U_T = H_0(\boldsymbol{k}), \tag{E.2}$$

where U_P and U_T are unitary matrices. In this paper, we consider a spin-1/2 system satisfying $U_T U_T^* = -\mathbb{1}_4$. In addition, we require that the time-reversal commute with the space-inversion (i.e., $U_P U_T = U_T U_P^*$), and the space-inversion operator is its own inverse (i.e., $U_P^2 = \mathbb{1}_4$). Under the above assumptions, $H_0(\boldsymbol{k})$ can be generally expressed as

$$H_0(\boldsymbol{k}) = (\epsilon_{\boldsymbol{k}}^0 - \mu)\sigma_0 \otimes \tau_0 + f_{\boldsymbol{k}}\sigma_0 \otimes \tau_{x_i}$$
$$+ \boldsymbol{g}_{\boldsymbol{k}} \cdot \boldsymbol{\sigma} \otimes \tau_{y_i} + h_{\boldsymbol{k}}\sigma_0 \otimes \tau_{z_i}, \tag{E.3}$$

where $\boldsymbol{\sigma} = (\sigma_x, \sigma_y, \sigma_z)$ and $\sigma_0 \otimes \tau_0 = \mathbb{1}_4$. Hermiticity requires all coefficients in Equation (E.3) are real. The index i specifies the extra DOF and (x_i, y_i, z_i) is a permutation of (x, y, z). Since U_P and U_T vary depending on the extra DOF, the general models (E.3) are classified by the index i. In this paper, we consider three representative examples shown in Table E.1. For $i = 1$ ($i = 2$), the extra DOF is orbitals with the same (opposite) parity, and $U_P = \sigma_0 \otimes \tau_0$ ($U_P = \sigma_0 \otimes \tau_z$). For $i = 3$, the extra DOF is sublattices in a locally noncentrosymmetric crystal structure, and $U_P = \sigma_0 \otimes \tau_x$. In these cases, $U_T = i\sigma_y \otimes \tau_0$. Although the extra DOF can be other than the above three cases, Eq. (E.3) holds for all the cases unless $U_P U_T \neq U_T U_P^*$, $U_P U_P \neq \mathbb{1}_4$,

Table E.1. Classification of two-band models based on the extra DOF. (x_i, y_i, z_i), U_P, and U_T for $i = 1, 2, 3$ are listed.

	(x_i, y_i, z_i)	U_P	U_T	DOF
$i = 1$	(x, y, z)	$\sigma_0 \otimes \tau_0$	$i\sigma_y \otimes \tau_0$	orbitals (same parity)
$i = 2$	(z, x, y)	$\sigma_0 \otimes \tau_z$	$i\sigma_y \otimes \tau_0$	orbitals (opposite parity)
$i = 3$	(y, z, x)	$\sigma_0 \otimes \tau_x$	$i\sigma_y \otimes \tau_0$	sublattices

or $U_T U_T^* \neq -\mathbb{1}_4$ [209]. Since the set of $\sigma_\mu \otimes \tau_\nu$ matrices is completely anticommuting in Eq. (E.3), we can substitute them by the five anticommuting Euclidean Dirac matrices. Then, we can rewrite Eq. (E.3) as Eq. (4.2).

The pairing potential $\Delta(\boldsymbol{k})$ transforms under the space-inversion and the time-reversal as $\Delta(\boldsymbol{k}) \xrightarrow{\mathcal{P}} U_P^\dagger \Delta(-\boldsymbol{k}) U_P^*$ and $\Delta(\boldsymbol{k}) \xrightarrow{\mathcal{T}} U_T^\dagger \Delta^*(-\boldsymbol{k}) U_T^*$, respectively. In terms of $\hat{\Delta}(\boldsymbol{k}) = \Delta(\boldsymbol{k}) U_T^\dagger$, these relations can be rewritten as

$$\hat{\Delta}(\boldsymbol{k}) \xrightarrow{\mathcal{P}} U_P^\dagger \hat{\Delta}(-\boldsymbol{k}) U_P, \tag{E.4}$$

$$\hat{\Delta}(\boldsymbol{k}) \xrightarrow{\mathcal{T}} \hat{\Delta}^\dagger(\boldsymbol{k}). \tag{E.5}$$

We note that Eq. (E.4) is equivalent to the transformation property of $H_0(\boldsymbol{k})$ under the space-inversion [see Eq. (E.1)], while Eq. (E.5) corresponds to the Hermiticity condition. Whereas $H_0(\boldsymbol{k})$ is assumed to preserve both $\mathcal{P}$- and $\mathcal{T}$-symmetries, we admit that $\Delta(\boldsymbol{k})$ spontaneously breaks the $\mathcal{P}$- and $\mathcal{T}$-symmetries. The only requirements for the pairing potential is satisfying the fermionic antisymmetry $\Delta(\boldsymbol{k}) = -\Delta^{\mathrm{T}}(-\boldsymbol{k})$, which can be rewritten as

$$\hat{\Delta}(\boldsymbol{k}) = U_T^\dagger \hat{\Delta}^{\mathrm{T}}(-\boldsymbol{k}) U_T, \tag{E.6}$$

where we used the fact that $U_T^\dagger = U_T^{\mathrm{T}} = -U_T$ by choosing U_T as real (i.e., $U_T = U_T^*$). It should be noticed that Eq. (E.6) is formally equivalent to the time-reversal symmetry for $H_0(\boldsymbol{k})$ [see Eq. (E.2)]. Since the even-parity part of $\hat{\Delta}(\boldsymbol{k})$ obeys transformation properties completely equivalent to those of $H_0(\boldsymbol{k})$ under the time-reversal and the space-inversion, it can be expressed as a linear combination of six $\sigma_\mu \otimes \tau_\nu$ matrices allowed to appear in $H_0(\boldsymbol{k})$. On the other hand, the other ten $\sigma_\mu \otimes \tau_\nu$ matrices, which correspond to $i\gamma_m\gamma_n$ ($1 \leq m < n \leq 5$), constitute the odd-parity pairing potential. Then, we obtain a general form of $\Delta(\boldsymbol{k})$ as

$$\hat{\Delta}(\boldsymbol{k}) = \Delta_1 \left[\sum_{\nu=0,x_i,z_i} \psi_{\boldsymbol{k}}^\nu \sigma_0 \otimes \tau_\nu + \boldsymbol{d}_{\boldsymbol{k}}^{y_i} \cdot \boldsymbol{\sigma} \otimes \tau_{y_i} \right]$$
$$+ \Delta_2 \left[\sum_{\nu=0,x_i,z_i} \boldsymbol{d}_{\boldsymbol{k}}^\nu \cdot \boldsymbol{\sigma} \otimes \tau_\nu + \psi_{\boldsymbol{k}}^{y_i} \sigma_0 \otimes \tau_{y_i} \right], \tag{E.7}$$

Table E.2. Necessary conditions for the asymmetric Bogoliubov spectrum in two-band models ($\sigma_\mu \otimes \tau_\nu$ basis).

	Criterion (i)	Criterion (ii)
(I)		$\psi_{\bm{k}}^{z_i}\psi_{\bm{k}}^{y_i} f_{\bm{k}} \neq 0$
(II)		$(\bm{d}_{\bm{k}}^{y_i} \cdot \bm{d}_{\bm{k}}^{z_i}) f_{\bm{k}} \neq 0$
(III)		$\psi_{\bm{k}}^{x_i}(\bm{d}_{\bm{k}}^{z_i} \cdot \bm{g}_{\bm{k}}) \neq 0$
(IV)	$\mathrm{Im}(\Delta_1 \Delta_2^*) \neq 0$	$\psi_{\bm{k}}^{z_i}(\bm{d}_{\bm{k}}^{x_i} \cdot \bm{g}_{\bm{k}}) \neq 0$
(V)		$(\bm{d}_{\bm{k}}^{y_i} \times \bm{d}_{\bm{k}}^{0}) \cdot \bm{g}_{\bm{k}} \neq 0$
(VI)		$(\bm{d}_{\bm{k}}^{y_i} \cdot \bm{d}_{\bm{k}}^{x_i}) h_{\bm{k}} \neq 0$
(VII)		$\psi_{\bm{k}}^{x_i}\psi_{\bm{k}}^{y_i} h_{\bm{k}} \neq 0$

where $\psi_{\bm{k}}^{\gamma}$ and $\bm{d}_{\bm{k}}^{\gamma}$ are real-valued coefficients. Note that Δ_1 and Δ_2 are complex valued since $\hat{\Delta}(\bm{k}) \neq \hat{\Delta}^\dagger(\bm{k})$ in $\mathcal{T}$-symmetry breaking superconducting phases. From Eq. (E.7), we obtain Eq. (4.3) as a general form of $\Delta(\bm{k})$ in two-band models.

From Eqs. (E.3) and (E.7), we obtain

$$\mathrm{Tr}[M_-^{(1)}(\bm{k})\tilde{H}_0(\bm{k})] = 8\mathrm{Im}(\Delta_1\Delta_2^*)\big[(\psi_{\bm{k}}^{z_i}\psi_{\bm{k}}^{y_i} - \bm{d}_{\bm{k}}^{y_i} \cdot \bm{d}_{\bm{k}}^{z_i})f_{\bm{k}}$$
$$+ (\psi_{\bm{k}}^{x_i}\bm{d}_{\bm{k}}^{z_i} - \psi_{\bm{k}}^{z_i}\bm{d}_{\bm{k}}^{x_i} - \bm{d}_{\bm{k}}^{y_i} \times \bm{d}_{\bm{k}}^{0}) \cdot \bm{g}_{\bm{k}}$$
$$+ (\bm{d}_{\bm{k}}^{y_i} \cdot \bm{d}_{\bm{k}}^{x_i} - \psi_{\bm{k}}^{x_i}\psi_{\bm{k}}^{y_i})h_{\bm{k}}\big]. \tag{E.8}$$

Then, in the $\sigma_\mu \otimes \tau_\nu$ basis, the necessary conditions for the asymmetric Bogoliubov spectrum (i.e., $\mathrm{Tr}[M_-^{(1)}(\bm{k})\tilde{H}_0(\bm{k})] \neq 0$) can be summarized as shown in Table E.2. For example, the condition (I) means that the asymmetric Bogoliubov spectrum appears when $\mathrm{Im}(\Delta_1\Delta_2^*) \neq 0$ and $\psi_{\bm{k}}^{z_i}\psi_{\bm{k}}^{y_i} f_{\bm{k}} \neq 0$.

Appendix F

Derivation of $\mathcal{P}, \mathcal{T}$-odd bilinear product

In this appendix, we derive a formula to calculate the $\mathcal{P}, \mathcal{T}$-odd bilinear product, which is used in Chap. 4. To obtain the formula, we first consider the transformation property of the bilinear product $\Delta(\boldsymbol{k})\Delta^{\dagger}(\boldsymbol{k})$ under the time-reversal. Since the time-reversed counterpart of $\hat{\Delta}(\boldsymbol{k}) = \Delta(\boldsymbol{k})U_T^{\dagger}$ is $\hat{\Delta}^{\dagger}(\boldsymbol{k})$, the transformation property of the bilinear product $\Delta(\boldsymbol{k})\Delta^{\dagger}(\boldsymbol{k}) = \hat{\Delta}(\boldsymbol{k})\hat{\Delta}^{\dagger}(\boldsymbol{k})$ under the time-reversal $\mathcal{T}$ is obtained as

$$\Delta(\boldsymbol{k})\Delta^{\dagger}(\boldsymbol{k}) = \hat{\Delta}(\boldsymbol{k})\hat{\Delta}^{\dagger}(\boldsymbol{k}) \xrightarrow{\mathcal{T}} \hat{\Delta}^{\dagger}(\boldsymbol{k})\hat{\Delta}(\boldsymbol{k}). \tag{F.1}$$

Then, we define the time-reversal-odd bilinear product $M^{(1)}(\boldsymbol{k})$ as

$$M^{(1)}(\boldsymbol{k}) = \frac{1}{2}\left[\hat{\Delta}(\boldsymbol{k})\hat{\Delta}^{\dagger}(\boldsymbol{k}) - \hat{\Delta}^{\dagger}(\boldsymbol{k})\hat{\Delta}(\boldsymbol{k})\right] = \frac{1}{2}[\hat{\Delta}(\boldsymbol{k}), \hat{\Delta}^{\dagger}(\boldsymbol{k})]. \tag{F.2}$$

Equation (F.2) extracts the time-reversal-odd part of the bilinear product $\Delta(\boldsymbol{k})\Delta^{\dagger}(\boldsymbol{k})$ [208, 209]. Here, we decompose the pairing potential $\Delta(\boldsymbol{k})$ into the even-parity part $\Delta^g(\boldsymbol{k})$ and odd-parity part $\Delta^u(\boldsymbol{k})$ as

$$\Delta(\boldsymbol{k}) = \Delta^g(\boldsymbol{k}) + \Delta^u(\boldsymbol{k}). \tag{F.3}$$

Then, $\Delta(\boldsymbol{k})$ transforms under the space-inversion $\mathcal{P}$ as

$$\Delta(\boldsymbol{k}) = \Delta^g(\boldsymbol{k}) + \Delta^u(\boldsymbol{k}) \xrightarrow{\mathcal{P}} \Delta^g(\boldsymbol{k}) - \Delta^u(\boldsymbol{k}). \tag{F.4}$$

From Eq. (F.4), $M^{(1)}(\boldsymbol{k})$ transforms under the space-inversion $\mathcal{P}$ as

$$M^{(1)}(\boldsymbol{k}) = M_+^{(1)}(\boldsymbol{k}) + M_-^{(1)}(\boldsymbol{k}) \xrightarrow{\mathcal{P}} M_+^{(1)}(\boldsymbol{k}) - M_-^{(1)}(\boldsymbol{k}), \tag{F.5}$$

where

$$M_+^{(1)}(\boldsymbol{k}) = \frac{1}{2}\left([\hat{\Delta}^g(\boldsymbol{k}), \hat{\Delta}^{g\dagger}(\boldsymbol{k})] + [\hat{\Delta}^u(\boldsymbol{k}), \hat{\Delta}^{u\dagger}(\boldsymbol{k})]\right),\tag{F.6}$$

$$M_-^{(1)}(\boldsymbol{k}) = \frac{1}{2}\left([\hat{\Delta}^g(\boldsymbol{k}), \hat{\Delta}^{u\dagger}(\boldsymbol{k})] + [\hat{\Delta}^u(\boldsymbol{k}), \hat{\Delta}^{g\dagger}(\boldsymbol{k})]\right).\tag{F.7}$$

$M_+^{(1)}(\boldsymbol{k})$ and $M_-^{(1)}(\boldsymbol{k})$ are the even-parity and odd-parity part of the time-reversal-odd bilinear product $M^{(1)}(\boldsymbol{k})$, respectively. Then, Eq. (F.7) represents the $\mathcal{P}, \mathcal{T}$-odd nonunitary part of $\Delta(\boldsymbol{k})\Delta^{\dagger}(\boldsymbol{k})$.

Appendix G

Derivation of Ginzburg-Landau Free energy

In this appendix, we perform the GL expansion of the free energy for the mixed-parity superconductivity. Then, we derive an analytical expression of the GL free energy for a model satisfying one of the necessary conditions to realize the asymmetric Bogoliubov spectrum (Sec. 4.4).

We consider the Hamiltonian $\mathcal{H} = \mathcal{H}_0 + \mathcal{H}_{\text{int}}$, which is composed of the single-particle term $\mathcal{H}_0$ and pairing interaction term $\mathcal{H}_{\text{int}}$. The pairing interaction $\mathcal{H}_{\text{int}}$ is assumed to be a mixture of even-parity and odd-parity channels as

$$\mathcal{H}_{\text{int}} = \frac{1}{2} \sum_{j=1,2} V_j B_j^\dagger(\boldsymbol{q}) B_j(\boldsymbol{q}), \tag{G.1}$$

where $\boldsymbol{q} = (q_x, q_y, q_z)$ is the center-of-mass momentum of the Cooper pairs, $V_j(<0)$ is the strength of the pairing interaction, and $j = 1$ ($j = 2$) represents an index of the even-parity (odd-parity) pairing channel. Note that we assume a single-$\boldsymbol{q}$ state in Eq. (G.1). The creation operator of the Cooper pairs $B_j^\dagger(\boldsymbol{q})$ is given by

$$B_j^\dagger(\boldsymbol{q}) = \sum_{\boldsymbol{k}} \sum_{ll',ss'} \varphi_{ls,l's'}^j(\boldsymbol{k}) c_{\boldsymbol{k}+\boldsymbol{q}/2,ls}^\dagger c_{-\boldsymbol{k}+\boldsymbol{q}/2,l's'}^\dagger, \tag{G.2}$$

where $s, s' = \uparrow, \downarrow$ and $l, l' = 1, 2$ are indexes for the spin-1/2 and extra two-valued DOF, respectively. Here, we apply the mean-field approximation to $\mathcal{H}_{\text{int}}$ as

$$\mathcal{H}_{\text{int}} \approx \frac{1}{2} \sum_{j=1,2} \sum_{\boldsymbol{k}} \sum_{ls,l's'} \left[\Delta_j \varphi_{ls,l's'}^j(\boldsymbol{k}) c_{\boldsymbol{k}+\boldsymbol{q}/2,ls}^\dagger c_{-\boldsymbol{k}+\boldsymbol{q}/2,l's'}^\dagger + \text{H.c.} \right] - \sum_{j=1,2} \frac{|\Delta_j|^2}{V_j}, \tag{G.3}$$

by introducing the superconducting order parameter

$$\Delta_j = V_j \sum_{\boldsymbol{k}} \sum_{ll',ss'} \varphi_{ls,l's'}^{j\dagger}(\boldsymbol{k}) \langle c_{-\boldsymbol{k}+\boldsymbol{q}/2,ls} c_{\boldsymbol{k}+\boldsymbol{q}/2,l's'} \rangle. \tag{G.4}$$

Then, a matrix form of the total Hamiltonian $\mathcal{H}$ is obtained as

$$\mathcal{H} = \frac{1}{2} \sum_{\boldsymbol{k}} (\hat{c}_{\boldsymbol{k}}^\dagger, \hat{c}_{-\boldsymbol{k}}^{\mathrm{T}}) \begin{pmatrix} H_0(\boldsymbol{k}+\boldsymbol{q}/2) & \Delta(\boldsymbol{k}) \\ \Delta^\dagger(\boldsymbol{k}) & -H_0^{\mathrm{T}}(-\boldsymbol{k}+\boldsymbol{q}/2) \end{pmatrix} \begin{pmatrix} \hat{c}_{\boldsymbol{k}} \\ \hat{c}_{-\boldsymbol{k}}^\dagger \end{pmatrix} - \sum_{j=1,2} \frac{|\Delta_j|^2}{V_j}, \tag{G.5}$$

where $\hat{c}_{\boldsymbol{k}}^{\mathrm{T}} = (c_{\boldsymbol{k}1\uparrow}, c_{\boldsymbol{k}1\downarrow}, c_{\boldsymbol{k}2\uparrow}, c_{\boldsymbol{k}2\downarrow})$ and some constants are omitted in Eq. (G.5). The pairing potential $\Delta(\boldsymbol{k})$ is given by

$$\Delta_{ls,l's'}(\boldsymbol{k}) = \sum_{j=1,2} \Delta_j \varphi_{ls,l's'}^j(\boldsymbol{k}). \tag{G.6}$$

To obtain the GL free energy for the $\mathcal{PT}$-symmetric mixed-parity superconducting states with the asymmetric Bogoliubov spectrum, we here assume that the pairing potentials are described as

$$\varphi^1(\boldsymbol{k}) = [r\eta_{\boldsymbol{k}}^b \gamma_b + (1-r)\eta_{\boldsymbol{k}}^a \gamma_a] U_T, \tag{G.7}$$

$$\varphi^2(\boldsymbol{k}) = \eta_{\boldsymbol{k}}^{ab} i \gamma_a \gamma_b U_T, \tag{G.8}$$

where a and b are integers satisfying $1 \le a < b \le 5$ and r takes the value either 0 or 1. In addition, we suppose that the normal state Hamiltonian $H_0(\boldsymbol{k})$ is described as

$$H_0(\boldsymbol{k}) = \xi_{\boldsymbol{k}} \mathbb{1}_4 + r\epsilon_{\boldsymbol{k}}^a \gamma_a + (1-r)\epsilon_{\boldsymbol{k}}^b \gamma_b. \tag{G.9}$$

Then, the model satisfies one of the necessary conditions for the asymmetric Bogoliubov spectrum, which is shown in Sec. 4.3. By assuming $|\xi_{\boldsymbol{k}}| \gg \max(|\epsilon_{\boldsymbol{k}}^{a,b}|)$, we can approximate Eq. (G.5) as

$$\mathcal{H} \approx \frac{1}{2} \sum_{\boldsymbol{k}} (\hat{c}_{\boldsymbol{k}}^\dagger, \hat{c}_{-\boldsymbol{k}}^{\mathrm{T}}) \begin{pmatrix} H_0(\boldsymbol{k}) + \frac{1}{2}\boldsymbol{v}_{\boldsymbol{k}} \cdot \boldsymbol{q} \mathbb{1}_4 & \Delta(\boldsymbol{k}) \\ \Delta^\dagger(\boldsymbol{k}) & -H_0^{\mathrm{T}}(-\boldsymbol{k}) + \frac{1}{2}\boldsymbol{v}_{\boldsymbol{k}} \cdot \boldsymbol{q} \mathbb{1}_4 \end{pmatrix} \begin{pmatrix} \hat{c}_{\boldsymbol{k}} \\ \hat{c}_{-\boldsymbol{k}}^\dagger \end{pmatrix} - \sum_{j=1,2} \frac{|\Delta_j|^2}{V_j}, \tag{G.10}$$

where $\boldsymbol{v}_{\boldsymbol{k}} = (v_{\boldsymbol{k}}^x, v_{\boldsymbol{k}}^y, v_{\boldsymbol{k}}^z) \equiv \nabla \xi_{\boldsymbol{k}}$ is the Fermi velocity. By diagonalizing the BdG Hamiltonian matrix in Eq. (G.10), we can obtain the free energy $\mathcal{F}$ as follows:

$$\mathcal{F} = -\frac{2}{\beta} \sum_{\boldsymbol{k}} \sum_{\sigma=\pm} \left[\ln\left(1 + e^{-\beta(E_{\boldsymbol{k}}^\sigma + \boldsymbol{v}_{\boldsymbol{k}} \cdot \boldsymbol{q}/2)}\right) + \ln\left(1 + e^{-\beta(-E_{-\boldsymbol{k}}^\sigma + \boldsymbol{v}_{\boldsymbol{k}} \cdot \boldsymbol{q}/2)}\right) \right] - \sum_{j=1,2} \frac{|\Delta_j|^2}{V_j}, \tag{G.11}$$

where $\beta = 1/T$ is the inverse temperature. The quasiparticle energy $E_{\boldsymbol{k}}^{\pm}$ is given by

$$E_{\boldsymbol{k}}^{\pm} = \sqrt{\xi_{\boldsymbol{k}}^2 + \frac{1}{4}\mathrm{Tr}\left[\Delta(\boldsymbol{k})\Delta^{\dagger}(\boldsymbol{k}) \pm \frac{M_{-}^{(1)}(\boldsymbol{k})\tilde{H}_0(\boldsymbol{k})}{r\epsilon_{\boldsymbol{k}}^a + (1-r)\epsilon_{\boldsymbol{k}}^b}\right]} \pm [r\epsilon_{\boldsymbol{k}}^a + (1-r)\epsilon_{\boldsymbol{k}}^b]. \tag{G.12}$$

By differentiating Eq. (G.11) with respect to Δ_j and Δ_j^*, we obtain an analytical expression of the GL free energy as

$$\begin{aligned} \mathcal{F} &= \alpha_1|\Delta_1|^2 + \alpha_2|\Delta_2|^2 + \beta_1|\Delta_1|^4 + \beta_2|\Delta_2|^4 + 4\tilde{\beta}|\Delta_1|^2|\Delta_2|^2 - \tilde{\beta}(\Delta_1^2\Delta_2^{*2} + \Delta_2^2\Delta_1^{*2}) \\ &+ \sum_{\nu=x,y,z} (\kappa_{1,\nu}|\Delta_1|^2 + \kappa_{2,\nu}|\Delta_2|^2)q_\nu^2 + \boldsymbol{T}\cdot\boldsymbol{q}. \end{aligned} \tag{G.13}$$

The coefficients of the quadratic terms are given by

$$\alpha_1 = \frac{1}{|V_1|} - 2\sum_{\boldsymbol{k}} |\eta_{\boldsymbol{k}}|^2\frac{1-2f(|\xi_{\boldsymbol{k}}|)}{|\xi_{\boldsymbol{k}}|} \approx \rho_0\langle|\eta_{\boldsymbol{k}}|^2\rangle_{\mathrm{FS}}\frac{T-T_{\mathrm{c},1}}{T_{\mathrm{c},1}}, \tag{G.14}$$

$$\alpha_2 = \frac{1}{|V_2|} - 2\sum_{\boldsymbol{k}} |\eta_{\boldsymbol{k}}^{ab}|^2\frac{1-2f(|\xi_{\boldsymbol{k}}|)}{|\xi_{\boldsymbol{k}}|} \approx \rho_0\langle|\eta_{\boldsymbol{k}}^{ab}|^2\rangle_{\mathrm{FS}}\frac{T-T_{\mathrm{c},2}}{T_{\mathrm{c},2}}, \tag{G.15}$$

where $|\eta_{\boldsymbol{k}}|^2 \equiv [r|\eta_{\boldsymbol{k}}^b|^2 + (1-r)|\eta_{\boldsymbol{k}}^a|^2]$, $f(x) = 1/(e^{\beta x}+1)$ is the Fermi-Dirac distribution function, ρ_0 is the density of states at the Fermi energy, and $\langle\cdots\rangle_{\mathrm{FS}}$ denotes the average over the Fermi surface. The superconducting transition temperature for the even-parity and odd-parity pairing channel $T_{\mathrm{c},1}$ and $T_{\mathrm{c},2}$ are defined as

$$T_{\mathrm{c},1} = \frac{2e^{\gamma}}{\pi}\epsilon_c\exp\left(-\frac{1}{\rho_0\langle|\eta_{\boldsymbol{k}}|^2\rangle_{\mathrm{FS}}|V_1|}\right), \tag{G.16}$$

$$T_{\mathrm{c},2} = \frac{2e^{\gamma}}{\pi}\epsilon_c\exp\left(-\frac{1}{\rho_0\langle|\eta_{\boldsymbol{k}}^{ab}|^2\rangle_{\mathrm{FS}}|V_2|}\right), \tag{G.17}$$

where $\gamma = 0.577\cdots$ is the Euler's constant, and ϵ_c is a cutoff energy. In Eqs. (G.14) and (G.15), the summation over $\boldsymbol{k}$ is approximated as

$$\sum_{\boldsymbol{k}} X(\boldsymbol{k})Y(\xi_{\boldsymbol{k}}) \approx \int_{\mathrm{FS}}\frac{dk_{\mathrm{F}}}{v(\boldsymbol{k}_{\mathrm{F}})}X(\boldsymbol{k}_{\mathrm{F}})\int_{-\epsilon_c}^{\epsilon_c}d\xi Y(\xi) \approx \frac{\rho_0}{4}\langle X(\boldsymbol{k}_{\mathrm{F}})\rangle_{\mathrm{FS}}\int_{-\epsilon_c}^{\epsilon_c}d\xi Y(\xi), \tag{G.18}$$

where X and Y are some functions, and $\boldsymbol{k}_{\mathrm{F}}$ is the Fermi wave vector. The coefficients of the

quartic terms are given by

$$\beta_1 = \frac{1}{2}\sum_{\boldsymbol{k}}|\boldsymbol{\eta}_{\boldsymbol{k}}|^4\left[\frac{1-2f(|\xi_{\boldsymbol{k}}|)}{|\xi_{\boldsymbol{k}}|^3}+\frac{2f'(|\xi_{\boldsymbol{k}}|)}{|\xi_{\boldsymbol{k}}|^2}\right]\approx\rho_0\langle|\boldsymbol{\eta}_{\boldsymbol{k}}|^4\rangle_{\text{FS}}\frac{7\zeta(3)}{16\pi^2T^2}, \tag{G.19}$$

$$\beta_2 = \frac{1}{2}\sum_{\boldsymbol{k}}|\eta_{\boldsymbol{k}}^{ab}|^4\left[\frac{1-2f(|\xi_{\boldsymbol{k}}|)}{|\xi_{\boldsymbol{k}}|^3}+\frac{2f'(|\xi_{\boldsymbol{k}}|)}{|\xi_{\boldsymbol{k}}|^2}\right]\approx\rho_0\langle|\eta_{\boldsymbol{k}}^{ab}|^4\rangle_{\text{FS}}\frac{7\zeta(3)}{16\pi^2T^2}, \tag{G.20}$$

$$\tilde{\beta} = \frac{1}{2}\sum_{\boldsymbol{k}}|\boldsymbol{\eta}_{\boldsymbol{k}}|^2|\eta_{\boldsymbol{k}}^{ab}|^2\left[\frac{1-2f(|\xi_{\boldsymbol{k}}|)}{|\xi_{\boldsymbol{k}}|^3}+\frac{2f'(|\xi_{\boldsymbol{k}}|)}{|\xi_{\boldsymbol{k}}|^2}\right]\approx\rho_0\langle|\boldsymbol{\eta}_{\boldsymbol{k}}|^2|\eta_{\boldsymbol{k}}^{ab}|^2\rangle_{\text{FS}}\frac{7\zeta(3)}{16\pi^2T^2}, \tag{G.21}$$

where $f'(x) = df(x)/dx$, and $\zeta(x)$ is the Riemann zeta function. In Eqs. (G.19)-(G.21), we used the following integral formula;

$$\int_{-\infty}^{\infty}d\xi\left[\frac{1-2f(\xi)}{\xi^3}+\frac{2f'(\xi)}{\xi^2}\right]=\int_{-\infty}^{\infty}d\xi\frac{f''(\xi)}{\xi}=\frac{7\zeta(3)}{2(\pi T)^2}, \tag{G.22}$$

where $f''(x) = df'(x)/dx$. The coefficients of the quadratic gradient term are obtained as

$$\kappa_{1,\nu} = \frac{1}{2}\sum_{\boldsymbol{k}}|\boldsymbol{\eta}_{\boldsymbol{k}}|^2|v_{\boldsymbol{k}}^{\nu}|^2\frac{f''(|\xi_{\boldsymbol{k}}|)}{|\xi_{\boldsymbol{k}}|}\approx\rho_0\langle|\boldsymbol{\eta}_{\boldsymbol{k}}|^2|v_{\boldsymbol{k}}^{\nu}|^2\rangle_{\text{FS}}\frac{7\zeta(3)}{16\pi^2T^2}, \tag{G.23}$$

$$\kappa_{2,\nu} = \frac{1}{2}\sum_{\boldsymbol{k}}|\eta_{\boldsymbol{k}}^{ab}|^2|v_{\boldsymbol{k}}^{\nu}|^2\frac{f''(|\xi_{\boldsymbol{k}}|)}{|\xi_{\boldsymbol{k}}|}\approx\rho_0\langle|\eta_{\boldsymbol{k}}^{ab}|^2|v_{\boldsymbol{k}}^{\nu}|^2\rangle_{\text{FS}}\frac{7\zeta(3)}{16\pi^2T^2}. \tag{G.24}$$

where we used Eq. (G.22). In the same manner, the effective anapole moment $\boldsymbol{T}$ is given by

$$\boldsymbol{T} = \frac{1}{2}\sum_{\boldsymbol{k}}\text{Tr}[M_-^{(1)}(\boldsymbol{k})\tilde{H}_0(\boldsymbol{k})]\boldsymbol{v}_{\boldsymbol{k}}\frac{f''(|\xi_{\boldsymbol{k}}|)}{|\xi_{\boldsymbol{k}}|}\approx\rho_0\langle\text{Tr}[M_-^{(1)}(\boldsymbol{k})\tilde{H}_0(\boldsymbol{k})]\boldsymbol{v}_{\boldsymbol{k}}\rangle_{\text{FS}}\frac{7\zeta(3)}{16\pi^2T^2}. \tag{G.25}$$

Appendix H

Symmetry analysis for UTe$_2$

In this appendix, we present a comprehensive symmetry analysis for possible asymmetric Bogoliubov spectrum and anapole superconductivity in UTe$_2$. Although we considered only the $A_g + iA_u$ and $A_g + iB_{3u}$ states in Sec. 4.4, we here consider all of possible $\mathcal{PT}$-symmetric mixed-parity pairing states in UTe$_2$. The superconducting order parameter in UTe$_2$ is classified based on the eight IRs in D_{2h} point group. The basis functions for these pairing states are shown in Table H.1. Since the local site symmetry at U site is C_{2v} in UTe$_2$ [202], the basis functions for the staggered pairing components can be obtained as listed in the third column of Table H.1. As shown in Sec. 4.4, the staggered pairing components and antisymmetric spin-orbit coupling are essential for the asymmetric Bogoliubov spectrum.

Table H.1. Basis functions for possible superconducting states in UTe$_2$. The second (third) column shows the basis function for intrasublattice (staggered) pairing components, which is proportional to τ_0 (τ_z). Here, τ_ν is the Pauli matrices for intra-ladder sublattice DOF in UTe$_2$ [202].

IR	Intrasublattice components ($\sim \tau_0$)	Staggered components ($\sim \tau_z$)
A_g	1	$k_y\hat{\boldsymbol{x}}, k_x\hat{\boldsymbol{y}}, k_xk_yk_z\hat{\boldsymbol{z}}$
B_{1g}	k_xk_y	$k_x\hat{\boldsymbol{x}}, k_y\hat{\boldsymbol{y}}, k_z\hat{\boldsymbol{z}}$
B_{2g}	k_zk_x	$k_xk_yk_z\hat{\boldsymbol{x}}, k_z\hat{\boldsymbol{y}}, k_y\hat{\boldsymbol{z}}$
B_{3g}	k_yk_z	$k_z\hat{\boldsymbol{x}}, k_xk_yk_z\hat{\boldsymbol{y}}, k_x\hat{\boldsymbol{z}}$
A_u	$k_x\hat{\boldsymbol{x}}, k_y\hat{\boldsymbol{y}}, k_z\hat{\boldsymbol{z}}$	k_xk_y
B_{1u}	$k_y\hat{\boldsymbol{x}}, k_x\hat{\boldsymbol{y}}, k_xk_yk_z\hat{\boldsymbol{z}}$	1
B_{2u}	$k_z\hat{\boldsymbol{x}}, k_xk_yk_z\hat{\boldsymbol{y}}, k_x\hat{\boldsymbol{z}}$	k_yk_z
B_{3u}	$k_xk_yk_z\hat{\boldsymbol{x}}, k_z\hat{\boldsymbol{y}}, k_y\hat{\boldsymbol{z}}$	k_zk_x

There are 16 patterns of $\mathcal{PT}$-symmetric mixed-parity pairing as shown in Table H.2. If the pairing state belongs to the nonpolar A_u^- IR, a nonpolar $k_xk_yk_z$-type asymmetry can be induced in the Bogoliubov spectrum. The A_u^- pairing states are equivalent to nonpolar odd-

Table H.2. List of possible $\mathcal{PT}$-symmetric mixed-parity pairing states in D_{2h} point group. For each pairing state, IR of the order parameter, corresponding multipole moment, type of asymmetric modulation in the Bogoliubov spectrum, and possible form of center-of-mass momentum of Cooper pairs $\boldsymbol{q}$ are shown. IRs with odd time-reversal parity are denoted by Γ^-. The anapole moment along the ν-axis is expressed as T_ν. On the other hand, M_0, M_2, M_4, ... denote nonpolar magnetic multipole moment, namely, the magnetic monopole, magnetic quadrupole, magnetic hexadecapole, ..., respectively.

Pairing state	IR	Multipole	Asymmetry	$\boldsymbol{q}$
$A_g + iA_u,\ B_{1g} + iB_{1u},\ B_{2g} + iB_{2u},\ B_{3g} + iB_{3u}$	A_u^-	$M_0,\ M_2,\ M_4,\ ...$	$k_x k_y k_z$	$(0,0,0)$
$A_g + iB_{1u},\ B_{1g} + iA_u,\ B_{2g} + iB_{3u},\ B_{3g} + iB_{2u}$	B_{1u}^-	T_z	k_z	$(0,0,q)$
$A_g + iB_{2u},\ B_{1g} + iB_{3u},\ B_{2g} + iA_u,\ B_{3g} + iB_{1u}$	B_{2u}^-	T_y	k_y	$(0,q,0)$
$A_g + iB_{3u},\ B_{1g} + iB_{2u},\ B_{2g} + iB_{1u},\ B_{3g} + iA_u$	B_{3u}^-	T_x	k_x	$(q,0,0)$

parity magnetic multipole states such as magnetic monopole, quadrupole, and hexadecapole, from the viewpoint of symmetry. On the other hand, if the pairing state belongs to the polar $B_{1u,2u,3u}^-$ IRs, the Bogoliubov spectrum can exhibit a polar $k_{z,y,x}$-type asymmetry. Thus, the $B_{1u,2u,3u}^-$ pairing state carries the anapole (magnetic toroidal) moment. This k_ν-type asymmetry leads to stabilization of FFLO state with $q_\nu \neq 0$ ($\nu = x, y, z$), where $\boldsymbol{q} = (q_x, q_y, q_z)$ is the center-of-mass momentum of Cooper pairs.

Bibliography

[1] J. Bardeen, L. N. Cooper, and J. R. Schrieffer, Phys. Rev. **108**, 1175 (1957).

[2] M. Z. Hasan and C. L. Kane, Rev. Mod. Phys. **82**, 3045 (2010).

[3] X.-g. Qi and S.-C. Zhang, Rev. Mod. Phys. **83**, 1057 (2011).

[4] C. Nayak, S. H. Simon, A. Stern, M. Freedman, and S. Das Sarma, Rev. Mod. Phys. **80**, 1083 (2008).

[5] E. Bauer and M. Sigrist, eds., *Noncentrosymmetric Superconductor: Introduction and Overview* (Springer, Berlin, 2012).

[6] M. Sato, Y. Takahashi, and S. Fujimoto, Phys. Rev. Lett. **103**, 020401 (2009).

[7] M. Sato, Y. Takahashi, and S. Fujimoto, Phys. Rev. B **82**, 134521 (2010).

[8] Y. Wang and L. Fu, Phys. Rev. Lett. **119**, 187003 (2017).

[9] S. Fujimoto, J. Phys. Soc. Jpn. **76**, 051008 (2007).

[10] P. A. Frigeri, D. F. Agterberg, A. Koga, and M. Sigrist, Phys. Rev. Lett. **92**, 097001 (2004).

[11] Y. Saito, Y. Nakamura, M. S. Bahramy, Y. Kohama, J. Ye, Y. Kasahara, Y. Nakagawa, M. Onga, M. Tokunaga, T. Nojima, Y. Yanase, and Y. Iwasa, Nat. Phys. **12**, 144 (2016).

[12] O. V. Dimitrova and M. V. Feigel'man, JETP Lett. **78**, 637 (2003).

[13] K. V. Samokhin, Phys. Rev. B **70**, 104521 (2004).

[14] D. F. Agterberg and R. P. Kaur, Phys. Rev. B **75**, 064511 (2007).

[15] T. Sekihara, R. Masutomi, and T. Okamoto, Phys. Rev. Lett. **111**, 057005 (2013).

[16] V. M. Edelstein, Phys. Rev. Lett. **75**, 2004 (1995).

[17] V. M. Edelstein, Phys. Rev. B **67**, 020505(R) (2003).

[18] S. K. Yip, Phys. Rev. B **65**, 144508 (2002).

[19] S. Fujimoto, Phys. Rev. B **72**, 024515 (2005).

[20] J. J. He, K. Hiroki, K. Hamamoto, and N. Nagaosa, Communications Physics **2**, 128 (2019).

[21] W.-Y. He and K. T. Law, Phys. Rev. Research **2**, 012073(R) (2020).

[22] Y. Ikeda and Y. Yanase, Phys. Rev. B **102**, 214510 (2020).

[23] F. Ando, Y. Miyasaka, T. Li, J. Ishizuka, T. Arakawa, Y. Shiota, T. Moriyama, Y. Yanase, and T. Ono, Nature **584**, 373 (2020).

[24] Y.-Y. Lyu, J. Jiang, Y.-L. Wang, Z.-L. Xiao, S. Dong, Q.-H. Chen, M. V. Milošević, H. Wang, R. Divan, J. E. Pearson, P. Wu, F. M. Peeters, and W.-K. Kwok, Nat. Commun. **12**, 2703 (2021).

[25] C. Baumgartner, L. Fuchs, A. Costa, S. Reinhardt, S. Gronin, G. C. Gardner, T. Lindemann, M. J. Manfra, P. E. Faria Junior, D. Kochan, J. Fabian, N. Paradiso, and C. Strunk, Nat. Nanotech. (2021).

[26] N. F. Yuan and L. Fu, arXiv:2106.01909 (2021).

[27] A. Daido, Y. Ikeda, and Y. Yanase, arXiv:2106.03326 (2021).

[28] J. J. He, Y. Tanaka, and N. Nagaosa, arXiv:2106.03575 (2021).

[29] A. Ramires and M. Sigrist, Phys. Rev. B **94**, 104501 (2016).

[30] A. Ramires, D. F. Agterberg, and M. Sigrist, Phys. Rev. B **98**, 024501 (2018).

[31] M. H. Fischer, F. Loder, and M. Sigrist, Phys. Rev. B **84**, 184533 (2011).

[32] T. Yoshida, M. Sigrist, and Y. Yanase, Phys. Rev. B **86**, 134514 (2012).

[33] Y. Nakamura and Y. Yanase, Phys. Rev. B **96**, 054501 (2017).

[34] T. Yoshida, M. Sigrist, and Y. Yanase, J. Phys. Soc. Jpn. **82**, 074714 (2013).

[35] S. Nakosai, Y. Tanaka, and N. Nagaosa, Phys. Rev. Lett. **108**, 147003 (2012).

[36] T. Yoshida, M. Sigrist, and Y. Yanase, Phys. Rev. Lett. **115**, 027001 (2015).

[37] T. Yoshida, A. Daido, Y. Yanase, and N. Kawakami, Phys. Rev. Lett. **118**, 147001 (2017).

[38] J. Ishizuka and Y. Yanase, Phys. Rev. B **98**, 224510 (2018).

[39] K. Miyake, S. Schmitt-Rink, and C. M. Varma, Phys. Rev. B **34**, 6554(R) (1986).

[40] T. Moriya and K. Ueda, Advances in Physics **49**, 555 (2000).

[41] Y. Yanase, T. Jujo, T. Nomura, H. Ikeda, T. Hotta, and K. Yamada, Physics Reports **387**, 1 (2003).

[42] D. Aoki, K. Ishida, and J. Flouquet, J. Phys. Soc. Jpn. **88**, 022001 (2019).

[43] Y. Yanagi, Y. Yamakawa, and Y. Ōno, Phys. Rev. B **81**, 054518 (2010).

[44] H. Kontani and S. Onari, Phys. Rev. Lett. **104**, 157001 (2010).

[45] F. Yu, D. Ma, W. Zhuo, S. Liu, X. Wen, B. Lei, J. Ying, and X. Chen, Nat. Commun. **12**, 3645 (2021).

[46] R. Tazai, Y. Yamakawa, S. Onari, and H. Kontani, arXiv:2107.05372 (2021).

[47] Y.-P. Lin and R. M. Nandkishore, arXiv:2107.09050 (2021).

[48] V. Kozii and L. Fu, Phys. Rev. Lett. **115**, 207002 (2015).

[49] L. Fu, Phys. Rev. Lett. **115**, 026401 (2015).

[50] S. Sumita and Y. Yanase, Phys. Rev. Research **2**, 033225 (2020).

[51] M. N. Gastiasoro, T. V. Trevisan, and R. M. Fernandes, Phys. Rev. B **101**, 174501 (2020).

[52] M. Lee, H.-J. Lee, J. H. Lee, and S. B. Chung, Phys. Rev. Materials **4**, 034202 (2020).

[53] M. N. Gastiasoro, M. E. Temperini, P. Barone, and J. Lorenzana, arXiv:2109.13207 (2021).

[54] Y. Yu, H. Y. Hwang, S. Raghu, and S. B. Chung, arXiv:2110.03710 (2021).

[55] S. Sumita and Y. Yanase, Phys. Rev. B **93**, 224507 (2016).

[56] S. Sumita, T. Nomoto, and Y. Yanase, Phys. Rev. Lett. **119**, 027001 (2017).

[57] S. Kanasugi and Y. Yanase, Phys. Rev. B **98**, 024521 (2018).

[58] C. W. Rischau, X. Lin, C. P. Grams, D. Finck, S. Harms, J. Engelmayer, T. Lorenz, Y. Gallais, B. Fauque, J. Hemberger, and K. Behnia, Nat. Phys. **13**, 643 (2017).

[59] R. Russell, N. Ratcliff, K. Ahadi, L. Dong, S. Stemmer, and J. W. Harter, Phys. Rev. Materials **3**, 091401 (2019).

[60] Z. Hiroi, J. Yamaura, T. C. Kobayashi, Y. Matsubayashi, and D. Hirai, J. Phys. Soc. Jpn. **87**, 024702 (2017).

[61] J.-i. Yamaura, K. Takeda, Y. Ikeda, N. Hirao, Y. Ohishi, T. C. Kobayashi, and Z. Hiroi, Phys. Rev. B **95**, 020102(R) (2017).

[62] I. A. Sergienko, Phys. Rev. B **69**, 174502 (2004).

[63] W. Yang, C. Xu, and C. Wu, Phys. Rev. Research **2**, 042047(R) (2020).

[64] Y. Shi, Y. Guo, X. Wang, A. J. Princep, D. Khalyavin, P. Manuel, Y. Michiue, A. Sato, K. Tsuda, S. Yu, M. Arai, Y. Shirako, M. Akaogi, N. Wang, K. Yamaura, and A. T. Boothroyd, Nat. Mater. **12**, 1024 (2013).

[65] Z. Fei, W. Zhao, T. A. Palomaki, B. Sun, M. K. Miller, Z. Zhao, J. Yan, X. Xu, and D. H. Cobden, Nature **560**, 336 (2018).

[66] P. Sharma, F.-X. Xiang, D.-F. Shao, D. Zhang, E. Y. Tsymbal, A. R. Hamilton, and J. Seidel, Sci. Adv. **5**, eaax5080 (2019).

[67] X. Lin, Z. Zhu, B. Fauqué, and K. Behnia, Phys. Rev. X **3**, 021002 (2013).

[68] X. Lin, G. Bridoux, A. Gourgout, G. Seyfarth, S. Krämer, M. Nardone, B. Fauqué, and K. Behnia, Phys. Rev. Lett. **112**, 207002 (2014).

[69] T. M. Bretz-Sullivan, A. Edelman, J. Jiang, A. Suslov, D. Graf, J. Zhang, G. Wang, C. Chang, J. E. Pearson, A. B. Martinson, P. B. Littlewood, and A. Bhattacharya, arXiv:1904.03121 (2019).

[70] Y. Takada, J. Phys. Soc. Jpn. **49**, 1267 (1980).

[71] J. Ruhman and P. A. Lee, Phys. Rev. B **94**, 224515 (2016).

[72] L. P. Gor'kov, Proc. Natl Acad. Sci. USA **113**, 4646 (2016).

[73] L. P. Gor'kov, Journal of Superconductivity and Novel Magnetism **30**, 845 (2017).

[74] K. A. Müller and H. Burkard, Phys. Rev. B **19**, 3593 (1979).

[75] S. Rowley, L. Spalek, R. Smith, M. Dean, M. Itoh, J. Scott, G. Lonzarich, and S. Saxena, Nat. Phys. **10**, 367 (2014).

[76] J. G. Bednorz and K. A. Müller, Phys. Rev. Lett. **52**, 2289 (1984).

[77] M. Itoh, R. Wang, Y. Inaguma, T. Yamaguchi, Y.-J. Shan, and T. Nakamura, Phys. Rev. Lett. **82**, 3540 (1999).

[78] H. Uwe and T. Sakudo, Phys. Rev. B **13**, 271 (1976).

[79] J. Hemberger, P. Lunkenheimer, R. Viana, R. Böhmer, and A. Loidl, Phys. Rev. B **52**, 13159 (1995).

[80] J. M. Edge, Y. Kedem, U. Aschauer, N. A. Spaldin, and A. V. Balatsky, Phys. Rev. Lett. **115**, 247002 (2015).

[81] K. Dunnett, A. Narayan, N. A. Spaldin, and A. V. Balatsky, Phys. Rev. B **97**, 144506 (2018).

[82] P. Wölfle and A. V. Balatsky, Phys. Rev. B **98**, 104505 (2018).

[83] J. R. Arce-Gamboa and G. G. Guzmán-Verri, Phys. Rev. Materials **2**, 104804 (2018).

[84] Y. Kedem, Phys. Rev. B **98**, 220505(R) (2018).

[85] D. van der Marel, F. Barantani, and C. W. Rischau, Phys. Rev. Research **1**, 013003 (2019).

[86] A. Stucky, G. Scheerer, Z. Ren, D. Jaccard, J.-M. Poumirol, C. Barreteau, E. Giannini, and D. van der Marel, Sci. Rep. **6**, 37582 (2016).

[87] Y. Tomioka, N. Shirakawa, K. Shibuya, and I. H. Inoue, Nat. Commun. **10**, 738 (2019).

[88] C. Herrera, J. Cerbin, A. Jayakody, K. Dunnett, A. V. Balatsky, and I. Sochnikov, Phys. Rev. Materials **3**, 124801 (2019).

[89] K. Ahadi, L. Galletti, Y. Li, S. Salmani-Rezaie, W. Wu, and S. Stemmer, Sci. Adv. **5**, eaaw0120 (2019).

[90] V. Kozii, A. Klein, R. M. Fernandes, and J. Ruhman, arXiv:2110.09530 (2021).

[91] S. A. Hayward and E. K. H. Salje, Phase Transitions **68**, 501 (1999).

[92] G. Binnig, A. Baratoff, H. E. Hoenig, and J. G. Bednorz, Phys. Rev. Lett. **45**, 1352 (1980).

[93] X. Lin, A. Gourgout, G. Bridoux, F. Jomard, A. Pourret, B. Fauqué, D. Aoki, and K. Behnia, Phys. Rev. B **90**, 140508 (2014).

[94] R. M. Fernandes, J. T. Haraldsen, P. Wölfle, and A. V. Balatsky, Phys. Rev. B **87**, 014510 (2013).

[95] J. M. Edge and A. V. Balatsky, Journal of Superconductivity and Novel Magnetism **28**, 2373 (2015).

[96] T. V. Trevisan, M. Schütt, and R. M. Fernandes, Phys. Rev. Lett. **121**, 127002 (2018).

[97] A. G. Swartz, H. Inoue, T. A. Merz, Y. Hikita, S. Raghu, T. P. Devereaux, S. Johnston, and H. Y. Hwang, Proceedings of the National Academy of Sciences **115**, 1475 (2018).

[98] M. Thiemann, M. H. Beutel, M. Dressel, N. R. Lee-Hone, D. M. Broun, E. Fillis-Tsirakis, H. Boschker, J. Mannhart, and M. Scheffler, Phys. Rev. Lett. **120**, 237002 (2018).

[99] R. E. Cohen, Nature **358**, 136 (1992).

[100] Y. Yanase, J. Phys. Soc. Jpn. **82**, 044711 (2013).

[101] M. Hirayama, T. Miyake, and M. Imada, J. Phys. Soc. Jpn. **81**, 084708 (2012).

[102] G. Khalsa and A. H. MacDonald, Phys. Rev. B **86**, 125121 (2012).

[103] Z. Zhong, A. Tóth, and K. Held, Phys. Rev. B **87**, 161102(R) (2013).

[104] U. Aschauer and N. A. Spaldin, Journal of Physics: Condensed Matter **26**, 122203 (2014).

[105] Y. Watanabe, Computational Materials Science **158**, 315 (2019).

[106] Y. Yanase and M. Sigrist, J. Phys. Soc. Jpn. **76**, 124709 (2007).

[107] H. Yoon, A. G. Swartz, S. P. Harvey, H. Inoue, Y. Hikita, Y. Yu, S. B. Chung, S. Raghu, and H. Y. Hwang, arXiv:2106.10802 (2021).

[108] C. Collignon, X. Lin, C. W. Rischau, B. Fauqué, and K. Behnia, Annual Review of Condensed Matter Physics **10**, 25 (2019).

[109] Y. Ayino, J. Yue, T. Wang, B. Jalan, and V. S. Pribiag, Journal of Physics: Condensed Matter **32**, 38LT02 (2020).

[110] R. A. Cowley, Advances in Physics **29**, 1 (1980).

[111] V. M. Edelstein, Sov. Phys. JETP **68**, 1244 (1989).

[112] S. Fujimoto, J. Phys. Soc. Jpn. **76**, 034712 (2007).

[113] E. Cappelluti, C. Grimaldi, and F. Marsiglio, Phys. Rev. Lett. **98**, 167002 (2007).

[114] D. J. Thouless, M. Kohmoto, M. P. Nightingale, and M. den Nijs, Phys. Rev. Lett. **49**, 405 (1982).

[115] M. Kohmoto, Annals of Physics **160**, 343 (1985).

[116] T. Fukui, Y. Hatsugai, and H. Suzuki, J. Phys. Soc. Jpn. **74**, 1674 (2005).

[117] H. Sumiyoshi and S. Fujimoto, J. Phys. Soc. Jpn. **82**, 023602 (2013).

[118] A. Balatsky and E. Abrahams, Phys. Rev. B **45**, 13125 (1992).

[119] A. M. Black-Schaffer and A. V. Balatsky, Phys. Rev. B **88**, 104514 (2013).

[120] T. Nomoto, K. Hattori, and H. Ikeda, Phys. Rev. B **94**, 174513 (2016).

[121] S.-O. Kaba and D. Sénéchal, Phys. Rev. B **100**, 214507 (2019).

[122] R. M. Geilhufe and A. V. Balatsky, Phys. Rev. B **97**, 024507 (2018).

[123] M. Sato, Phys. Rev. B **79**, 214526 (2009).

[124] M. Sato, Phys. Rev. B **81**, 220504(R) (2010).

[125] L. Fu and E. Berg, Phys. Rev. Lett. **105**, 097001 (2010).

[126] T. M. Rice and M. Sigrist, Journal of Physics: Condensed Matter **7**, L643 (1995).

[127] A. P. Mackenzie and Y. Maeno, Rev. Mod. Phys. **75**, 657 (2003).

[128] J. A. Sauls, Adv. Phys. **43**, 113 (1994).

[129] H. Tou, Y. Kitaoka, K. Ishida, K. Asayama, N. Kimura, Y. Onuki, E. Yamamoto, Y. Haga, and K. Maezawa, Phys. Rev. Lett. **80**, 3129 (1998).

[130] R. Joynt and L. Taillefer, Rev. Mod. Phys. **74**, 235 (2002).

[131] S. S. Saxena, P. Agarwal, K. Ahilan, F. M. Grosche, R. Haselwimmer, M. J. Steiner, E. Pugh, I. R. Walker, S. R. Julian, P. Monthoux, G. G. Lonzarich, A. Huxley, I. Sheikin, D. Braithwaite, and J. Flouquet, Nature **406**, 587 (2000).

[132] D. Aoki, A. Huxley, E. Ressouche, D. Braithwaite, J. Flouquet, J.-P. Brison, E. Lhotel, and C. Paulsen, Nature **413**, 613 (2001).

[133] N. T. Huy, A. Gasparini, D. E. de Nijs, Y. Huang, J. C. P. Klaasse, T. Gortenmulder, A. de Visser, A. Hamann, T. Görlach, and H. v. Löhneysen, Phys. Rev. Lett. **99**, 067006 (2007).

[134] S. Ran, C. Eckberg, Q. P. Ding, Y. Furukawa, T. Metz, S. R. Saha, I. L. Liu, M. Zic, H. Kim, J. Paglione, and N. P. Butch, Science **365**, 684 (2019).

[135] D. Aoki, A. Nakamura, F. Honda, D. X. Li, Y. Homma, Y. Shimizu, Y. J. Sato, G. Knebel, J. P. Brison, A. Pourret, D. Braithwaite, G. Lapertot, Q. Niu, M. Vališka, H. Harima, and J. Flouquet, J. Phys. Soc. Jpn. **88**, 043702 (2019).

[136] S. Yonezawa, T. Kajikawa, and Y. Maeno, J. Phys. Soc. Jpn. **83**, 083706 (2014).

[137] S. Kittaka, A. Kasahara, T. Sakakibara, D. Shibata, S. Yonezawa, Y. Maeno, K. Tenya, and K. Machida, Phys. Rev. B **90**, 220502(R) (2014).

[138] A. Pustogow, Y. Luo, A. Chronister, Y.-S. Su, D. A. Sokolov, F. Jerzembeck, A. P. Mackenzie, C. W. Hicks, N. Kikugawa, S. Raghu, E. D. Bauer, and S. E. Brown, Nature **574**, 72 (2019).

[139] K. Ishida, M. Manago, K. Kinjo, and Y. Maeno, J. Phys. Soc. Jpn. **89**, 034712 (2020).

[140] H. Yao and F. Yang, Phys. Rev. B **92**, 035132 (2015).

[141] Z. Y. Meng, F. Yang, K.-S. Chen, H. Yao, and H.-Y. Kee, Phys. Rev. B **91**, 184509 (2015).

[142] X. Wu, M. Fink, W. Hanke, R. Thomale, and D. Di Sante, Phys. Rev. B **100**, 041117(R) (2019).

[143] K. Kuroki, R. Arita, and H. Aoki, Phys. Rev. B **63**, 094509 (2001).

[144] K. Kuroki and R. Arita, Phys. Rev. B **63**, 174507 (2001).

[145] Y. Tanaka and K. Kuroki, Phys. Rev. B **70**, 060502(R) (2004).

[146] K. Kuroki and Y. Tanaka, J. Phys. Soc. Jpn. **74**, 1694 (2005).

[147] J. C. Nickel, R. Duprat, C. Bourbonnais, and N. Dupuis, Phys. Rev. Lett. **95**, 247001 (2005).

[148] Y. Fuseya and Y. Suzumura, J. Phys. Soc. Jpn. **74**, 1263 (2005).

[149] K. Kuroki, Y. Tanaka, and R. Arita, Phys. Rev. Lett. **93**, 077001 (2004).

[150] K. Kuroki, Y. Tanaka, and R. Arita, Phys. Rev. B **71**, 024506 (2005).

[151] H. Ikeda, Y. Nisikawa, and K. Yamada, J. Phys. Soc. Jpn. **73**, 17 (2004).

[152] Y. Tanaka, Y. Yanase, and M. Ogata, J. Phys. Soc. Jpn. **73**, 319 (2004).

[153] Y. Nisikawa, H. Ikeda, and K. Yamada, J. Phys. Soc. Jpn. **73**, 1127 (2004).

[154] Y. Yanase, M. Mochizuki, and M. Ogata, J. Phys. Soc. Jpn. **74**, 430 (2005).

[155] Y. Yanase, M. Mochizuki, and M. Ogata, J. Phys. Soc. Jpn. **74**, 2568 (2005).

[156] I. Mazin and M. Johannes, Nat. Phys. **1**, 91 (2005).

[157] M. Mochizuki, Y. Yanase, and M. Ogata, Phys. Rev. Lett. **94**, 147005 (2005).

[158] J. Goryo, M. H. Fischer, and M. Sigrist, Phys. Rev. B **86**, 100507(R) (2012).

[159] W.-S. Wang, Y. Yang, and Q.-H. Wang, Phys. Rev. B **90**, 094514 (2014).

[160] Y. Fukaya, K. Yada, A. Hattori, and Y. Tanaka, J. Phys. Soc. Jpn. **85**, 104704 (2016).

[161] G.-q. Zheng, K. Matano, D. P. Chen, and C. T. Lin, Phys. Rev. B **73**, 180503(R) (2006).

[162] K. Matano, G.-Q. Zheng, D. Chen, and C. Lin, Physica B: Condensed Matter **403**, 1107 (2008).

[163] M. Sigrist and K. Ueda, Rev. Mod. Phys. **63**, 239 (1991).

[164] M. Sigrist, D. F. Agterberg, M. H. Fischer, J. Goryo, F. Loder, S.-H. Rhim, D. Maruyama, Y. Yanase, T. Yoshida, and S. J. Youn, J. Phys. Soc. Jpn. **83**, 061014 (2014).

[165] D. Maruyama, M. Sigrist, and Y. Yanase, J. Phys. Soc. Jpn. **81**, 034702 (2012).

[166] J. A. Wilson and A. Yoffe, Adv. Phys. **18**, 193 (1969).

[167] G.-B. Liu, D. Xiao, Y. Yao, X. Xu, and W. Yao, Chem. Soc. Rev. **44**, 2643 (2015).

[168] M. Bonilla, S. Kolekar, Y. Ma, H. C. Diaz, V. Kalappattil, R. Das, T. Eggers, H. R. Gutierrez, M.-H. Phan, and M. Batzill, Nat. Nanotech. **13**, 289 (2018).

[169] D. J. O'Hara, T. Zhu, A. H. Trout, A. S. Ahmed, Y. K. Luo, C. H. Lee, M. R. Brenner, S. Rajan, J. A. Gupta, D. W. McComb, and R. K. Kawakami, Nano Lett. **18**, 3125 (2018).

[170] R. Roldán, E. Cappelluti, and F. Guinea, Phys. Rev. B **88**, 054515 (2013).

[171] N. F. Q. Yuan, K. F. Mak, and K. T. Law, Phys. Rev. Lett. **113**, 097001 (2014).

[172] J. Yuan and C. Honerkamp, arXiv:1504.04536 (2015).

[173] Y.-T. Hsu, A. Vaezi, M. H. Fischer, and E.-A. Kim, Nat. Commun. **8**, 14985 (2017).

[174] A. K. Nayak, A. Steinbok, Y. Roet, J. Koo, G. Margalit, I. Feldman, A. Almoalem, A. Kanigel, G. A. Fiete, B. Yan, Y. Oreg, and N. Avraham, Nat. Phys. (2021).

[175] O. Zheliuk, J. Lu, Q. Chen, A. El Yumin, S. Golightly, and J. Ye, Nat. Nanotech. **14**, 1123 (2019).

[176] R. Akashi, M. Ochi, S. Bordács, R. Suzuki, Y. Tokura, Y. Iwasa, and R. Arita, Phys. Rev. Applied **4**, 014002 (2015).

[177] R. Akashi, Y. Iida, K. Yamamoto, and K. Yoshizawa, Phys. Rev. B **95**, 245401 (2017).

[178] A. T. Rømer, T. A. Maier, A. Kreisel, I. Eremin, P. J. Hirschfeld, and B. M. Andersen, Phys. Rev. Research **2**, 013108 (2020).

[179] D. Costanzo, S. Jo, H. Berger, and A. F. Morpurgo, Nat. Nanotech. **11**, 339 (2016).

[180] Y. Ge and A. Y. Liu, Phys. Rev. B **87**, 241408(R) (2013).

[181] M. Rösner, S. Haas, and T. O. Wehling, Phys. Rev. B **90**, 245105 (2014).

[182] T. Das and K. Dolui, Phys. Rev. B **91**, 094510 (2015).

[183] D. Costanzo, H. Zhang, B. A. Reddy, H. Berger, and A. F. Morpurgo, Nat. Nanotech. **13**, 483 (2018).

[184] K. S. Burch, D. Mandrus, and J.-G. Park, Nature **563**, 47 (2018).

[185] B. Huang, G. Clark, E. Navarro-Moratalla, D. R. Klein, R. Cheng, K. L. Seyler, D. Zhong, E. Schmidgall, M. A. McGuire, D. H. Cobden, W. Yao, D. Xiao, P. Jarillo-Herrero, and X. Xu, Nature **546**, 270 (2017).

[186] C. Gong, L. Li, Z. Li, H. Ji, A. Stern, Y. Xia, T. Cao, W. Bao, C. Wang, Y. Wang, Z. Q. Qiu, R. J. Cava, S. G. Louie, J. Xia, and X. Zhang, Nature **546**, 265 (2017).

[187] M. Nakano, Y. Wang, S. Yoshida, H. Matsuoka, Y. Majima, K. Ikeda, Y. Hirata, Y. Takeda, H. Wadati, Y. Kohama, Y. Ohigashi, M. Sakano, K. Ishizaka, and Y. Iwasa, Nano Lett. **19**, 8806 (2019).

[188] A. J. Leggett, Rev. Mod. Phys. **47**, 331 (1975).

[189] E. Taylor and C. Kallin, Phys. Rev. Lett. **108**, 157001 (2012).

[190] M. Smidman, M. B. Salamon, H. Q. Yuan, and D. F. Agterberg, Rep. Prog. Phys. **80**, 036501 (2017).

[191] C. Wu and J. E. Hirsch, Phys. Rev. B **81**, 020508(R) (2010).

[192] L. H. Zhou, W. Yi, and X. L. Cui, Sci. China Phys. Mech. Astron. **60**, 127011 (2017).

[193] Z. Hiroi, J. Yamaura, T. C. Kobayashi, Y. Matsubayashi, and D. Hirai, J. Phys. Soc. Jpn. **87**, 024702 (2018).

[194] T. Schumann, L. Galletti, H. Jeong, K. Ahadi, W. M. Strickland, S. Salmani-Rezaie, and S. Stemmer, Phys. Rev. B **101**, 100503(R) (2020).

[195] S. Ryu, J. E. Moore, and A. W. W. Ludwig, Phys. Rev. B **85**, 045104 (2012).

[196] X.-g. Qi, E. Witten, and S.-C. Zhang, Phys. Rev. B **87**, 134519 (2013).

[197] P. Goswami and B. Roy, Phys. Rev. B **90**, 041301(R) (2014).

[198] K. Shiozaki and S. Fujimoto, Phys. Rev. B **89**, 054506 (2014).

[199] B. Roy, Phys. Rev. B **101**, 220506(R) (2020).

[200] C. Xu and W. Yang, arXiv:2009.12998 (2020).

[201] T. Scaffidi, arXiv:2007.13769 (2020).

[202] J. Ishizuka and Y. Yanase, Phys. Rev. B **103**, 094504 (2021).

[203] D. Braithwaite, M. Vališka, G. Knebel, G. Lapertot, J. P. Brison, A. Pourret, M. E. Zhitomirsky, J. Flouquet, F. Honda, and D. Aoki, Communications Physics **2**, 147 (2019).

[204] W. C. Lin, D. J. Campbell, S. Ran, I. L. Liu, H. Kim, A. H. Nevidomskyy, D. Graf, N. P. Butch, and J. Paglione, npj Quantum Materials **5**, 68 (2020).

[205] D. Aoki, F. Honda, G. Knebel, D. Braithwaite, A. Nakamura, D. Li, Y. Homma, Y. Shimizu, Y. J. Sato, J.-P. Brison, and J. Flouquet, J. Phys. Soc. Jpn. **89**, 053705 (2020).

[206] D. Aoki, M. Kimata, Y. J. Sato, G. Knebel, F. Honda, A. Nakamura, D. Li, Y. Homma, Y. Shimizu, W. Knafo, D. Braithwaite, M. Vališka, A. Pourret, J.-P. Brison, and J. Flouquet, J. Phys. Soc. Jpn. **90**, 074705 (2021).

[207] Z. Wang, J. Berlinsky, G. Zwicknagl, and C. Kallin, Phys. Rev. B **96**, 174511 (2017).

[208] P. M. R. Brydon, D. S. L. Abergel, D. F. Agterberg, and V. M. Yakovenko, Phys. Rev. X **9**, 031025 (2019).

[209] M. D. E. Denys and P. M. R. Brydon, Phys. Rev. B **103**, 094503 (2021).

[210] C. Triola and A. M. Black-Schaffer, Phys. Rev. B **97**, 064505 (2018).

[211] D. F. Agterberg, P. M. R. Brydon, and C. Timm, Phys. Rev. Lett. **118**, 127001 (2017).

[212] P. M. R. Brydon, D. F. Agterberg, H. Menke, and C. Timm, Phys. Rev. B **98**, 224509 (2018).

[213] P. Fulde and R. A. Ferrell, Phys. Rev. **135**, A550 (1964).

[214] A. I. Larkin and Y. N. Ovchinnikov, Zh. Eksp. Teor. Fiz. **47**, 1136 (1964), [translation: Sov. Phys. JETP **20**, 762 (1965)].

[215] V. P. Mineev and K. V. Samokhin, Phys. Rev. B **78**, 144503 (2008).

[216] N. A. Spaldin, M. Fiebig, and M. Mostovoy, Journal of Physics: Condensed Matter **20**, 434203 (2008).

[217] V. V. Flambaum, I. B. Khriplovich, and O. P. Sushkov, Physics Letters B **146**, 367 (1984).

[218] J. Jeong, Y. Sidis, A. Louat, V. Brouet, and P. Bourges, Nat. Commun. **8**, 15119 (2017).

[219] H. Murayama, K. Ishida, R. Kurihara, T. Ono, Y. Sato, Y. Kasahara, H. Watanabe, Y. Yanase, G. Cao, Y. Mizukami, T. Shibauchi, Y. Matsuda, and S. Kasahara, Phys. Rev. X **11**, 011021 (2021).

[220] H. Watanabe and Y. Yanase, Phys. Rev. X **11**, 011001 (2021).

[221] J. Ahn, G.-Y. Guo, and N. Nagaosa, Phys. Rev. X **10**, 041041 (2020).

[222] C. Timm, P. M. R. Brydon, and D. F. Agterberg, Phys. Rev. B **103**, 024521 (2021).

[223] S. Ran, H. Kim, I. L. Liu, S. R. Saha, I. Hayes, T. Metz, Y. S. Eo, J. Paglione, and N. P. Butch, Phys. Rev. B **101**, 140503(R) (2020).

[224] G. Knebel, M. Kimata, M. Vališka, F. Honda, D. Li, D. Braithwaite, G. Lapertot, W. Knafo, A. Pourret, Y. J. Sato, Y. Shimizu, T. Kihara, J.-P. Brison, J. Flouquet, and D. Aoki, J. Phys. Soc. Jpn. **89**, 053707 (2020).

[225] S. M. Thomas, F. B. Santos, M. H. Christensen, T. Asaba, F. Ronning, J. D. Thompson, E. D. Bauer, R. M. Fernandes, G. Fabbris, and P. F. Rosa, Sci. Adv. **6**, eabc8709 (2020).

[226] S. M. Thomas, C. Stevens, F. B. Santos, S. S. Fender, E. D. Bauer, F. Ronning, J. D. Thompson, A. Huxley, and P. F. S. Rosa, arXiv:2103.09194 (2021).

[227] L. Jiao, S. Howard, S. Ran, Z. Wang, J. O. Rodriguez, M. Sigrist, Z. Wang, N. P. Butch, and V. Madhavan, Nature **579**, 523 (2020).

[228] I. M. Hayes, D. S. Wei, T. Metz, J. Zhang, Y. S. Eo, S. Ran, S. R. Saha, J. Collini, N. P. Butch, D. F. Agterberg, A. Kapitulnik, and J. Paglione, arXiv:2002.02539 (2020).

[229] K. Ishihara, M. Roppongi, M. Kobayashi, Y. Mizukami, H. Sakai, Y. Haga, K. Hashimoto, and T. Shibauchi, arXiv:2105.13721 (2021).

[230] I. M. Hayes, D. S. Wei, T. Metz, J. Zhang, Y. S. Eo, S. Ran, S. R. Saha, J. Collini, N. P. Butch, D. F. Agterberg, A. Kapitulnik, and J. Paglione, Science **373**, 797 (2021).

[231] Y. Yanase, J. Phys. Soc. Jpn. **83**, 014703 (2014).

[232] S. Hayami, H. Kusunose, and Y. Motome, Phys. Rev. B **90**, 024432 (2014).

[233] G. L. J. A. Rikken, J. Fölling, and P. Wyder, Phys. Rev. Lett. **87**, 236602 (2001).

[234] H. Watanabe and Y. Yanase, Phys. Rev. B **96**, 064432 (2017).

[235] Y. Shiomi, H. Watanabe, H. Masuda, H. Takahashi, Y. Yanase, and S. Ishiwata, Phys. Rev. Lett. **122**, 127207 (2019).

[236] M. Chazono, H. Watanabe, and Y. Yanase, arXiv:2109.03461 (2021).

[237] Y. Tokunaga, H. Sakai, S. Kambe, T. Hattori, N. Higa, G. Nakamine, S. Kitagawa, K. Ishida, A. Nakamura, Y. Shimizu, Y. Homma, D. X. Li, F. Honda, and D. Aoki, J. Phys. Soc. Jpn. **88**, 073701 (2019).

[238] S. Sundar, S. Gheidi, K. Akintola, A. M. Côté, S. R. Dunsiger, S. Ran, N. P. Butch, S. R. Saha, J. Paglione, and J. E. Sonier, Phys. Rev. B **100**, 140502(R) (2019).

[239] G. Knebel, W. Knafo, A. Pourret, Q. Niu, M. Vališka, D. Braithwaite, G. Lapertot, M. Nardone, A. Zitouni, S. Mishra, I. Sheikin, G. Seyfarth, J. P. Brison, D. Aoki, and J. Flouquet, J. Phys. Soc. Jpn. **88**, 063707 (2019).

[240] W. Knafo, M. Vališka, D. Braithwaite, G. Lapertot, G. Knebel, A. Pourret, J. P. Brison, J. Flouquet, and D. Aoki, J. Phys. Soc. Jpn. **88**, 063705 (2019).

[241] A. Miyake, Y. Shimizu, Y. J. Sato, D. Li, A. Nakamura, Y. Homma, F. Honda, J. Flouquet, M. Tokunaga, and D. Aoki, J. Phys. Soc. Jpn. **88**, 063706 (2019).

[242] S. Imajo, Y. Kohama, A. Miyake, C. Dong, M. Tokunaga, J. Flouquet, K. Kindo, and D. Aoki, J. Phys. Soc. Jpn. **88**, 083705 (2019).

[243] G. Nakamine, S. Kitagawa, K. Ishida, Y. Tokunaga, H. Sakai, S. Kambe, A. Nakamura, Y. Shimizu, Y. Homma, D. Li, F. Honda, and D. Aoki, J. Phys. Soc. Jpn. **88**, 113703 (2019).

[244] S. Ran, I.-L. Liu, Y. S. Eo, D. J. Campbell, P. M. Neves, W. T. Fuhrman, S. R. Saha, C. Eckberg, H. Kim, D. Graf, F. Balakirev, J. Singleton, J. Paglione, and N. P. Butch, Nat. Phys. **15**, 1250 (2019).

[245] S. Bae, H. Kim, Y. S. Eo, S. Ran, I.-l. Liu, W. T. Fuhrman, J. Paglione, N. P. Butch, and S. M. Anlage, Nature Communications **12**, 1 (2021).

[246] S. Kittaka, Y. Shimizu, T. Sakakibara, A. Nakamura, D. Li, Y. Homma, F. Honda, D. Aoki, and K. Machida, Phys. Rev. Research **2**, 032014(R) (2020).

[247] T. Metz, S. Bae, S. Ran, I. L. Liu, Y. S. Eo, W. T. Fuhrman, D. F. Agterberg, S. M. Anlage, N. P. Butch, and J. Paglione, Phys. Rev. B **100**, 220504(R) (2019).

[248] G. Nakamine, K. Kinjo, S. Kitagawa, K. Ishida, Y. Tokunaga, H. Sakai, S. Kambe, A. Nakamura, Y. Shimizu, Y. Homma, D. Li, F. Honda, and D. Aoki, Phys. Rev. B **103**, L100503 (2021).

[249] C. Paulsen, G. Knebel, G. Lapertot, D. Braithwaite, A. Pourret, D. Aoki, F. Hardy, J. Flouquet, and J.-P. Brison, Phys. Rev. B **103**, L180501 (2021).

[250] J. Ishizuka, S. Sumita, A. Daido, and Y. Yanase, Phys. Rev. Lett. **123**, 217001 (2019).

[251] Y. Xu, Y. Sheng, and Y.-f. Yang, Phys. Rev. Lett. **123**, 217002 (2019).

[252] L. Miao, S. Liu, Y. Xu, E. C. Kotta, C.-J. Kang, S. Ran, J. Paglione, G. Kotliar, N. P. Butch, J. D. Denlinger, and L. A. Wray, Phys. Rev. Lett. **124**, 076401 (2020).

[253] S. Fujimori, I. Kawasaki, Y. Takeda, H. Yamagami, A. Nakamura, Y. Homma, and D. Aoki, J. Phys. Soc. Jpn. **88**, 103701 (2019).

[254] Q. Niu, G. Knebel, D. Braithwaite, D. Aoki, G. Lapertot, G. Seyfarth, J.-P. Brison, J. Flouquet, and A. Pourret, Phys. Rev. Lett. **124**, 086601 (2020).

[255] A. B. Shick and W. E. Pickett, Phys. Rev. B **100**, 134502 (2019).

[256] A. B. Shick, S.-i. Fujimori, and W. E. Pickett, Phys. Rev. B **103**, 125136 (2021).

[257] K. Hiranuma and S. Fujimoto, J. Phys. Soc. Jpn. **90**, 034707 (2021).

[258] T. Shishidou, H. G. Suh, P. M. R. Brydon, M. Weinert, and D. F. Agterberg, Phys. Rev. B **103**, 104504 (2021).

[259] H. Watanabe, A. Daido, and Y. Yanase, arXiv:2109.14866 (2021).

[260] H. Watanabe, A. Daido, and Y. Yanase, arXiv:2109.14874 (2021).

[261] P. Wadley, B. Howells, J. Elezny, C. Andrews, V. Hills, R. P. Campion, V. Novak, K. Olejnik, F. Maccherozzi, S. S. Dhesi, S. Y. Martin, T. Wagner, J. Wunderlich, F. Freimuth, Y. Mokrousov, J. Kune, J. S. Chauhan, M. J. Grzybowski, A. W. Rushforth, K. W. Edmonds, B. L. Gallagher, and T. Jungwirth, Science **351**, 587 (2016).

[262] H. Watanabe and Y. Yanase, Phys. Rev. B **98**, 220412(R) (2018).

Acknowledgement